STUDYING SEISMOTECTONICS OF EASTERN AND SOUTHERN ANATOLIA USING EARTHQUAKE MECHANISMS

by

Sezim Ezgi Güvercin

B.S., Geophysical Engineering, İstanbul University, 2008

M.S., Geophysics, Boğaziçi University, 2013

Submitted to the Kandilli Observatory and
Earthquake Research Institute in partial fulfillment of
the requirements for the degree of
Doctor of Philosophy

Graduate Program in Geophysics

Boğaziçi University

2019

STUDYING SEISMOTECTONICS OF EASTERN AND SOUTHERN ANATOLIA USING EARTHQUAKE MECHANISMS

APPROVED BY:

Assoc. Prof. Dr. Ali Özgün Konca
(Thesis Advisor; Boğaziçi University) ……..……..

Prof. Dr. Hayrullah Karabulut
(Boğaziçi University) …..…….……..

Prof. Dr. Semih Ergintav
(Boğaziçi University) …..…….……..

Prof. Dr. Argun Kocabey
(İstanbul Technical University) …..…….……..

Prof. Dr. A. M. Celal Şengör
(İstanbul Technical University) …..…….……..

DATE OF APPROVAL: 24.09.2019

Dedicated to my daughter Parla Işık,

ACKNOWLEDGEMENTS

I would like to express my deepest appreciation to my advisor Assoc. Prof. Özgün Konca for his encouragement and unfailing passion of work. I also would like to thank Prof. Hayrullah Karabulut for guiding me during my research and through other related studies.

I am indebted to Prof. Rob Reilinger for his contributions to my research. I also would like to thank Ali Değer Özbakır and Prof. Semih Ergintav for their insightful comments.

I would like to thank my mother Meral Güvercin and my father Ender Güvercin for supporting me during my graduate years.

Finally, I would like to thank my dear daughter Parla who I love to the moon and back, for making me stronger than ever. Without her my whole life would be like the tectonics of Eastern Mediterranean.

ABSTRACT

STUDYING SEISMOTECTONICS OF EASTERN AND SOUTHERN ANATOLIA USING EARTHQUAKE MECHANISMS

The Anatolia-Aegean domain provides a unique opportunity to explore plate interactions where oceanic subduction, continental collision and transform plate motions are observed simultaneously. High seismicity rates and diversity of the earthquake source mechanisms are the result of the accommodation of these relative plate motions. As the initial tectonic buildup involves the amalgamation of different tectonic units, it is natural that lithospheric segments with varying structural properties in this relatively small region also contributes to the complexities of the observations.

Understanding interactions of these plates and related deformation requires an integrated analysis of various observations such as seismic tomography, earthquake slip models, geodetic observations and stress changes along with the seismicity and earthquake source mechanisms. In this thesis, 3 case studies in different tectonic settings are presented: the continental collision in the east, the extension due to roll back in the west and the transition between extension and compression. For these 3 case studies, the relation of earthquake source mechanisms to other seismological and geodetic data is used to better understand the present state of the seismotectonics of Easternmost Mediterranean including eastern Anatolia.

The October 23, 2011 Mw7.1 Van, Eastern Anatolia earthquake which is on an EW trending thrust fault, in a region under N-S compression due to the convergence of the Arabian plate toward Eurasia. The three faults were activated during and after the coseismic rupture. The earthquake source mechanisms with consistent orientations are grouped in three clusters. An average fault mechanism is calculated for each cluster by the summation of moment tensors. The triggered faults have experienced Coulomb stress increase due to co-seismic rupture revealing a mechanism which accommodates NS shortening in the region.

The June 20, 2017 Mw 6.6 Bodrum-Kos earthquake which occurred on an E-W trending normal fault is related to the roll back effect of Hellenic Subduction. The Bodrum-Kos event revealed that the extension in the western section of Gökova Bay is accommodated by a north dipping fault. Two different fault slip models, dipping to north and south, are used to compute the Coulomb stress changes at different depths. The coherency between the seismicity and the regions of increased stress is used to put a constraint on the dip of the ruptured fault. The gradual change of strikes of aftershock mechanisms from east to west is consistent with the rotation of the strain field region indicating that the observed earthquake pattern during the 2017 earthquake reflects the long term tectonic frame work in the region.

In between these compressive tectonics of Eastern Anatolia and extension in the Aegean, Cyprus Arc region acts as a transitional zone which is tectonically less understood. Specifically how the convergence of Nubia toward Anatolia is accommodated remains unclear. By the analyses of novel earthquake source mechanisms, and other seismological and geodetic data, it is proposed that the segmentation of the subducting Nubian Plate has a significant contribution to the lithospheric deformation. The change in the orientations of the earthquake mechanisms around the Isparta Angle determines the eastern boundary of the N-S extension due to roll back of the Hellenic slab and is consistent with the counter clockwise rotation of AnatoliaAegean domain which is revealed by the recent GPS vector field. Thrust mechanism earthquakes along with Bouguer gravity, seismicity, and horizontal GPS velocities reveal the geometry of the subducting slab beneath Antalya Basin towards N-E. We suggest that the Antalya Slab deforms as an isolated block, responding in part to adjacent plates, including the Anatolian Plate that moves toward the west, overriding the remnant Antalya slab.

ÖZET

DOĞU VE GÜNEY ANADOLU'NUN SİSMOTEKTONİĞİNİN DEPREM MEKANİZMALARI İLE ÇALIŞILMASI

Anadolu-Ege bölgesi okyanussal dalma-batma, kıtasal çarpışma ve transform levha hareketlerinin etkilerinin hepsini içerdiği için levha ilişkilerine ışık tutan özel bir öneme sahiptir. Depremsellikteki yüksek değişim oranı ve odak mekanizlarındaki çeşitlilik bu levhaların birbirleri ile ilşkilerinden kaynaklanmaktadır. Bölgenin başlangıçta farklı tektonik ünitelerden oluşuyor olmasından dolayı, litosfer parçalarının küçük alanlarda farklı yapısal özellikler göstermesi gözlemlerdeki karmaşıklığı artırmaktadır.

Bu plakalar arasındaki etkileşimi ve ilgili deformasyonu anlamak için tomografi, deprem kayma modellerinin, jeodezik gözlemlerin ve stres değişimlerinin beraber değerlendirilmesi edilmesi gerekir. Bu tezde 3 farklı tektonik bölgede 3 farklı süreç gösteren fiziksel süreçler incelenmektedir: doğuda kıtasal çarpışma, batıda dalan levhanın geri çekilmesi ile genişleme ve iki rejimin arasında bir geçiş zonu. Bu 3 çalışmada, Doğu Akdeniz ve Doğu Anadolu'nun sismotektoniği, deprem odak mekanizmalarının diğer sismolojik ve jeodezik verilerle ilişkisi kullanılarak daha iyi anlaşılmaya çalışılmıştır.

23 Ekim 2011, Mw 7.1, Van, Doğu Anadolu depremi, Arap ve Anadolu levhalarının karşılaşmalarından kaynaklanan K-G doğrultulu sıkışma rejimi içerisindeki D-B uzanımlı bir ters fay üzerinde gerçekleşmiştir. Eşzamanlı kırılma sırasında üç fay tetiklenmiştir. Benzer doğrultulara sahip olan mekanizmalar 3 gruba ayrılarak her grup için moment tensorlerinin toplamından ortlama birer mekanizma bulunmuştur. Tetiklenen fayların K-G sıkışmayı karşıladığı, hesaplanan Coulomb stressin yükselimi ile desteklenmiştir.

20 Haziran 2017, M_w 6.6 Bodrum-Kos depremi ise Hellenic dalma-batma zonunundan kaynaklanan dalan levhanın geri çekilmesi ile ilişkili D- uzanımlı bir normal fay üzerinde gerçekleşmiş ve kırılan fayın Gökova Körfezi'nde açılmayı karşılayan kuzeye dalmakta olan bir yapıya sahip olduğunu göstermiştir. Kuzeye ve güneye dalan iki farklı fay için modellenen kayma dağılımları farklı derinliklerde Coulomb stres

değişimi hesaplamakta kullanılmış ve sonuçlar söz konusu fayın kuzeye daldığını desteklemiştir. Artçı depremlerin doğudan batıya doğru K-G'den D-B'ya doğru yönelimi, Anadolu levhasının deformasyon yönüyle uyumlu olup, ana şoktan sonra gözlenen depremselliğin bölgedeki uzun periyotlu tektonik rejim ile ilişkili olduğunu ifade etmektedir.

Doğu Anadolu'daki sıkışmanın ve batı Anadolu'daki açılmanın ortasında tektonik olarak daha az anlaşılmış olan Kıbrıs Yayı bir geçiş bölgesi olduğu düşünülmektedir. Özellikle Nubia ve Anadolu karşılaşmasının nasıl karşılandığı belirsizdir. Yeni deprem mekanizması kataloğunun diğer sismolojik ve jeodezik veriler ile birlikte değerlendirilmesi sonucunda dalan Nubia lavhasının parçalanmasının bölgedeki litosferik deformasyona belirgin bir etkisi olduğu söylenebilir. Isparta Açısı etrafındaki mekanizmaların doğrultularının değiştiği yer Hellenic dalmabatma zonunundan kaynaklanan K-G yönlü açılmanın doğu sınırını belirlemektedir. Bu sonuç güncel GPS verileri ile de uyumludur. Çalışma alanındaki ters fay mekanizları, Bouguer gravitesi, depremsellik ve yatay GPS vektöleri Antalya baseni altına dalan levhanın KD yönünde dalan levhanın geometrisi açıklamak için kullanılmıştır. Antalya levha parçası olarak tanımladığımız bu parça izole olmuş bir blok olarak deforme olmaktadır. Batıya doğru hareket eden Anadolu levhasının bu izole levha parçasına üzerlemekte olduğu önerilmektedir.

TABLE OF CONTENTS

ACKNOWLEDGEMENTS iv

ABSTRACT v

TABLE OF CONTENTS ix

LIST OF FIGURES xi

LIST OF TABLES xix

LIST OF ACRONYMS / ABBREVIATIONS xx

1. INTRODUCTION 1

2. TECTONICS 3

3. METHODS 5

4. THE SEISMIC INTERACTIONS AND SPATIOTEMPORAL EVOLUTION OF SEISMICITY FOLLOWING THE OCTOBER 23, 2011 M_W 7.1 VAN, EASTERN ANATOLIA EARTHQUAKE 7

   4.1. Introduction 7

   4.2. Data 9

   4.3. Results 17

      4.3.1. Reactivated Faults 17

      4.3.2. Coulomb Stress Changes 22

   4.4. Discussion 25

5. ON THE INTERACTION BETWEEN NUBIA-ANATOLIA PLATES: SEGMENTATION, GEOMETRY, AND KINEMATICS OF AN ISOLATED SLAB 28

   5.1. Introduction 28

   5.2. Data 31

   5.3. Results 35

   5.4. Discussion 38

5.4.1. The Remnant of Cyprus Subduction: Antalya Slab 38
5.4.2. A Localized Extensional Deformation Zone at the Isparta Angle 42
6. SLIP DISTRIBUTION OF THE 2017 M_W 6.6 BODRUM-KOS EARTHQUAKE: RESOLVING THE AMBIGUITY OF FAULT GEOMETRY 46
6.1. Introduction 46
6.2. Data 48
6.2.1. Aftershock Relocation 48
6.2.2. Aftershock Mechanisms 51
6.3. Results 55
6.3.1. Aftershock Locations and Mechanisms 55
6.3.2. Coulomb Stress Changes and Early Aftershock Distribution 58
6.3. Discussion 60
7. CONCLUSIONS 61
REFERENCES 64
APPENDIX A 76
APPENDIX B 79
APPENDIX C 81

LIST OF FIGURES

Figure 4.1. The map of the study area, Eastern Anatolia, including main tectonic features. Solid black lines indicate the active faults in the region (Emre et al., 2013; Mackenzie et al., 2016). Slip rates of North Anatolian and East Anatolian Faults (Reilinger et al., 2006) are indicated below their names in parentheses. The motion of the Anatolian and Arabian Plates with respect to stable Eurasia are shown by red arrows at a few locations (McClusky et al., 2000; ArRajehi et al., 2010). The epicenter of the Mw7.1 2011 earthquake and its largest aftershock are shown with red stars. The surface deformation observed during the post-seismic period of 2011 earthquake are shown by red lines (Mackenzie et al., 2016). Inset shows the study area (red box) on a wider map of Anatolia and surrounding regions. VF: Van Fault; BF: Bostaniçi Fault; GF: Gürpınar Fault; EF: Erciş Fault; CF: Çaldıran Fault SLVF: South Lake Van Fault. 8

Figure 4.2. Statistics of the relocated aftershocks during the 3 months after 23 October 2011 Van earthquake; (a) longitude errors; (b) latitude errors; (c) depth errors; (d) azimuthal gap; (e) number of stations used for locating each earthquake; (f) frequency-magnitude distribution. 10

Figure 4.3. The relative (a) longitude (b) latitude (c) depth errors of the afterhock locations after the Double-Difference relocation algorithm was applied. ... 11

Figure 4.4. Comparison of catalogs. (a) Epicentral locations of the BDTIM catalog (b) Epicentral locations of the AFAD catalog (c) Epicentral locations after both AFAD and BDTIM catalogs were merged and earthquakes were relocated. (d) Epicentral locations after both catalogs were jpoined and relocation was repeated using the velocity model obtained from Velest. (e) Epicentral locations after the double-difference relocation. 12

Figure 4.5. (a) Map view of aftershock activity during the first 81 days following the mainshock. Each earthquake is shown by a circle scaled by its magnitude and colored based on its hypocenter depth. Three gray strips indicate the locations of depth profiles A-A′, B-B and C-C′ shown in (b). Black arrow on the profile C-C′ corresponds to the intersection of strike-slip fault with the mainshock fault. 19

Figure 4.6. Number of stations used for each focal mechanism solution, displayed at the epicenter location 13

Figure 4.7. Three examples of gCAP waveform fits for the best-fitting mechanism, moment magnitude and results of the depth grid search. Variance reduction is indicated for each event on top of the waveform fits. (Left panel) 2011/10/26, 02:59, M_w 4.16 earthquake is an example where the depth grid search yields a stable single best-fitting depth, therefore the event depth is updated after the waveform modeling. (Middle panel) 2011/10/30, 04:29, M_w 3.74 (Right panel) 2011/11/21, 21:00, Mw 4.32, shows two examples where the mechanism is stable but there are multiple best-fitting depths. In those cases we relied on the depths reported from travel-time locations. ... 15

Figure 4.8. Variance reduction to regional body and surface waves for grid search of strike, dip and rake angles for an Mw4.3 earthquake that occurred on 11/21/2011, 21:00 GMT. The best-fitting solution is obtained for strike=276°, dip=33° and rake=90°. The variance reduction values are saturated at 50%. 16

Figure 4.9. Comparison of focal mechanism solutions obtained in this study using gCAP with the solutions in the Global CMT (GCMT) catalog. GCMT and gCAP focal mechanism solutions are shown by black and red beach balls, respectively. Numbers indicate the fault mechanism solutions in Table S2. Red star represents the epicenter of October 23th, 2011, M_w 7.1 Van earthquake. 17

Figure 4.10. (a) Map view of aftershock focal mechanisms obtained in this study. Red star represents the epicenter of the mainshock. Focal mechanisms colored in purple were used to calculate the orientations of the assumed strike-slip faults associated with the three clusters. The remaining source mechanism solutions are in yellow. 19

Figure 4.11. Coulomb stress change calculated on assumed faults and the main fault using the co-seismic slip model of Elliott et. al., (2013) using InSAR data. The two-segment co-seismic fault geometry is outlined in green. The slip model from Elliott et. al., (2013) is roughened to 6 km by 6 km sub-faults. Blue zones indicate stress decrease while red patches indicate stress increase. 23

Figure 4.12. Coulomb stress change calculated on assumed faults and the main fault using the co-seismic slip model of Elliott et al. (2013) using InSAR data. The two-segment co-seismic fault geometry is outlined in green. The slip model from Elliott et al. (2013) is roughened to 6 km by 6 km sub-faults. Blue zones indicate stress decrease while red patches indicate stress increase. 24

Figure 4.13. Coulomb stress change calculated at the depth of 15 km for the source parameters of the strike-slip fault identified in Cluster III shown in black rectangle. Green star represents the epicenter of the mainshock. Relocated aftershocks that occurred during the first 81 days after the mainshock are indicated by black circles that are scaled by event magnitude. 25

Figure 5.1. Seismotectonic setting of the study region. The circles indicate the seismicity between 2004 and 2018 reported by KOERI (magnitude > 3.5) (www.koeri.boun.edu.tr). The colors indicate focal depths. White arrows show GPS velocities with respect to East of Central Anatolia (Reilinger et. al., 2006). Elevations greater than 800 m are shaded in gray using SRTM30 database. ST: Strabo “Trench”, PT: Pliny “Trench”, IA: Isparta Angle, AB: Antalya Basin, ANX: Anaximander Mountains, FR: Florence Rise, CB:

Cyprus Basin, ADB: Adana Basin. Inset shows broader Plate Tectonic setting. NAF: North Anatolian Fault, EAF: East Anatolian Fault 29

Figure 5.2. Left panel: Stations are indicated by triangles and colored by number of occurrence in the waveforms inversions of the earthquakes that are listed in Table S1. Inset shows the Pn tomography from Mutlu & Karabulut, (2011). Black rectangles indicate the sub-regions with different 1D velocity models that are used for the Green's Function calculations. Right panel: 1D waveforms from Perk, (2013). 32

Figure 5.3. Bootstrap analysis of selected earthquakes. 33

Figure 5.4. Comparison of the focal mechanisms solution in this study with solutions from GCMT and previous studies..... 34

Figure 5.5. a) Earthquake source mechanisms around Antalya Basin obtained in this study. Seismicity is the same as in the Figure 5.1, colored by depth with M > 3.5. Earthquake source mechanisms are also colored by the same color scale. Solid black lines show the profile lines in Figure 5.6. and 5.8. In the background P wave velocity perturbations at 70 km depth from the tomography model of Karabulut et. al. (2019) and this study are shown where positive and negative anomalies are represented by hot and cold colors, respectively. b) Computed horizontal strain rate field. Red arrows show double extensional strain rates. c) White arrows indicate the GPS velocity vectors with respect to Nubia (Ergintav et. al, 2019). Yellow arrows show the slip vectors of thrust mechanisms. 37

Figure 5.6. Topography, gravity anomaly and earthquake dip angles along Profile 1 in Figure 2 a. Gray and blue areas represent land and sea, respectively. Red solid line shows the Bouguer Gravity anomaly. b) The circles represent the seismicity with M > 3.5 and scaled by color with depth. 40

Figure 5.7. a) Gray area represents the topography and bathymetry while the red solid line shows the Gravity anomaly. b) The circles represent the seismicity with M>3.5 and scaled by color with depth. White arrows indicate P axes plunge angles. Positive and negative seismic P wave velocity perturbation is represented by hot colors and cold colors respectively (Karabulut et al., 2019). Red solid line refers to the crustal thickness (Karabulut et al., 2019). 41

Figure 5.8. a) Topography, gravity anomaly and earthquake dip angles along Profile 2 in Figure 5.5. a) Gray and blue areas represent land and sea, respectively. Red solid line shows the Bouguer Gravity anomaly. Red arrow marks the location of the low velocity zone in Figure 5.5. b) The circles represent the seismicity with M > 3.5 and scaled by color with depth. Positive and negative seismic P wave velocity perturbations of the tomography model are represented by hot colors and cold colors, respectively (Karabulut et al., 2019). Red solid line refers to the crustal thickness (Karabulut et al., 2019). Beachballs repesent the normal mechanisms in Figure 5.5. 43

Figure 5.9. Topography, Bouguer gravity anomaly and magnetic anomaly of the region 100 km filtered in a b and c respectively. d) Pn tomography from Mutlu & Karabulut (2011). e) Teleseismic tomography image at 100 km. All maps are shaded with a view angle of N45W. Main features are indicated by areas 1, 2 and 3..... 44

Figure 5.10. The plate boundary between Nubia-Anatolia-Sinai-Arabia. White arrows indicate the GPS velocity vectors with respect to Reilinger et al., (2006). Yellow arrows show the slip vectors of thrust mechanisms. AS: Antalya slab. T1: Tear 1. T2: Tear 2. Hot and cold colors refers to the Pn velocity change with respect to 8 km/s (Mutlu and Karabulut, 2011; Karabulut and Özdeğer, 2018)..... 45

Figure 6.1. . (Inset) Broader study area including the Hellenic Arc and the Aegean Sea region. The red vectors show selected annual GPS velocities with respect

to Anatolia (Vernant et al., 2014). The black box shows the area of the main figure. (Main Figure) The study region of the 2017 Bodrum-Kos earthquake. The black circles filled with yellow show the seismicity between 2002 and 2008 (Bohnhoff et al., 2004; Brüstle, 2012) with magnitude scale on the bottom-left. The GPS stations used in this study are shown by green and red triangles for continuous and campaign sites, respectively. The black box represents the boundary of the best-fitting fault plane used for finite-fault modeling and the black enclosed curves show 50 cm slip contours for the best-fitting north-dipping slip mode 47

Figure 6.2. The distribution of the seismic stations used to locate the mainshock and aftershocks during the first month following the mainshock which are part of Kandilli Observatory and Research Institute (KOERI), General Directorate of Disaster Affairs of Turkey (AFAD), German Research Center (GFZ), Italian Seismic Network (INGV), Seismological Network of Crete and Hellenic Unified Seismic Network (HUSN). (red triangles) . Green star shows the epicenter location..... 49

Figure 6.3. Statistics of the relocated aftershocks during the first 20 days following the July 20, 2017 Bodrum-Kos earthquake; (a) latitude; (b) longitude; (c) depth uncertainties. (d) Frequency-magnitude distribution and the best fitting b-value..... 51

Figure 6.4. The evolution of the relocated seismicity following the mainshock during first 3 days and cumulative seismicity during the first 20 days. 50

Figure 6.5. Result of an inversion of an M_w4.5 aftershock that occurred a day after the mainshock. (a) (left) the best-fitting mechanism information and lower hemispheric projection of station locations. (right) Velocity waveform data (black) and model fits (red) for the P waves and S and surface wave windows. Station name, distance (km) and azimuth (°) are shown on the left of the traces. A band-pass filter between 0.02 Hz and 0.1 Hz for the 35

s P_{nl} window and 0.02–0.08 Hz for the 70 surface wave window was used. Grid search is performed to obtain the strike, dip and rake angles with 5° intervals and to the moment magnitude for a step size 0.1. Maximum time shifts were chosen as 2 s and 5 s for the P_{nl} and Surface wave components respectively. Station name, distance and azimuth of each station is shown on left of the waveforms. (b) Depth vs variance reduction and the best-fitting mechanism at each depth. 53

Figure 6.6. Bootstrap analysis of selected aftershocks with a variance reduction of ~50%. The date, time and magnitude of each earthquake is indicated at the top of the histograms for strike, dip and rake, respectively. By fitting a Gaussian curve, the average value (μ) and the standard deviation (σ) from the bootstrap analysis is calculated and displayed on top right of each plot. Strike, dip and rake values using all the data are also listed below the bootstrap results. 54

Figure 6.7. Map view of relocated mainshock, aftershock distribution and focal mechanisms. Focal mechanisms are colored in gray scale by their occurrence time and scaled in size by magnitude. Yellow circles show the epicenters of aftershock activity of the first 20 days in the vicinity of the main shock (M > 1). The outermost black contour outlines the fault area that slips more than 10 cm. The other black enclosed curves show slip contours at every 50 cm for the final north-dipping slip model. Solid red lines indicate active faults in the region from active fault map of General Directorate of Mineral Research and Exploration (Emre et al., 2013), while red dashed lines indicate faults from the study of Görür et al. (1995) and Kurt et al. (1999). Tick marks show the hanging wall of the identified normal faults from Kurt et al. (1999). SDF: South Datça Fault, NDF: North Datça Fault. 56

Figure 6.8. Seismicity distribution of the first 20 days with fault planes dipping to (a) north, and (b) south. Thick dashed lines show the fault plane. Red filled circle shows the location of the mainshock from this study. Each profile

includes earthquakes within 2.5 km distance to the profile line in each direction. Red dashed lines show the fault lines from Emre et al. (2013) Görür et al. (1995) and Kurt et al. (1999). 57

Figure 6.9. The Coulomb stress changes with the same mechanism as the mainshock for the (a) northdipping (left panel) and (b) south-dipping (right panel) faults at depths between 4-14 km. The gray circles show the aftershocks (M≥1) during the first 5 days following the mainshock (between 2017/07/20 and 2017/07/25). Coulomb stress changes are calculated on faults having the same mechanism as the mainshock. 59

LIST OF TABLES

Table A.1. Source parameters (strike, dip and rake angles and moment magnitude) obtained in Chapter 4. (r. Relocated events; *. Centroid depth)..... 76

Table A.2. GCMT solutions of selected earthquakes)..... 13

Table B.1. Calculated mechanisms in this study. Lines with asterisks show the mechanisms that are compared to other studies and GCMT solutions. Highlighted lines are not presented in the main text since they are out of the area of this study, still are resolved to provide a better understanding of uncertainty of our solutions. Bold and italic rows indicate the earthquake focal mechanism solutions to which we applied bootstrap analysis..... 79

Table B.2. Other studies. Bold line shows the earthquake source mechanism from *Jackson & McKenzie* (1977) others are from *Howell et al.* (2017). 80

Table B.3. GCMT solutions..... 80

Table C.1. Several point source mechanism solutions by global and local agencies 81

Table C.2. The velocity model for the region obtained from earthquake relocations. .. 81

Table C.3. The velocity model for the region obtained from earthquake relocations. .. 81

LIST OF ACRONYMS / ABBREVIATIONS

1D	1 Dimension
AB	Antalya Basin
ADB	Adana Basin
AFAD	Authority Disaster and Emergency Management Presidency
ANX	Anaximander Mountains
AS	Antalya Slab
BDTIM	Bölgesel Deprem-Tsunami İzleme ve Değerlendirme Merkezi
CAP	Cut and Paste
CB	Cyprus Basin
CDCAT	Continental Dynamics-Central Anatolian Tectonics
CMT	Centroid Moment Tensor
CQ	Cyprus Broadband Seismological 201 Network
E	East
EAF	East Anatolian Fault
FMM	Fast Marching Method
FR	Florence Rise
GEOFON	GEOFOrschungsNetz
GFZ	Geo Forschungs Zentrum
GPS	Global Positioning System
HUSN	Hellenic Unified Seismic Network
IA	Isparta Angle
INGV	Italian Seismic Network
InSAR	Interferometric Synthetic Aperture Radar
IS	Israelian Broadband Seismological Network
KOERI	Kandilli Observatory and Earthquake Research Institute
LOS	Line of sight
M	Magnitude
N	North
NAF	North Anatolian Fault
NDF	North Datça Fault

PT	Piliny Trench
S	South
SDF	South Datça Fault
SIMBAAD	Seismic Imaging of the Mantle Beneath the Anatolian-Aegan Domain
ST	Strabo Trench
USGS	United States Geological Survey
W	West

1. INTRODUCTION

Understanding the origins of lithospheric deformation requires examination of tectonic processes using variety of methods involving different disciplines of earth sciences. While the surface expressions of the underlying physical processes are studied using geological methods, the source of driving mechanisms need to be further investigated by a combination of seismological, geodetic and geodynamical studies.

In this thesis, we provide insight on the current seismo-tectonics of Anatolia-Aegean region by three case studies using mainly source mechanisms and also other aforementioned tools. These three studies cover various aspects of convergence of Nubia and Arabia toward Anatolia and Eurasia.

In the second chapter, a brief summary of tectonic evolution of Anatolia-Aegean domain is given. Detailed information can be found in the introduction sections of chapters four, five and six.

The methodology of moment tensor inversion is given under chapter three, providing details of cut and paste (CAP) method and its advantages over the standard waveform inversion techniques.

In the fourth chapter, reactivation of faults surrounding the main rupture of 2011, Van earthquake and their geometry are revealed by relocation of aftershocks and significant number of high resolution source mechanisms. The results are supported by the Coulomb stress changes which are calculated using the finite fault model of Elliot et al., (2013). This chapter is published as a product of this thesis (Işık et al., 2017).

The objective of the fifth chapter is to analyze how the convergence of Nubia-Anatolia is accommodated along the southern boundary of Anatolia-Aegean domain. Moreover, we reveal the segmentation of subducting slab and its effects on the overriding plate by a combination of recent teleseismic tomography images, GPS observations,

gravity anomalies and topography. Results are coherent with the high velocity perturbations in the teleseismic tomography, indicating both slab tears at different locations and slab break-off near west of Isparta Angle. This part of the thesis is submitted as a manuscript and is currently under review.

In the sixth chapter, we study the geometry of 2017, M_w 6.6 Bodrum earthquake. This earthquake provides critical information about the active faulting related to the opening of Gulf of Gökova due to roll back along the Hellenic subduction. Previous studies proposed either a north or south dipping fault plane, leading to an ambiguity of the faulting involved with this event. This study, by a combination of different data sets, provides a reliable solution to the problem. A combined analyses of earthquake source mechanisms, relocated aftershock activity and comparison of Coulomb stress changes due to slip models using both north and south dipping fault planes from Konca et al., (2019) lead to a unique solution to the problem, clarifying this ambiguity.

The last chapter summarizes the result from chapters four, five and six, in the general context of tectonics of Anatolia-Aegean domain.

2. TECTONICS

The Anatolia-Aegean domain developed through the accretion of terranes to the north from late Cretaceous (100-66 Ma) until the end of Eocene (33 Ma) (Dewey and Şengör, 1979; Şengör and Yılmaz, 1981). Around the end of the Eocene, Africa-Eurasia convergence slowed down in two major episodes; the first episode in late Oligocene to early Miocene (~25 Ma) when convergence slowed by ~50% with the formation of the East African Rift and Red Sea basin (McQuarrie et al., 2003, Jolivet & Faccenna 2000). The second episode of slowing occurred around 11 Ma (McQuarrie et al., 2003) following the development of ocean spreading in the Gulf of Aden and the collision of Arabia with Eurasia (e.g., Jolivet & Faccenna 2000, Reilinger & McClusky, 2011). The current, broad scale tectonics of the region are dominated by the convergence of the Nubian and Arabian plates with Eurasian plate late in the plate collision process. The interactions of these plates, result in a combination of complex tectonic processes such as collision, subduction, back-arc extension, strike-slip faulting in the Anatolia-Aegean domain.

The deformation of the Anatolia-Aegean domain is strongly correlated with the collision-slowing processes. In the west, the roll-back effect of the Hellenic slab induce back-arc extension in the overriding Anatolia-Aegean domain (e.g., Royden and Faccenna, 2018), resulting in a thinned brittle crust. In the east, the left lateral East Anatolian Fault and Dead Sea fault accommodate the convergence of Arabia with eastern Anatolia. Together these processes are accommodated by the westward “extrusion” of the Anatolian region along the North Anatolian Fault system (Şengör et al., 2014), and rapid southward motion of the south Aegean over-riding the subducting Nubian Plate (e.g., Ergintav et al., 2019).

The rate of shortening across the easternmost Anatolia, which is composed of Karlıova triple junction on the north and Bitlis-Zagros Fold and Thrust Belt on the south, is 10 mm/yr (Reilinger et al., 2006). Due to the N-S compression, the convergence in the region is accommodated by faults which are oriented in different directions. NW

and NE trending strike-slip, E-W (NNW and ENE) trending reverse faults and N-S trending oblique-slip normal faults (Koçyiğit, 2013).

To the west, where the extension due to Hellenic Arc has highest rates at about 20 mm/yr (McClusky et al., 2000; Aktuğ et al., 2009; Floyd et al., 2010), normal faulting witihin large horst-graben systems is observed, from Gökova Gulf to Izmir Peninsula and the Gediz and Büyük Menderes Graben systems (e.g., Sengor et al., 1984). Hence, the region frequently generates M>5 earthquakes mostly on south-dipping faults (Görür et al., 1995; Emre et al., 2013).

On the other hand, the consequences of the deceleration and Nubia-Arabia/Eurasia collision along the Cyprus Arc in the Easternmost Mediterranean, and its effects on the deformation and geomorphology of Anatolia are not clear. There are clear variations in the style of convergence along the arc system that may be induced by differential roll-back between the Hellenic and the Cyprus arcs (Şengör and Yılmaz, 1981; Dercourt et al., 2000; Jolivet et al., 2013), however; how the convergence is accommodated in the Cyprus region is still debated.

3. METHODS

We employ cut and paste method (CAP) (Zhao and Helmberger; 1994, Zhu and Helmberger; 1996, Zhu et al; 2013) to determine focal mechanisms from regional waveforms. The best fitting double-couple mechanism is obtained by performing a grid search over strike, dip, rake and moment magnitude, minimizing the misfit between observed and synthetic waveforms using Green's Functions.

When standard regional waveform inversion methods (e.g. Dziewonski et al., 1981, Dreger & Helmberger, 1993) are used, the misfit is dominated by surface waves due to their higher amplitudes and durations. The major advantages of CAP over these methods are: i- Waveforms are split into Pnl and S-surface wave time windows. ii- Each time window is applied a relative time shift and an independent filter in order to compute the synthetic waveforms. iii- User defined separate weights are applied to the time windows. iv- The waveform amplitudes are rescaled by introducing a distance range scaling factor which preserves the amplitude variations due to radiation pattern while reducing the distance effects in the misfit function.

Thus, the synthetic waveforms are aligned for each time window and the P waveform alignment is not lost unlike the standard methods. Furthermore, inaccuracies in the Green's function computation are reduced when the earth structure is complex.

Although the methodology does not require a detailed earth structure in order to obtain reliable focal mechanism solutions, in specific cases when the structure itself is complex and varies in small scale distances, path dependent Green's functions are needed. In Chapters 4 and 6, unique 1D velocity structures for two different tectonic regions are used to create Green's function library. In Chapter 5, Green's functions are calculated for certain source-station paths according to 1D velocity models which were obtained for different regions in Eastern Mediterranean.

To test the robustness of our solutions and obtain a measure of uncertainty, we used the bootstrap method (Efron, 1979) to the selected earthquakes by making 1000 inversions with randomly selected stations allowing repetition in these selections.

For the horizontal strain rate calculations in Chapter 5, we utilized the approach of Hackl et al., 2009, which uses the spatial derivatives of the interpolated velocity field. Since the strain rate field calculations are independent from the reference frame of the velocity field, we stick to the Nubian fixed reference frame GPS data from Reilinger et al, (2006). Considering the distance between the geodetic observation locations in the study region, we interpolated the velocities with 70 km grid spacing.

4. THE SEISMIC INTERACTIONS AND SPATIOTEMPORAL EVOLUTION OF SEISMICITY FOLLOWING THE OCTOBER 23, 2011 M_W 7.1 VAN, EASTERN ANATOLIA EARTHQUAKE

4.1. Introduction

On October 23rd, 2011, Eastern Anatolia have witnessed the largest earthquake (M_w 7.1) in Van which is reported in the instrumental period. The mainshock occurred on a reverse fault and led to broad scale devastation and more than 600 death of (Kalafat et al., 2014). The focal mechanisms by USGS and Global CMT are 255°/50°/73° and 246°/38°/60°, respectively. Another mechanism with strike, dip and rake angles of 258°/46°/71°, respectively, were determined from InSAR data by Fielding et al. (2013). Their results confirm that the rupture occurred on an almost E-W trending thrust fault with a small left lateral component.

Several co-seismic slip models of this earthquake were presented using various datasets. Elliott et al. (2013) computed the slip distribution of the mainshock two connected fault segments using InSAR data. The segmentation is observed from the InSAR fringes which show offset, which the authors explain by a two-segment fault geometry.Their model has a 35 km length along the strike of the main fault with an average rake of 60°. Another two slip models were computed from the joint inversion of seismic and geodetic data by Konca (2015) and Wang et al. (2015). Their initial models also had two fault patches with rupture lengths of 35 km and 40 km, respectively. Other studies derived slip models of the mainshock with similar geometry from a single patch fault geometry. (Fielding et al., 2013, Feng et al., 2014 and Liu et al., 2015).

It is remarkable that all the slip models are comparable in their lateral sizes, being distributed between 10 km and 20 km, although they differ by the geometrical settings of initial models and the maximum value of slip distributions.

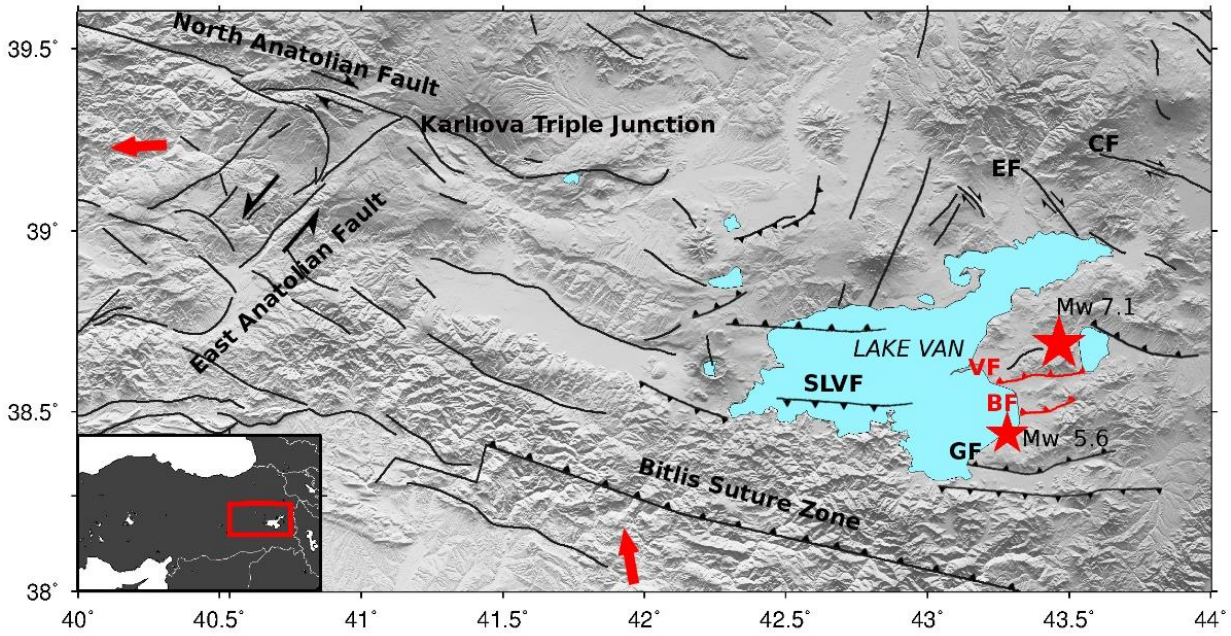


Figure 4.1. The map of the study area, Eastern Anatolia, including main tectonic features. Solid black lines indicate the active faults in the region (Emre et al., 2013; Mackenzie et al., 2016). Slip rates of North Anatolian and East Anatolian Faults (Reilinger et al., 2006) are indicated below their names in parentheses. The motion of the Anatolian and Arabian Plates with respect to stable Eurasia are shown by red arrows at a few locations (McClusky et al., 2000; ArRajehi et al., 2010). The epicenter of the M_w 7.1 2011 earthquake and its largest aftershock are shown with red stars. The surface deformation observed during the post-seismic period of 2011 earthquake are shown by red lines (Mackenzie et al., 2016). Inset shows the study area (red box) on a wider map of Anatolia and surrounding regions. VF: Van Fault; BF: Bostaniçi Fault; GF: Gürpınar Fault; EF: Erciş Fault; CF: Çaldıran Fault SLVF: South Lake Van Fault.

The post-seismic deformation after the mainshock is also examined in several studies. Doğan et al. (2014) revealed that the total moment release is 9.8×10^{18} Nm after the mainshock which refers to a M_w 6.6 earthquake, with most of the post-seismic on the shallower (<10 km) part of the fault that had not ruptured co-seismically. On the other hand, Wang et al. (2015), using three months data following the mainshock, calculated a moment release of 2.04 × 10 19 Nm which is equal to a M_w 6.8 earthquake. Two models demonstrate a major left-lateral strike slip displacement on both main fault and also on a splay fault to the south called Bostaniçi fault (McKenzie et al., 2016) (Figure 4.1)

Considering that the fault which ruptured during the mainshock is blind, it is important to understand why the slip is confined below 10 km. A possible reason was suggested by McKenzie et al. (2016) that the displacement is spread to a splay fault at a depth of 10 km, terminating the slip towards the surface.

The aftershock activity is represented by mainly thrust faulting around the mainshock area by the previous studies. Strike-slip source mechanisms at the eastern and western ends of the main rapture were observed in the first month after the mainshock by Utkucu et al. (2013) from first motion polarities.

The objective of this chapter is to understand the relationship between the reactivation of the faults around the mainshock region and the spatiotemporal evolution of the related aftershocks and their focal mechanisms. The new focal mechanism catalog has a lower magnitude threshold compared to the previous studies which enables a clear identification of the locations and geometry of the faults which activated as a result of the stress transfer after the mainshock.

4.2. Data

The seismicity of first 3 months following the 2011 M_w 7.1 Van earthquake is relocated using the catalogs of General Directorate of Disaster Affairs of Turkey (AFAD), and Boğaziçi University, Kandilli Observatory (KOERI) Regional Earthquake-Tsunami Monitoring Center (BDTIM). The joint catalog consists of the events whose phase readings are merged from two catalogs and the events which exist in one catalog. The phase readings of the first 3 days of aftershock activity is picked manually from the continuous waveforms. The phase pickings of the aftershocks in the first 3 months following the mainshock with magnitude > 4 were also updated using the continuous waveforms. The joint catalog contains > 6700 earthquakes between the dates from the mainshock to the end of 2012. VELEST code (Kissling et al., 1994) was used to obtain the best-fitting 1-D minimum velocity model that minimizes the travel time errors and

resulting station corrections are applied for the relocation process (statics are in Figure 4.2).

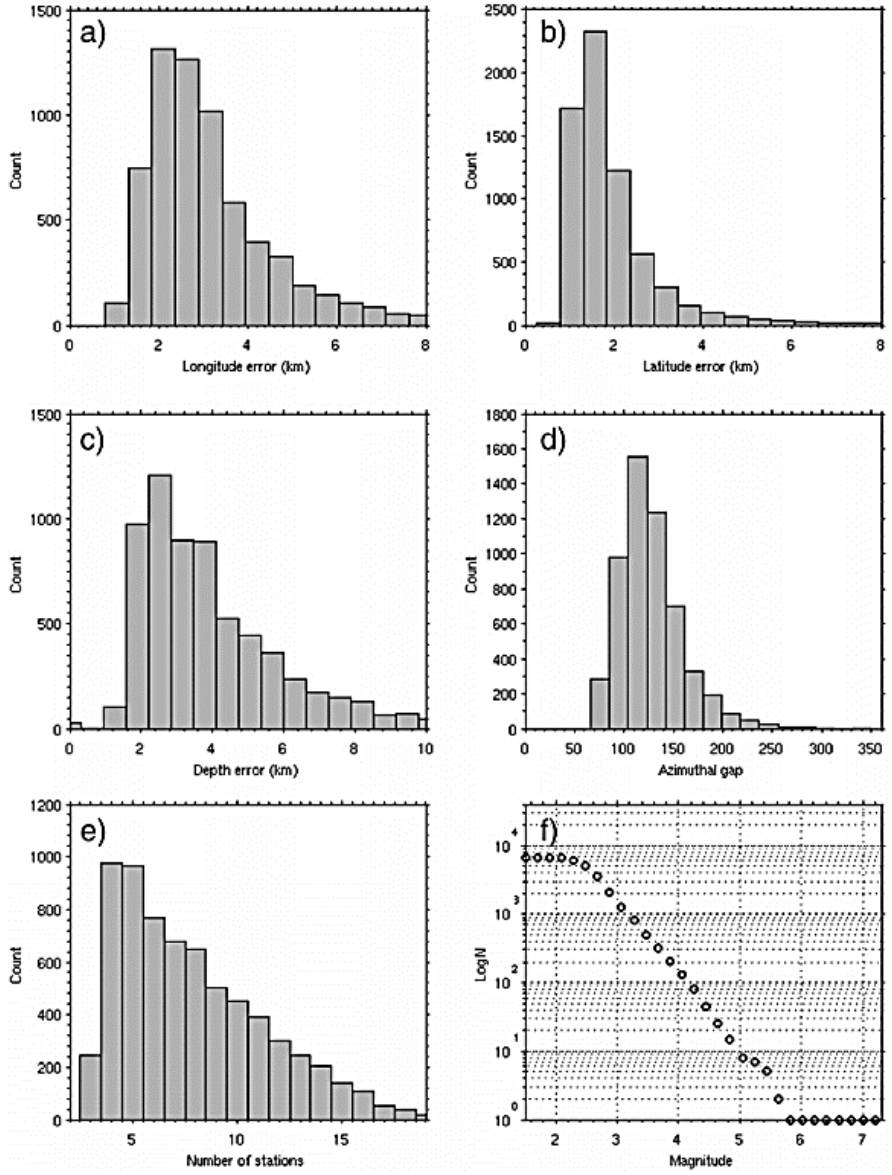


Figure 4.2. Statistics of the relocated aftershocks during the 3 months after 23 October 2011 Van earthquake; (a) longitude errors; (b) latitude errors; (c) depth errors; (d) azimuthal gap; (e) number of stations used for locating each earthquake; (f) frequency-magnitude distribution.

In order to maximize the reliability of the new hypocenters, we relocated the catalog with HYPODD which is a relative location code based on the double-difference method

(Waldhauser and Ellsworth, 2000; Waldhauser, 2001). The relative location uncertainties are reduced to only a few hundred meters after the double-difference method is applied as shown in Figure 4.3. Figure 4.4, shows the epicentral locations of the Van earthquake aftershocks from two initial catalogs and for various stages of the relocation procedure. Results show that the double-difference relocation gives the most compact distribution of aftershocks.

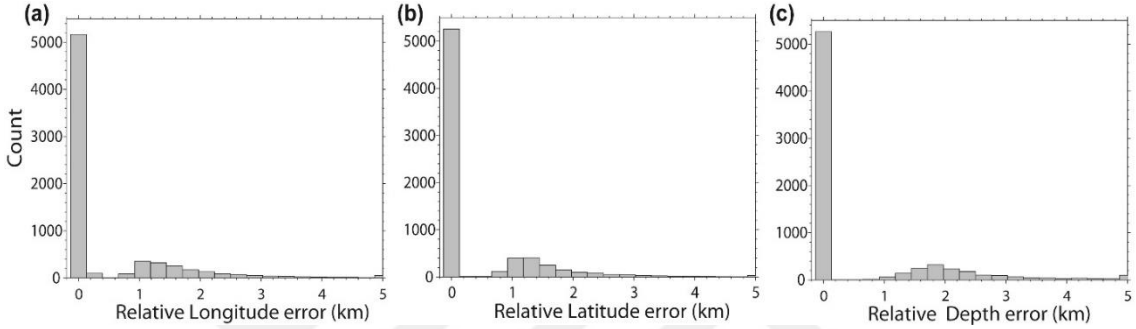


Figure 4.3. The relative (a) longitude (b) latitude (c) depth errors of the afterhock locations after the Double-Difference relocation algorithm was applied.

For the earthquake focal mechanisms, all available seismic stations within the epicentral distance of 300 km are utilized. 17 of these broadband seismic stations are operated by AFAD, while 8 of them are operated by BDTIM (Figure 4.5). Number of stations used for each focal mechanisms solution is shown in Figure 4.6. The Green's functions library is derived from the 1-D velocity model from Zor et al., (2003).

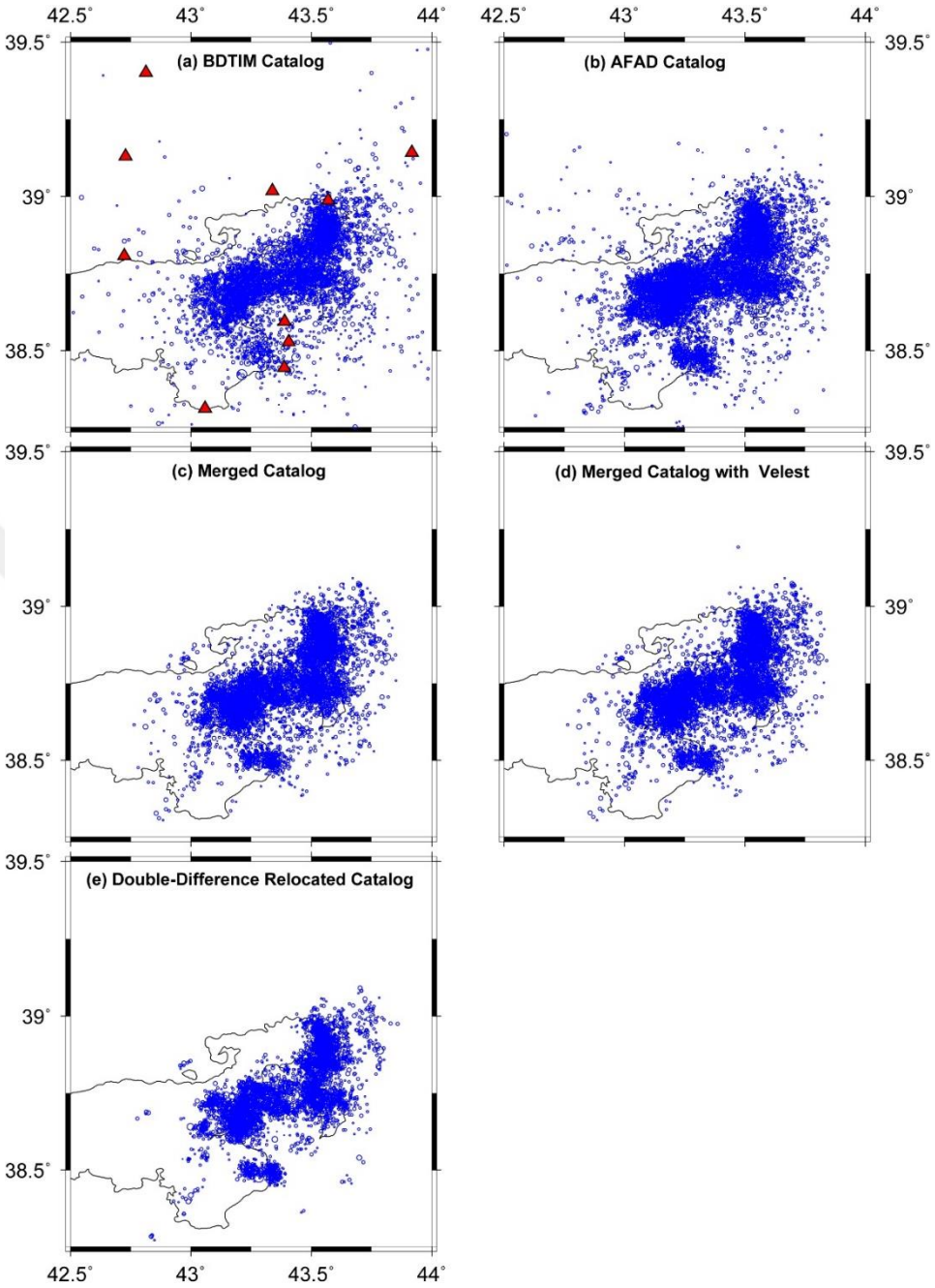


Figure 4.4. Comparison of catalogs. (a) Epicentral locations of the BDTIM catalog (b) Epicentral locations of the AFAD catalog (c) Epicentral locations after both AFAD and BDTIM catalogs were merged and earthquakes were relocated. (d) Epicentral locations after both catalogs were jpoined and relocation was repeated using the velocity model obtained from Velest. (e) Epicentral locations after the double-difference relocation.

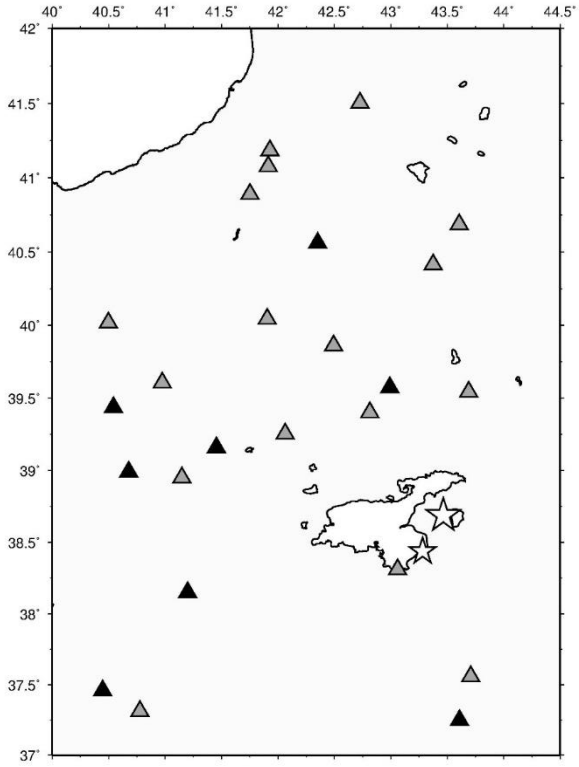


Figure 4.5. Stations used in the focal mechanism inversions. Light gray and black triangles indicate stations operated by AFAD and BDTIM, respectively. White stars mark the epicenters of main shock and largest aftershock.

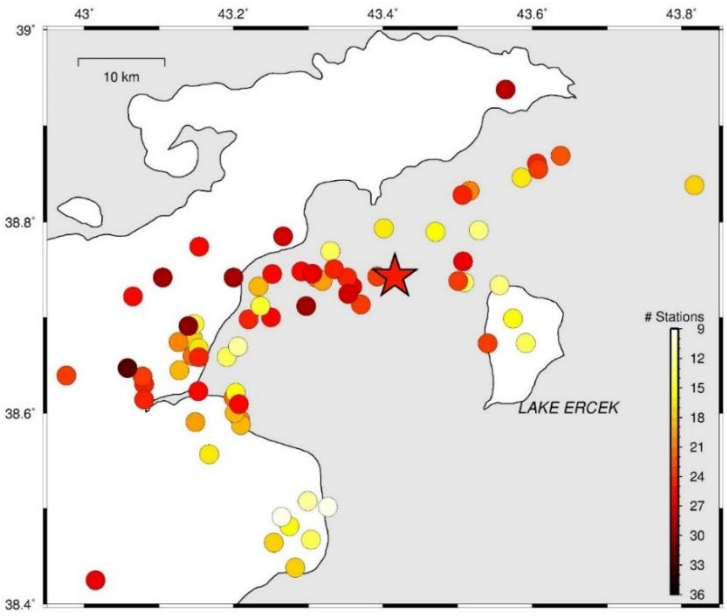


Figure 4.6. Number of stations used for each focal mechanism solution, displayed at the epicenter location

Eliminating the earthquakes focal mechanism solutions with a variance reduction < 50 %, we end up with 74 focal mechanisms out of 106. All waveforms are applied a band-pass filter between 0.02 Hz-0.1 Hz for Pnl, and 0.02 Hz-0.08 Hz for surface waves. Time windows of 35 s and 70 s are used for Pnl and surface waves, respectively. Hypocenter depths of 15 events are determined by grid search over a depth rage between 5 km and 30 km. Rest of the depths are from the relocated catalog.

Waveform fits with depth resolution of example an event are in Figure 4.7. We computed rake and dip angles of an M_w 4.3 event for different strikes which shows that there is no unique solution; instead there is a best fitting region with an uncertainty on the order of ±25° (Figure 4.8). 8 of the moment tensor inversions are compared to the solutions from Global CMT in order to analyze the stability of the solutions (Figure 4.9). Seven of the earthquakes have quite similar mechanisms, while one out of the 8 earthquakes shows the same thrust mechanism but with a different strike angle which might have resulted from the small number of stations used in the inversion, leading to a greater uncertainty.

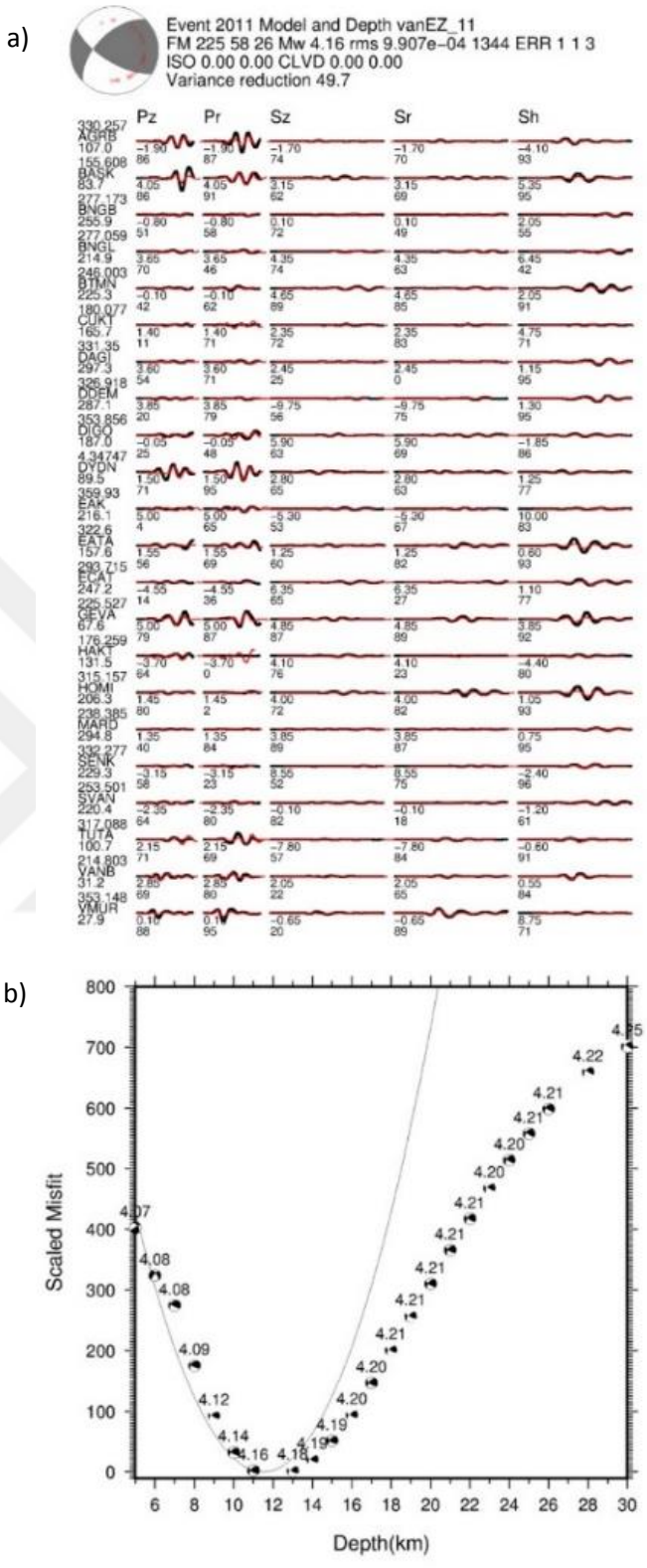


Figure 4.7. An example of gCAP waveform fits for the best-fitting mechanism of 2011/10/26, 02:59, M_w 4.16 earthquake. a) Waveform fits. Variance reduction is indicated on top of the waveform fits. b) Depth grid search.

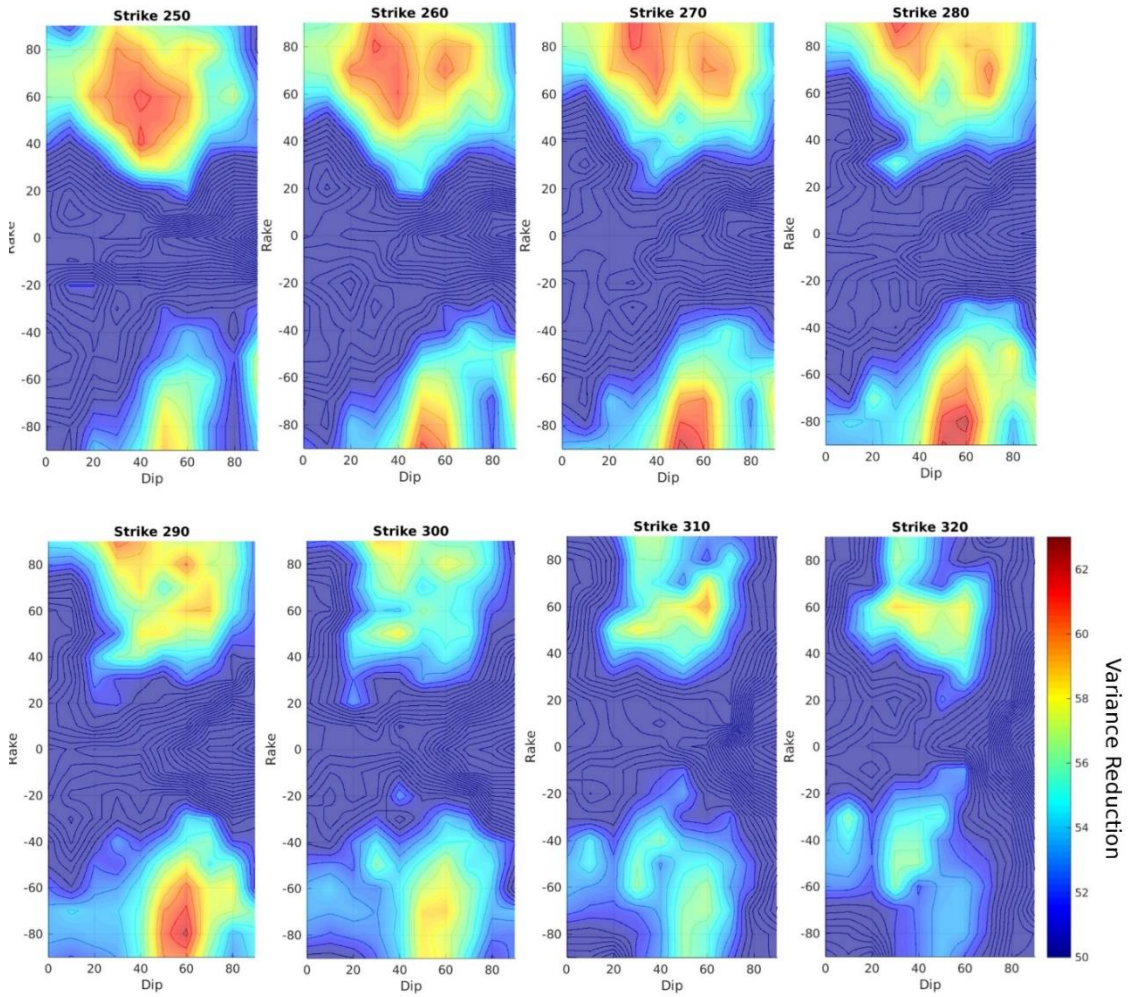


Figure 4.8. Variance reduction to regional body and surface waves for grid search of strike, dip and rake angles for an M_w 4.3 earthquake that occurred on 11/21/2011, 21:00 GMT. The best-fitting solution is obtained for strike=276°, dip=33° and rake=90°. The variance reduction values are saturated at 50%.

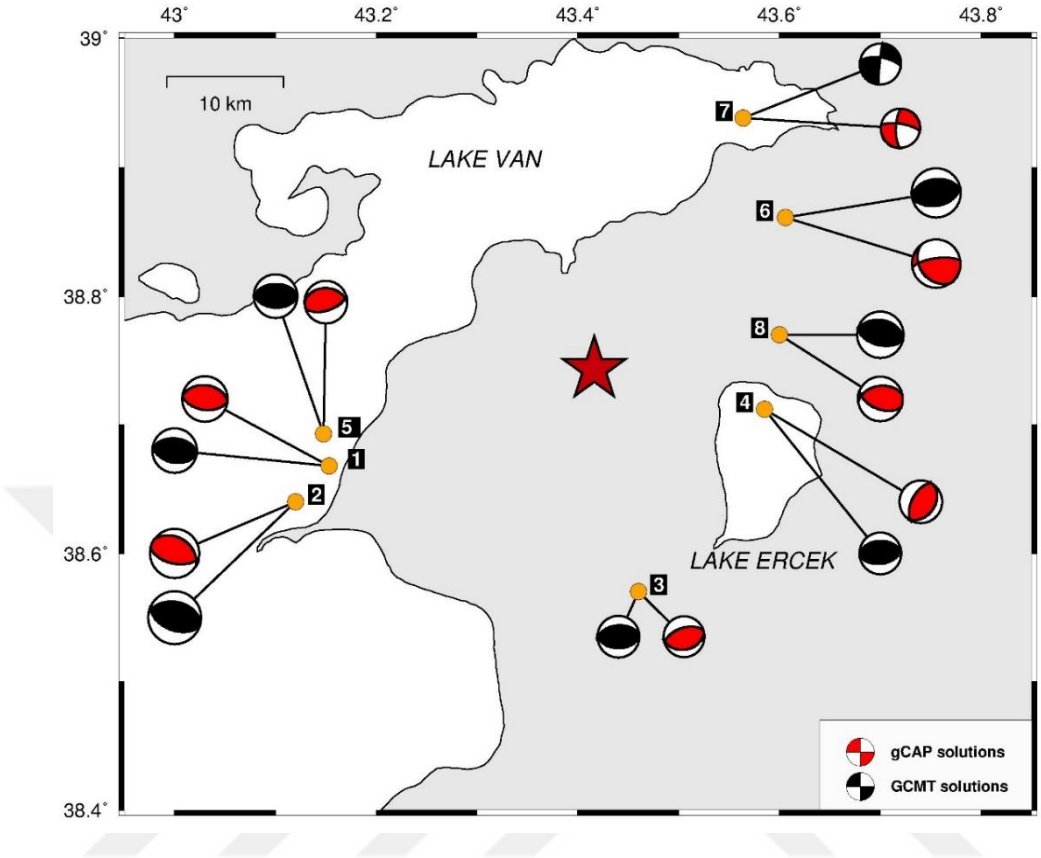


Figure 4.9. Comparison of focal mechanism solutions obtained in this study using gCAP with the solutions in the Global CMT (GCMT) catalog. GCMT and gCAP focal mechanism solutions are shown by black and red beach balls, respectively. Numbers indicate the fault mechanism solutions in Table S2. Red star represents the epicenter of October 23th, 2011, M_w 7.1 Van earthquake.

4.3. Results

4.3.1. Reactivated Faults

The distribution of aftershocks (Figure 4.10) show that the aftershocks are not aligned along the almost E-W strike of the mainshock. Significant number of aftershocks demonstrates a pattern which deviates from E-W to N-S at each end of the main fault rupture area. It is also remarkable that the depths of the N-S lineated aftershocks are shallow compared to the aftershocks around the main shocks, especially at further distances.

Based on the changes in the lineation of the aftershock distribution and their focal mechanisms, we define 3 clusters for earthquakes which are off the mainshock area or inconsistent with the mainshock mechanism. The N-S profiles of depth distribution of aftershocks are shown in Figure 4.10. The cluster locations and earthquakes included in each cluster are shown in Figure 4.11. Profile AA' crosses Cluster 1 and Cluster 2. Profile BB' crosses the mainshock area while Profile CC' crosses Cluster 3 (Figure 4.11). The depth sections in Figure 4.10, show that Cluster 1 is distributed between surface and 25 km without a clear trend. Cluster 2 takes place with a clear trend towards south, at the eastern end of the mainshock area. Cluster 3, which is located further south of Cluster 1, tends to have E-W lineation at shallow depths.

The focal mechanism solutions in these 3 clusters include many oblique ones with significant left-lateral strike-slip components along with the thrust mechanisms around the mainshock area. Cluster 1 is located at the western tip of the co-seismic rupture and it initiated 2 hours after the main shock with a strike-slip component and resulted in a 23 km long aftershock activity towards south. Another strike-slip activity began at the eastern tip of the co-seismic slip (Cluster 2) 6 hours after the mainshock. Cluster 2 activity started at a location which is close to the main rupture area. However, the rest of the activity moved further away from the mainshock area in time, towards N with a 27 km elongation (Figure 4.10). On the other hand, 17 days after the mainshock, the last activity started with an M_w 5.6 event on November 9th, 2011. The lineation of this activity indicates that the first earthquake ruptured the possible extension of the right-lateral Edremit Fault (Ketin, 1977). Wang et al. (2015) also observed right-lateral strike-slip displacements depending on the aftershock activity of the M_w 5.6 event by InSAR data.

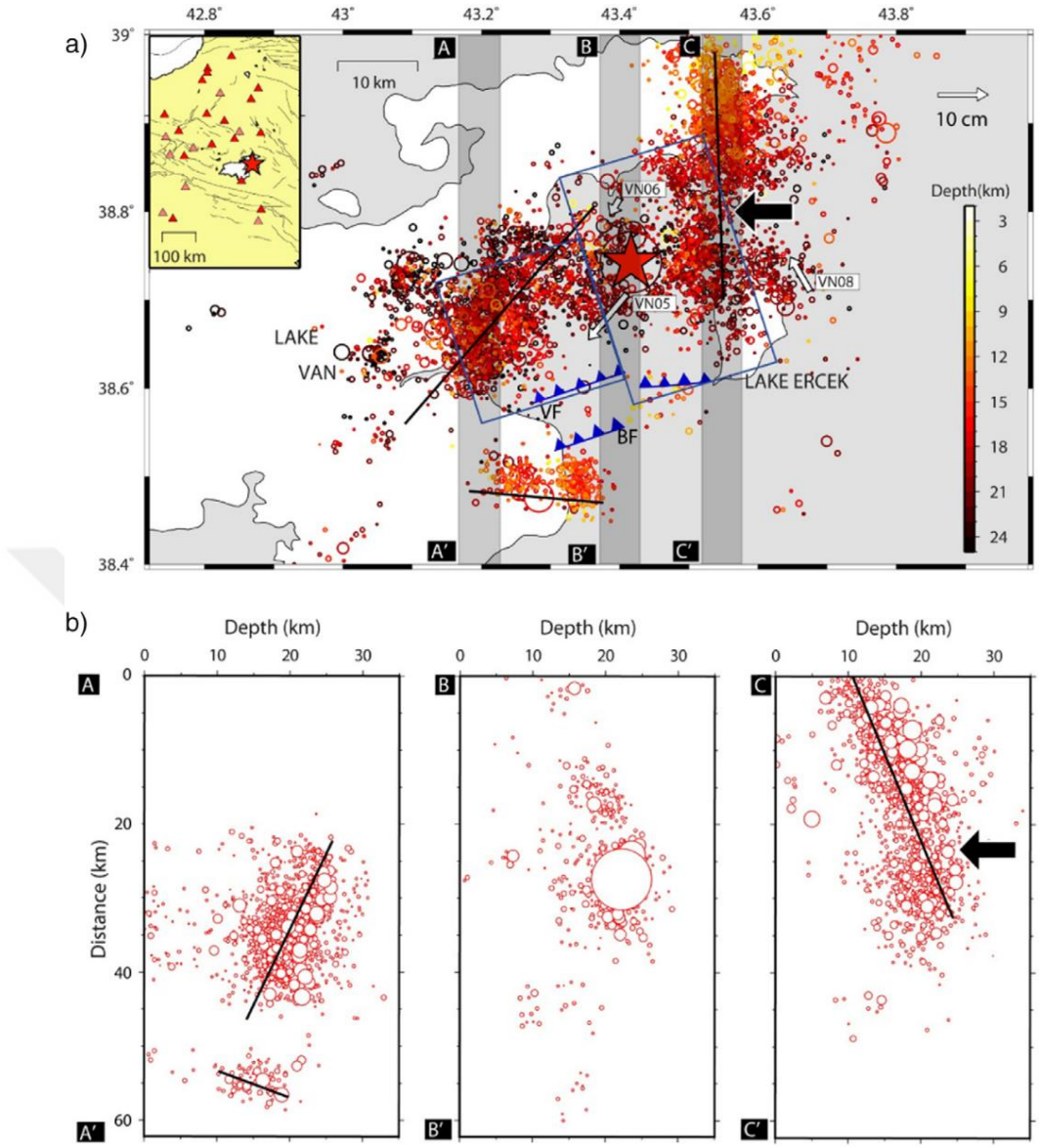


Figure 4.10. (a) Map view of aftershock activity during the first 81 days following the mainshock. Each earthquake is shown by a circle scaled by its magnitude and colored based on its hypocenter depth. Three gray strips indicate the locations of depth profiles A-A′, B-B and C-C′ shown in (b). Black arrow on the profile C-C′ corresponds to the intersection of strike-slip fault with the mainshock fault. The rectangular boxes show the edges of the two-segment co-seismic slip model of Elliott et al. (2013) and the red star represents the epicenter. Surface expressions of the Van fault (VF) and The Bostaniçi splay fault (BF) observed during the post-seismic period are indicated by blue lines with triangles indicating the hanging wall side (Mackenzie et al., 2016). White arrows show the GPS displacement vectors recorded at stations VN05, VN06 and VN08 during the 1.5 year post-seismic period (Doğan et al., 2014). Solid black lines show the surface projection of faults that are activated due to mainshock as proposed in this

study. The inset shows the broadband seismic stations (BDTIM and AFAD stations denoted by light red and dark red respectively) used for waveform modeling. (b) Depth-sections through A-A′, B-B′ and C-C′ shown in panel a. Aftershocks are represented by red circles scaled in size by magnitude. Black arrow in profile C-C′ indicates the intersection of strike-slip fault and the main thrust fault. Solid black lines in profiles A-A′ and C-C′ indicate the depth profile of faults that are proposed in this study.

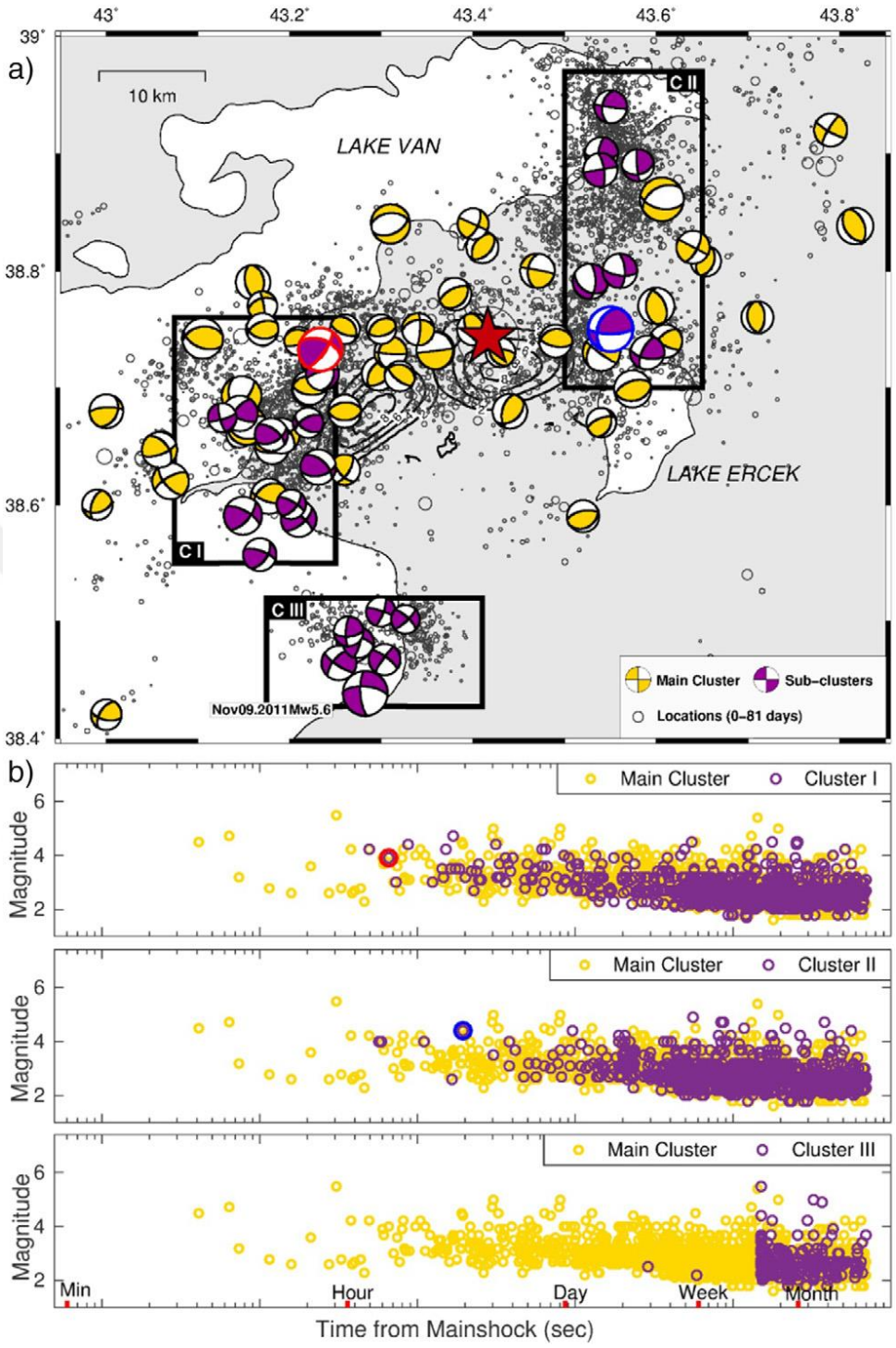


Figure 4.11. (a) Map view of aftershock focal mechanisms obtained in this study. Red star represents the epicenter of the mainshock. Focal mechanisms colored in purple were used to calculate the orientations of the assumed strike-slip faults associated with the three clusters. The remaining source mechanism solutions are in yellow. Black rectangles show the borders of the cluster zones which are numbered based on their initiation time and labeled CI, CII and CIII. Slip contours from Elliott et al. (2013) are

also underlain the focal mechanisms. Relocated aftershocks are shown by black circles which are scaled by their moment magnitudes. Focal mechanisms encircled in red and blue indicate the first strike-slip events in Cluster I and Cluster II, respectively. Solid black line inside the box for Cluster III is the surface trace of the Edremit Fault (Ketin, 1977). In Cluster III, November 9th, 2011 M_w 5.6 event is plotted slightly south of the actual hypocenter to uncover other mechanisms in the cluster. The actual location of this earthquake is shown by the red circle. (b) Time evolution of the aftershock activity in Clusters I, II and III (purple circles) in comparison to the time evolution of aftershock activities on the mainshock fault zone (yellow circles). Red and blue circles represent the first modeled strike-slip events inside Cluster I and II, respectively, as shown in map view in panel a.

4.3.2. Coulomb Stress Changes

Although understanding triggered earthquakes requires the examination of underlying origins which are enigmatic, estimating the Coulomb stress change on suggested faults is a reliable way to determine if they are correlated with the co-seismic displacement. The summation of change in shear stress ($\Delta\tau_s$), and normal stress ($\Delta\sigma_n$) multiplied by the coefficient of friction, μ (King et al., 1995), gives the Coulomb stress change which is the static change of stress in the crust.

In the first step, 3 faults planes are suggested in Clusters 1, 2 and 3. For each cluster, strike, dip and rake angles of the new faults are obtained from the summation of moment tensor (Jost and Hermann, 1989). Considering Cluster 1 and 2 are initiated due to co-seismic slip, 3 finite fault co-seismic slip models (Konca, 2015; Shao and Ji, 2011; Elliott et al., 2013) are tested. The model of Elliott et al. (2013) which has a compact structure matching the 3 suggested faults, is chosen. The results showed that there is a clear increase in stress (2 to 5 bars) around the activated faults which supports the idea that the 2011, Van earthquake triggered neighboring faults (Figure 4.12).

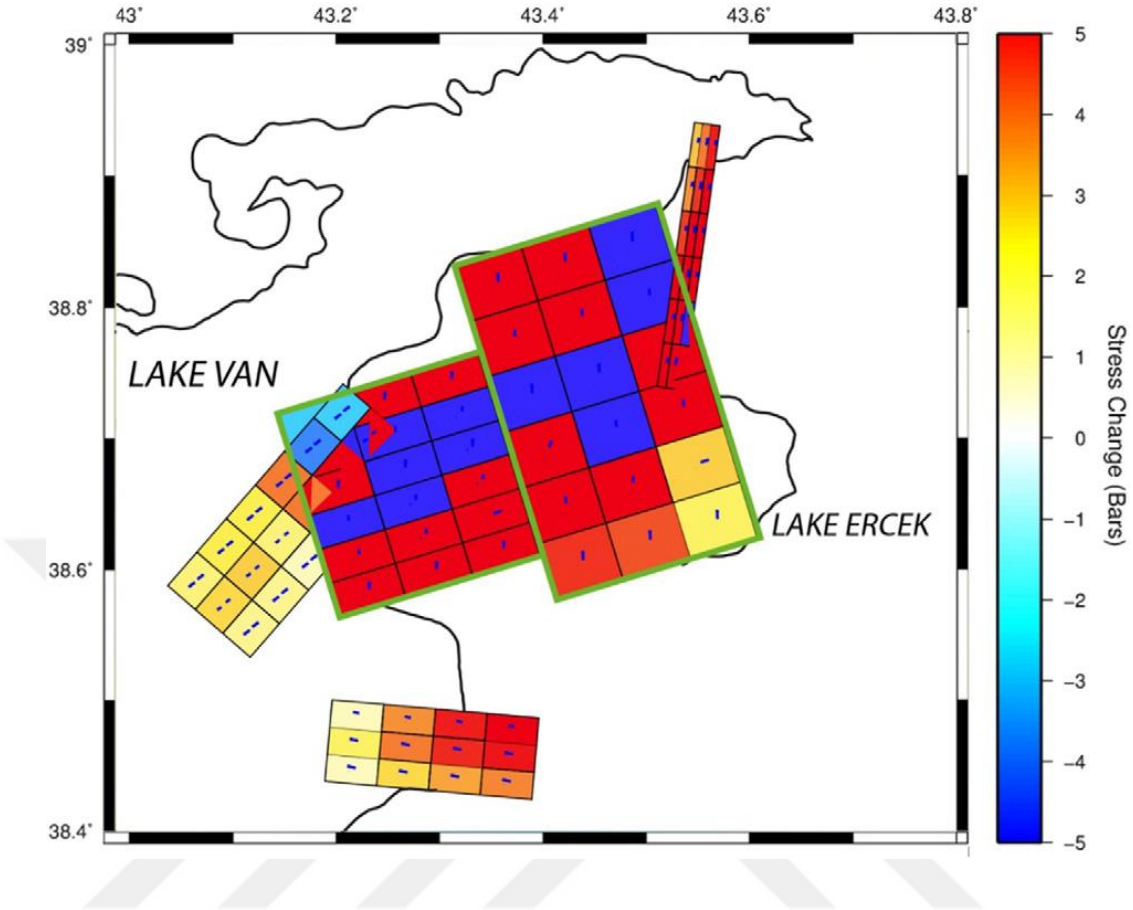


Figure 4.12. Coulomb stress change calculated on assumed faults and the main fault using the co-seismic slip model of Elliott et. al., (2013) using InSAR data. The two-segment co-seismic fault geometry is outlined in green. The slip model from Elliott et. al., (2013) is roughened to 6 km by 6 km sub-faults. Blue zones indicate stress decrease while red patches indicate stress increase.

In addition to stress changes induced on pre-existing faults, Coulomb stress changes at optimally oriented faults are also calculated. This approach assumes that faults exist at every location at every orientation. Aftershocks occur on faults that experience the maximum stress change due to co-seismic slip (King et al., 1995). In this approach initial stresses are calculated from a regional stress model. In this study regional stresses are calculated from from Sezgin and Pınar (2002).

$\sigma 1 = (350, 0), \sigma 2 = (260, 81), \sigma 3 = (80, 9)$

(Compression is in the N–NW & Extension is in the E–NE)

Results of Coulomb stress changes on optimally oriented faults show that almost all of the aftershock activity near the mainshock area and at the eastern and western tips (Clusters 1 and 2) occurred on zones where the stress increased due to co-seismic slip. However, Cluster 3 is in a region where the stress decreased (Figure 4.13). This is because the regional stress regime defined here imply that optimally oriented faults in the region of Cluster 3 are E-W striking thrust faults, rather than E-W striking right lateral strike-slip fault. Therefore, another computation is done with the source parameters of fault in the Cluster 3, which shows an increase in the stress around Cluster 3 for pre-existing E-W striking right-lateral faults (Figure 4.14).

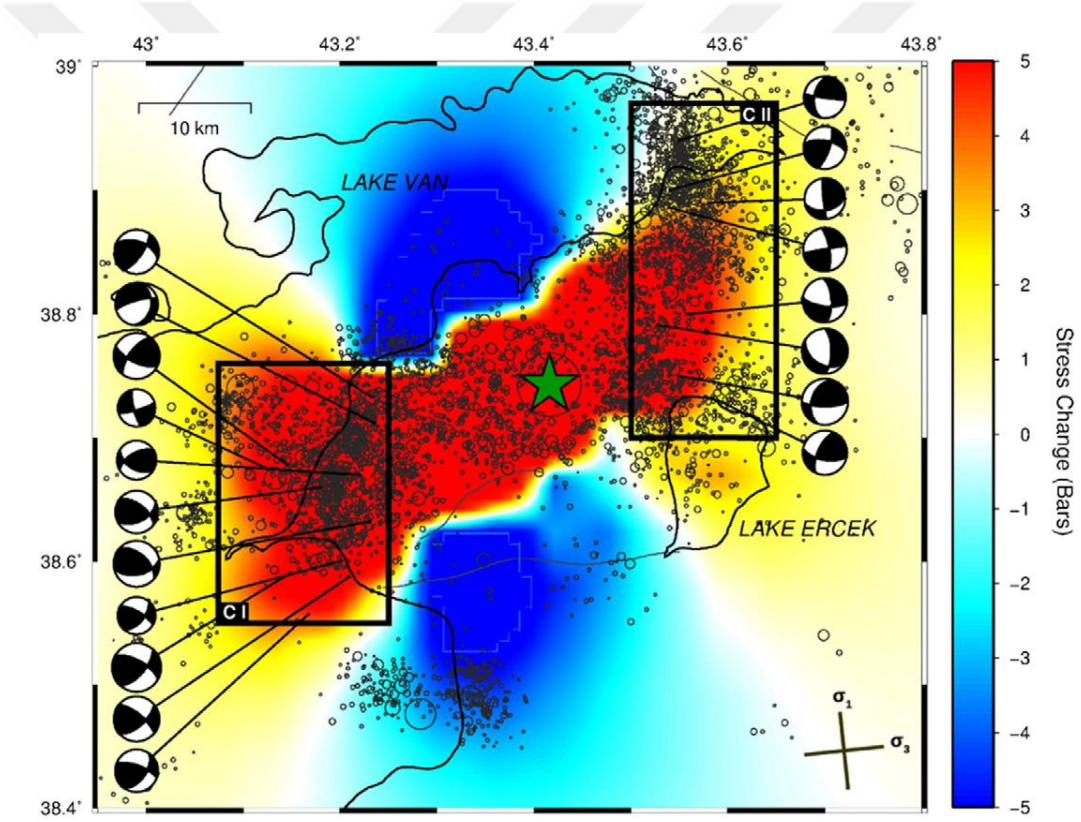


Figure 4.13. Coulomb stress change calculated on assumed faults and the main fault using the co-seismic slip model of Elliott et al. (2013) using InSAR data. The two-segment co-seismic fault geometry is outlined in green. The slip model from Elliott et al. (2013) is roughened to 6 km by 6 km sub-faults. Blue zones indicate stress decrease while red patches indicate stress increase.

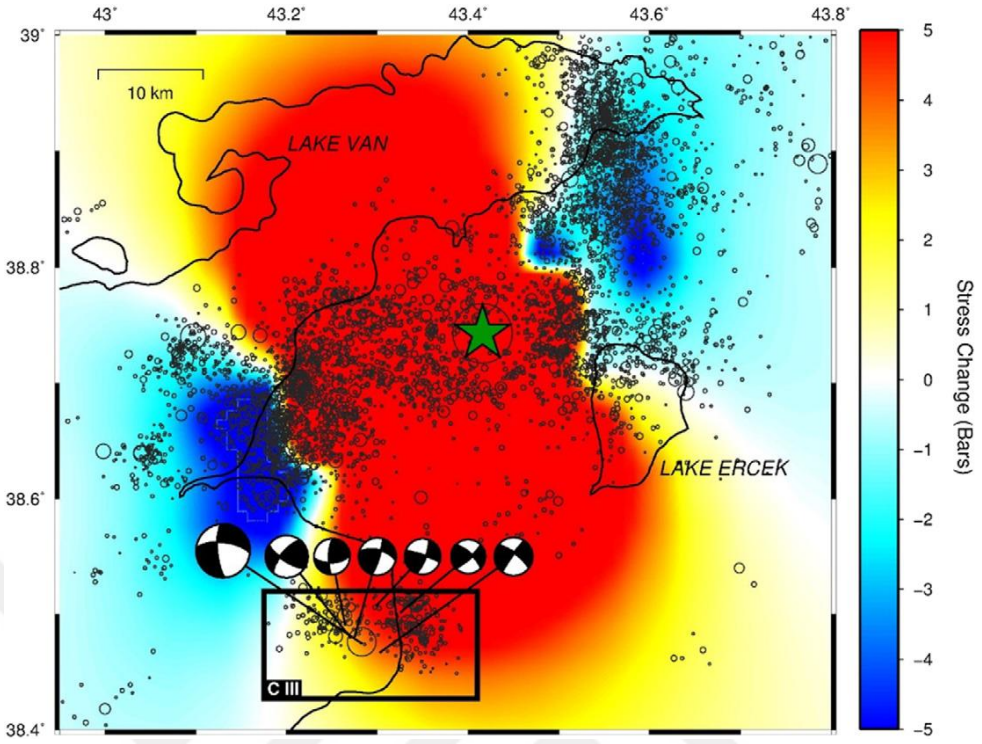


Figure 4.14. Coulomb stress change calculated at the depth of 15 km for the source parameters of the strike-slip fault identified in Cluster III shown in black rectangle. Green star represents the epicenter of the mainshock. Relocated aftershocks that occurred during the first 81 days after the mainshock are indicated by black circles that are scaled by event magnitude.

4.4. Discussion

Convergence of Arabia toward Eurasia leads to N-S compression in Eastern Anatolia east of Karliova triple Junction. Eastern Anatolia is being deformed by mainly 4 different structures: (1) NNE-SSW and/or NE-SW trending left lateral strike-slip faults in southeast Turkey, (2) NW-SE trending right-lateral strike-slip faults in the northeast, (3) east-west trending thrusts and folds (4) N-S trending extension cracks (Arpat et al., 1977; Şengör, 1980; Şaroğlu and Guner, 1981; Şaroğlu, 1985; Barka and Kadinsky-Cade, 1988; Copley and Jackson, 2006). Van region is located at the conjunction of Arabia and Eurasia and defined by E-W thrust faulting while its north is dominated by NW-SE right lateral faults (Copley and Jackson, 2006).

The analysis of the aftershocks demonstrates that activity along N-S trending left-lateral faults are triggered by 2011, Van earthquake and these N-S structures terminate the main rupture at two ends of the main fault. The later E-W activity further to the south was also activated by the post seismic activity. The overall activity of the main fault and reactivated faults are consistent with the N-S compression in the region. Cluster 1 and surroundings include oblique strike-slip earthquakes with some left-lateral component along with thrust mechanisms with varying strike angles. Still this activity plays and important role in being the western termination of the main fault activity, as also seen from the time evolution aftershocks (Figure 4.11). However, it is not clear if the main fault extends through Cluster 1 to the west or not.

The initial earthquakes which occurred in Cluster 1 and Cluster 2 are located at the tips of the main activity indicating that the stress release from the mainshock possibly initiated the seismic activities on the left-lateral faults. Unlike the complex focal mechanisms distribution in Cluster 1, Cluster 2 has a clear seismicity which trends south. The average dip angles which derived from the summation of the moment tensors are consistent with the dip of the seismicity in all clusters.

The region to the north of the mainshock area is characterized by right-lateral faults in NW-SE direction which can be observed on the surface (Mackenzie et al., 2016). However, the reactivation of the fault in Cluster 2 has no surface expression which can be explained by the fact that the deformation of the surface is mainly depended on the structures in the first 10 km of the crust. As a result, the effect that comes from the deeper deformation cannot be observed (Mackenzie et al., 2016). Considering the existence of the surface deformation of reactivated faults and the main fault, it is reasonable to conclude that the region is dominated by thrust and right-lateral strike slip faults at shallow depths (0-10 km) and by oblique mechanisms with left-lateral components at deeper depths (> 10 km).

The suggested mechanism here also gives constraints for the geometry to be used for post-seismic studies. Doğan et al., (2014) studied 1.5 years of post-seismic motion from GPS observations. In their study, while southward motion is observed at VN05 and VN06 stations on the hanging wall, northward motion is observed at VN08 station which

is located further east on the hanging wall. It is impossible to explain this motion for oblique thrust earthquake on an E-W trending fault, which would constrain the hanging wall side to move south. Addition of slip along the left-lateral fault at the northeastern tip of the rupture as proposed here from earthquakes in Cluster 2 would explain the difference of post-seismic GPS displacement vectors. Hence, it is not realistic to interpret the GPS vectors and post-seismic behavior of the region without introducing N-S left-lateral strike slip faults.

Activation of the fault in Cluster 3 has a longer delay compared to Cluster 1 and Cluster 2. The location of this activity is further south of the other clusters and the main activity and it is assumed to be a separate fault which is possibly the western extension of the Edremit Fault. The earthquakes with $M \geq 2.5$ occur after some time delay and the amount of delay varies for each cluster (e.g., Durand et al., 2010; Aksarı et al., 2010; Aktar et al., 2007). The post-seismic slip might have also contributed to the triggering of this fault; however, since the post-seismic models performed until this study do not consider the geometrical complexity suggested here, we avoided adding their contribution to the Coulomb stress change calculations.

In conclusion, the study of aftershock mechanisms of the 2011 Van earthquake show a mechanism where oblique thrust (with a left lateral) rupture of the E-W striking co-seismic fault interacts with N-S striking left lateral and E-W trending right lateral faults. Overall pattern of the mechanisms are consistent with dominant N-S compression in the region due to convergence of Arabia due to Eurasia.

5. ON THE INTERACTION BETWEEN NUBIA-ANATOLIA PLATES: SEGMENTATION, GEOMETRY, AND KINEMATICS OF AN ISOLATED SLAB

5.1. Introduction

Slab segmentation plays a key role in understanding lithospheric deformation and plate boundary evolution (e.g. Govers & Wortel, 2005; Wortel & Spakman, 2000). Segmentation may result from a combination of factors such as subduction of irregular plate margins, lateral variations of lithospheric density/buoyancy contrasts or lateral variations of overriding plate resistance (e.g. Rosenbaum et al., 2008, Wortel et al., 2009). All of the aforementioned factors are present and may have influenced the convergence history of the Eastern Mediterranean (Figure 5.1).

The active plate margin along the Eastern Mediterranean encompasses the Hellenic and Cyprus Subduction Zones. To the west, the Hellenic Arc can be traced from the Kefalonia Transform Fault in the west to the Pliny-Strabo shear zone in the east with a convergence rate exceeding ~35 mm/yr (McClusky et al., 2000; Reilinger et al., 2006). To the east, the Cyprus Arc runs from east of the Pliny-Strabo shear zone to the west of Cyprus with a slower convergence rate of ~15 mm/yr near the Antalya Basin to ~5 mm/yr near the western end of Cyprus (Wdowinski et al., 2006, Özbakir et al., 2017). Although the plate boundary zone in this region is obscured by thick sediments involving diffuse thin-skinned tectonics, the Wadati-Benioff zone extends down to ~150 km depth beneath the Antalya Basin. However, intermediate depth seismicity is discontinuous along the boundary that may indicate slab segmentation. These factors make it difficult to define a simple subduction geometry for the plate boundary east of the Hellenic Arc.

The pertinent features of the Cyprus Arc, namely the Antalya Basin, Anaximander Mountains, and the Florence Rise (Figure 5.1), contain faults with varying orientations and types. Studies relying on seismic reflection profiles suggest pure strike-slip or transpression along a diffuse boundary that goes through the Anaximander Mountains

and the Florence Rise (e.g. Woodside et al., 2002; Ten Veen et al., 2004; Aksu et al., 2019). On the contrary, Howell et al. (2017) argue that convergence is accommodated predominantly by thrust earthquakes and strike-slip motion is subordinate.

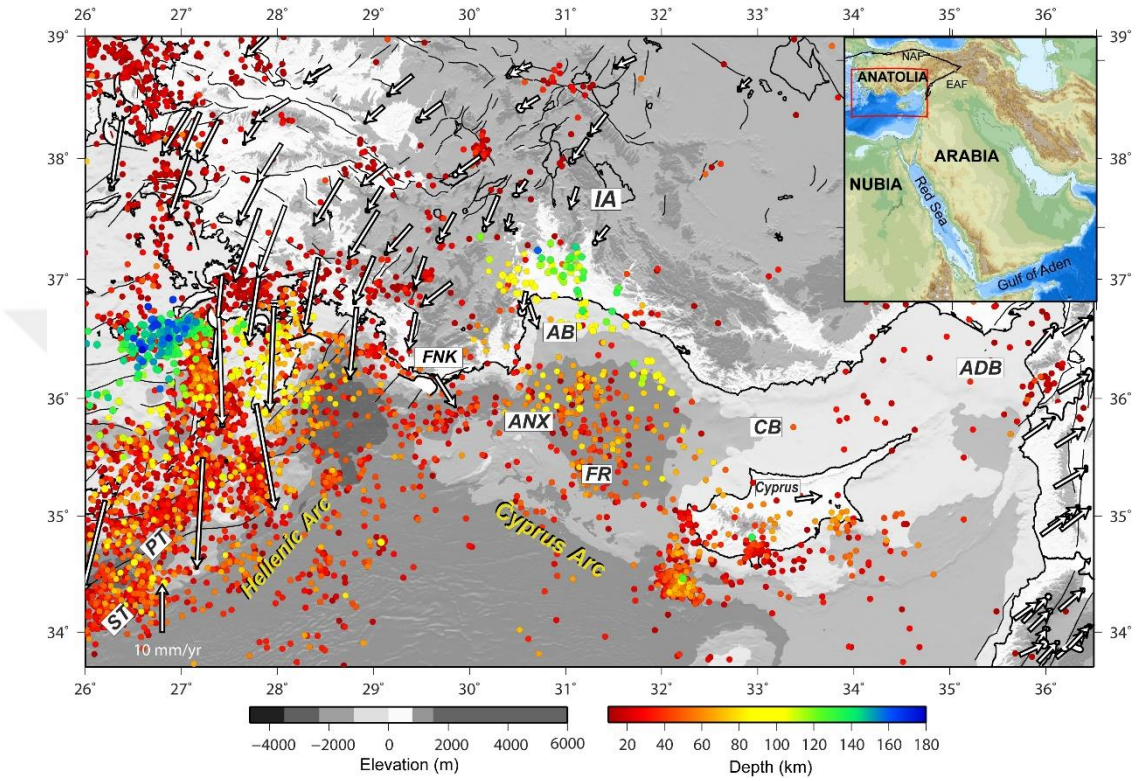


Figure 5.1. Seismotectonic setting of the study region. The circles indicate the seismicity between 2004 and 2018 reported by KOERI (magnitude > 3.5) (www.koeri.boun.edu.tr). The colors indicate focal depths. White arrows show GPS velocities with respect to East of Central Anatolia (Reilinger et. al., 2006). Elevations greater than 800 m are shaded in gray using SRTM30 database. ST: Strabo "Trench", PT: Pliny "Trench", IA: Isparta Angle, AB: Antalya Basin, ANX: Anaximander Mountains, FR: Florence Rise, CB: Cyprus Basin, ADB: Adana Basin. Inset shows broader Plate Tectonic setting. NAF: North Anatolian Fault, EAF: East Anatolian Fault

Earthquake focal mechanism catalogs are critical in order to put kinematic constrains to the convergence of two plates, especially in the Easternmost Mediterranean where the slab geometry and the origins of regional deformation are unclear. The existing focal mechanism catalogs relied either on teleseismic data (e.g. Taymaz et al., 1990; Pilidou et al., 2004; Howell et al., 2017) or first motion polarities (e.g. McKenzie et al.,

1972; Jackson & McKenzie, 1983; Salamon et al., 2003). For the teleseismic moment tensor inversion, the earthquakes need to be large enough to be well recorded at teleseismic distances, which limits the magnitude threshold to typically greater than M~5. The number of events for such criterion is insufficient to elucidate the characteristics of the convergence in the study region. The first motion polarity solutions, only use a limited portion of the earthquake radiation pattern and a reliable solution requires a dense network and good azimuthal coverage. However, the lack of stations to the south of Cyprus creates large uncertainties on the fault plane parameters.

As a result of the low seismicity rate and insufficient station distribution, the available focal mechanism catalogs are not adequate to study the regional deformation. Considering the limited number of reliable earthquake focal mechanism solutions from previous studies in the Cyprus Arc region, an expanded earthquake mechanism catalog with accurately determined fault parameters which are obtained by an advanced waveform inversion method is essential and required.

One way to improve the earthquake source mechanism catalog is to use regional waveforms; however, due to complexity of the crustal and upper mantle velocity structure in the region, this has proven to be challenging. In this study, we overcome this difficulty by computing path dependent Green's functions using 1-D velocity structures for different sub-regions of southern Anatolia. Eventually we expand the earthquake mechanism catalog down to M_w ~4 using regional body and surface waveforms.

The novel earthquake focal mechanism catalog and seismicity along with tomographic studies (Bijwaard and Spakman, 2000; Biryol et al., 2011; Govers and Fichtner, 2015; Portner et al., 2018; Karabulut et al., 2019a) create a unique opportunity to put better constraints on the slab fragmentation and related plate deformation in easternmost Mediterranean.

In short, the geometry and segmentation of the slab under the Antalya Basin, and kinematics of plate convergence along the west Cyprus Arc are still debated. Understanding the behavior of such a highly segmented slab in a heterogeneous lithosphere requires integrating various observations and coherent measurements as both

geometry and kinematics are changing at short length scales. By combining seismic tomographic images of the sub-surface, surface topography, crustal thickness models, focal mechanism solutions for crustal and sub-crustal earthquakes, and gravity anomalies with the GPS observations, we provide new constraints on the present-day kinematics and geometry of the slab under the Cyprus Arc, and its influence on deformation of the over-riding Anatolian plate.

5.2. Data

For the focal mechanism solutions, we utilized 130 broadband stations from GFZ (Geo Forschungs Zentrum) (GEOFON Data Centre, 1993), KOERI (Kandilli Observatory and Earthquake Research Institute) (Bogazici University Kandilli Observatory And Earthquake Research Institute, 2001), AFAD (Authority Disaster and Emergency Management Presidency (AFAD Turkey), 1990), HUSN (Hellenic Unified Seismic Network) (National Observatory of Athens, Institute of Geodynamics, Athens, 1997), IS (Israelian Broadband Seismological Network) (Geophysical Institute of Israel (GII Israel), 1982), CQ (Cyprus Broadband Seismological Network) (Geological Survey Department Cyprus, 2013), SIMBAAD (Etransect (Seismic Imaging of the Mantle Beneath the Anatolian-Aegan Domain) (SIMBAAD-Etransect)) (Paul et. al., 2008). We ignored the stations with poor signal to noise ratio and manually checked the quality of the waveforms. The KOERI catalog with M > 3.5 from 2004 to the end of 2018 is used for the seismicity and for the locations of the earthquakes for which the focal mechanisms are determined. The Green's functions library is derived from the 1-D velocity model from Perk (2013) and updated using Mutlu & Karabulut (2011) (Figure 5.2). Bootstrap analysis for selected events are in Figure 5.3. We also compared our results with GCMT solutions (Figure 5.4)

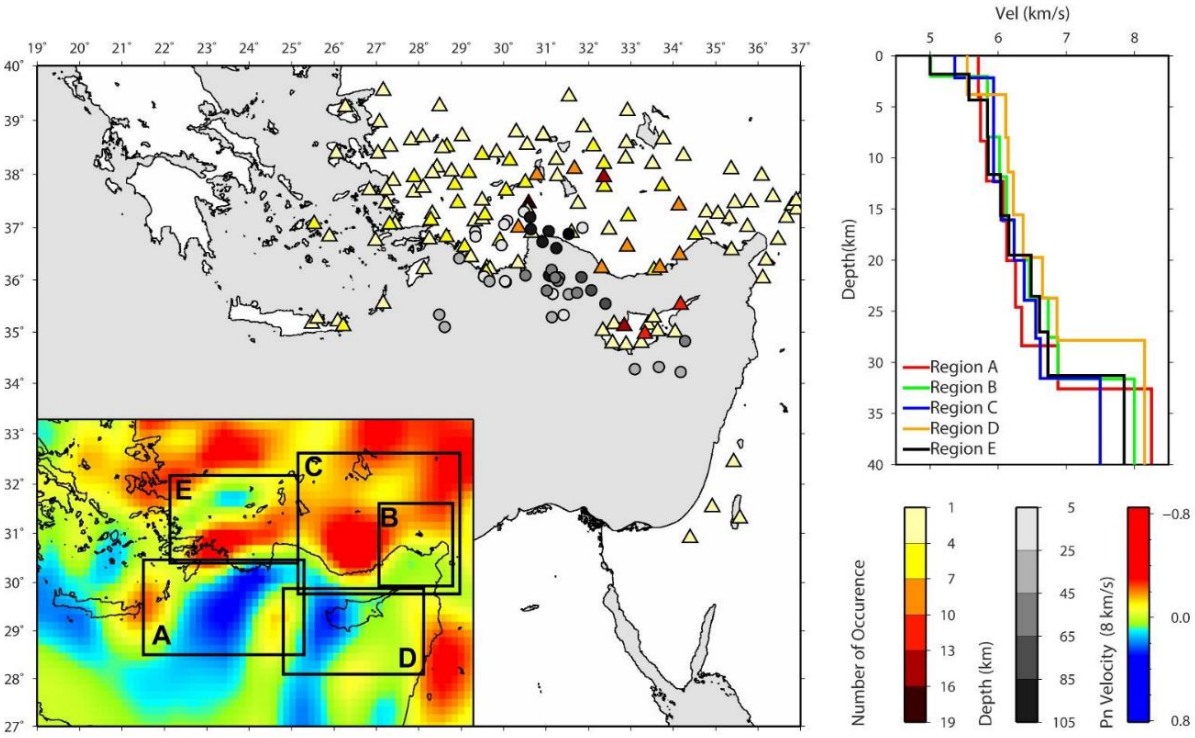


Figure 5.2. Left panel: Stations are indicated by triangles and colored by number of occurrence in the waveforms inversions of the earthquakes that are listed in Table S1. Inset shows the Pn tomography from Mutlu & Karabulut, (2011). Black rectangles indicate the sub-regions with different 1D velocity models that are used for the Green's Function calculations. Right panel: 1D waveforms from Perk, (2013).

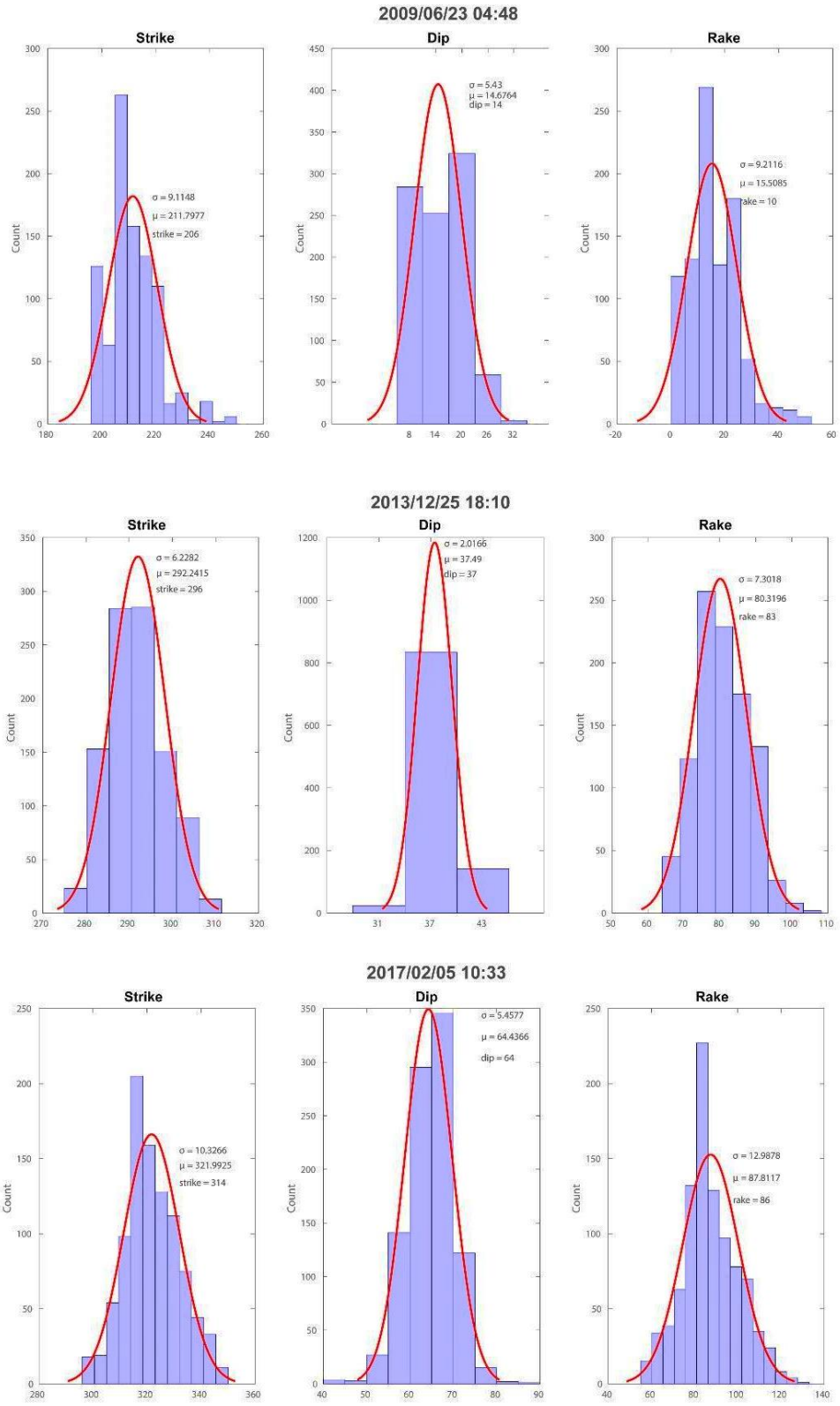


Figure 5.3. Bootstrap analysis of selected earthquakes.

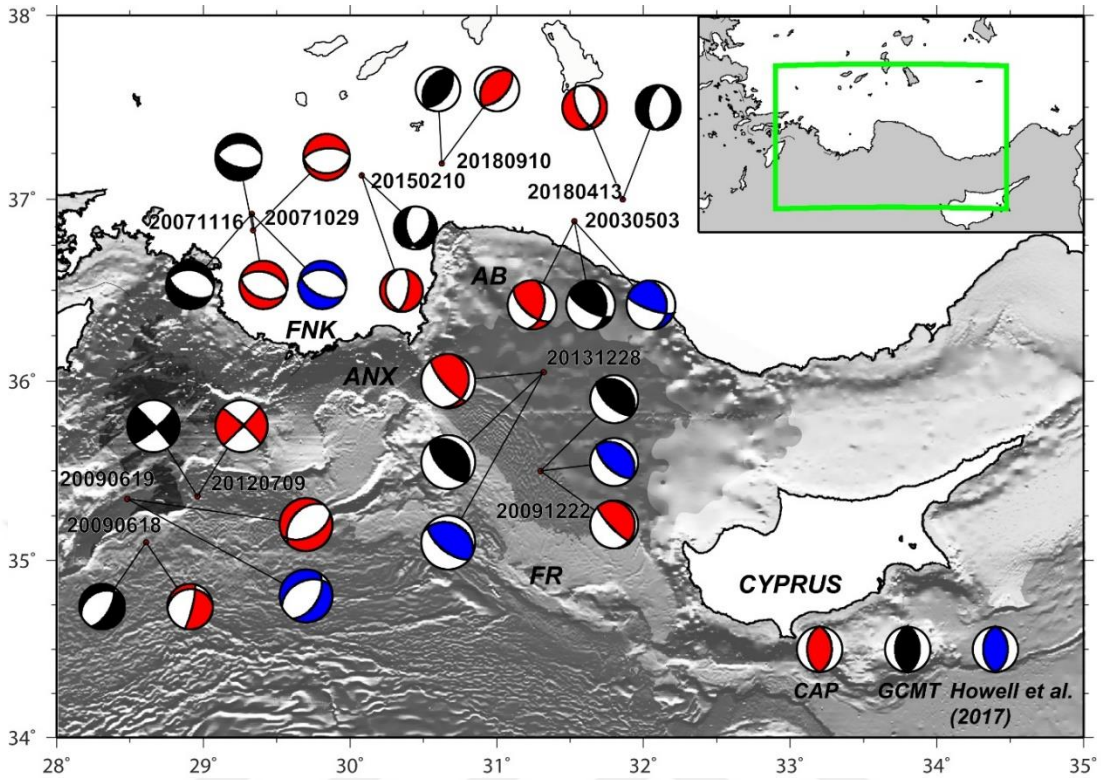


Figure 5.4. Comparison of the focal mechanisms solution in this study with solutions from GCMT and previous studies.

GPS velocities with the Nubia fixed reference frame are used to constrain the slip Confidential manuscript submitted to Tectonics vector directions by using the pole from Reilinger et al. (2006) (Figure 5.1). The density of GPS observations is low in the Antalya region and Isparta Angle and has better coverage towards the Hellenic arc. We used the SRTM30 topography database (Becker et. al., 2009). Bouguer gravity anomalies are computed from the EGM2008 (Palvis et. al., 2012) and the crustal thickness from Karabulut et al. (2019b) are also used for the analysis.

The teleseismic tomographic images are derived from Karabulut et al. (2019a). The travel time data are compiled from the waveforms recorded by the permanent and temporary networks operated in the study area between 2004 and 2019. We included the most recent data from CDCAT (Sandvol et. al., 2013), IS and CQ. More than 700 broadband stations are used in the analysis. The cross-correlation method is used for accurate estimates of arrival times. A total of 69600 direct P phases were picked on the

vertical components of broadband stations from 739 teleseismic events with magnitudes greater than 6.0 located at distances of 30–99◦. Residual times are calculated with respect to the AK135 velocity model. The region covers an area approximately 900 km in (E–W) and 500 km in (N–S) which is parameterized with a regularly spaced 3-D rectangular grid that starts at the surface and extends down to 700 km depth. The lateral node spacing is 50 km, and the vertical node spacing is 20 km. There are also other seismological observations that may contribute to the analysis of kinematics and geometry of the slab. The Pn velocity tomography is updated from Mutlu and Karabulut, (2011) by adding the earthquakes in the region with M > 5 since 2012 with increased number of stations. The resolution of the images improved significantly for the Antalya Bay and Cyprus region (Karabulut and Ozbakir, 2018). Since Pn tomography is sensitive to the velocity perturbations in the uppermost mantle, both the transitions between continental and oceanic lithosphere and low velocity zones as a result of slab tears can be identified. Furthermore, the upper mantle velocities of the 1D velocity models, which we use to calculate Green's functions, are improved by using the Pn velocity variations. The strain-rate calculations from GPS observations and Bouguer gravity anomalies are also used for shallow (crustal) and deep (mantle) interactions.

5.3. Results

We provide focal mechanism solutions for 50 earthquakes using regional waveforms from east of the Pliny-Strabo Trenches to the east of Cyprus. The earthquakes in this region have complex waveforms at local and regional distances. However, we were able to solve a significant number of new events (38 out of 50 earthquakes) in the Antalya Basin by utilizing path dependent 1-D velocity models (Figure 5.5). The unresolved earthquakes are mostly located around Cyprus Island which have complex waveforms due to scattering and path effects from 3D earth structures (Woodside et al., 2002; Veen et al., 2004; Aksu et al., 2009; Hall et al., 2013; Güneş et al., 2018). We present a large number of thrust mechanisms around the subduction interface and several strike-slip mechanisms both around the subduction zone and offshore of Finike, with $M_w >\sim 4.2$. The thrust mechanisms exhibit a clear pattern in NW-SE direction indicating compression along the plate boundary. The tomography images (Figure 5.5-a) down to ~200 km also

support the presence of a downgoing slab by an isolated high velocity anomaly which is coherent with the distribution of seismicity and thrust mechanisms.

To the west of the Isparta Angle, we obtained several crustal (depths < 20 km) normal mechanisms related to the dominant extensional forces in the region (Glover and Robertson 1998) (Figure 5.5-a). The strikes of these mechanisms change gradually from NS to EW from east to west. The spatial distribution of these mechanisms is in accordance with the location and the geometry of a round shaped, low P wave velocity anomaly reaching down to ~150 km in the tomographic cross sections along Profile 2. A topographic high in the 35 km filtered topography and Bouguer gravity low observed across Profile 2 suggest crustal response to the slab break off. The horizontal strain rate field calculated from the GPS velocities indicates double extensional strain rate field with a rotation from east to west which is consistent with the strikes of the normal mechanism earthquakes.

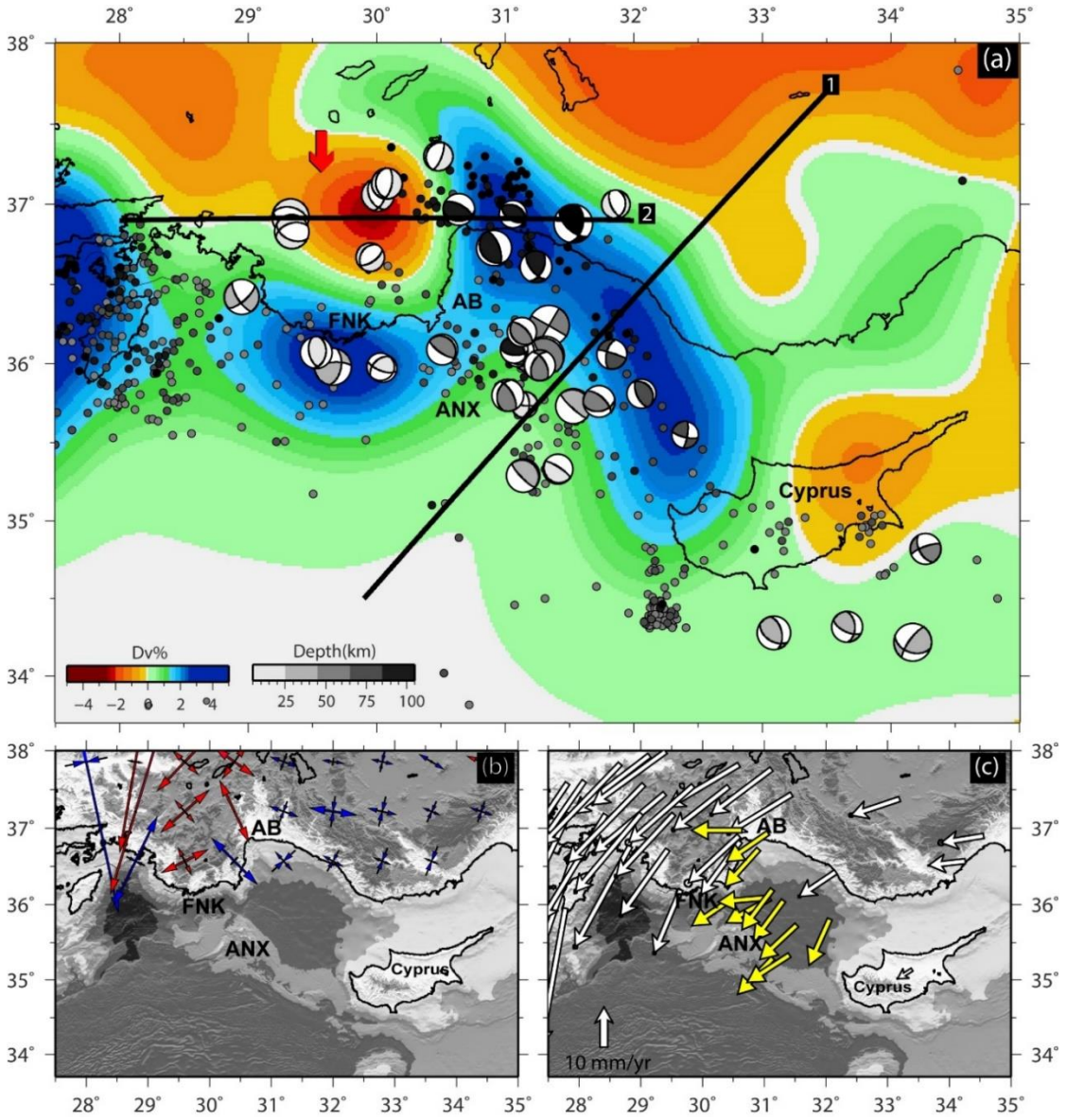


Figure 5.5. a) Earthquake source mechanisms around Antalya Basin obtained in this study. Seismicity is the same as in the Figure 5.1, colored by depth with M > 3.5. Earthquake source mechanisms are also colored by the same color scale. Solid black lines show the profile lines in Figure 5.6 and 5.8. In the background P wave velocity perturbations at 70 km depth from the tomography model of Karabulut et. al. (2019) and this study are shown where positive and negative anomalies are represented by hot and cold colors, respectively. b) Computed horizontal strain rate field. Red arrows show double extensional strain rates. c) White arrows indicate the GPS velocity vectors with respect to Nubia (Ergintav et. al, 2019). Yellow arrows show the slip vectors of thrust mechanisms.

5.4. Discussion

The active plate margin along the Eastern Mediterranean, from west of Rhodos island to the Dead Sea Fault, is composed of fragments of oceanic and continental crust, exhibiting small-scale subduction zones (e.g. Dercourt et al., 1986; Şengör & Natal, 1996; Royden & Faccenna, 2018). The Cyprus Subduction Zone has been separated from the Hellenic Subduction Zone by a tear across the Pliny-Strabo Trenches and ended to the east of Cyprus. As a result, the remnant of the subducting Nubian Plate under the Cyprus Arc, that is, the Antalya slab, appears to be isolated, fragmented and segmented). Understanding the behavior of such highly segmented slab in a heterogeneous lithosphere requires integrating various observations and coherent measurements as both geometry and kinematics are changing at short length scales.

In the following subsections, we analyze the deformation in the easternmost Mediterranean subduction as revealed from the new earthquake mechanisms in addition to teleseismic tomographic images reaching to the lower mantle with further constraints from GPS, gravity anomaly and topography for crustal depths.

5.4.1. The Remnant of Cyprus Subduction: Antalya Slab

New focal mechanisms, which are either pure thrust or thrust with a strike-slip component, indicate that the Antalya Slab deforms under dominant NE-SW oriented compressive forces, while the deformation to the west of the slab tear inboard of the Pliny-Strabo Trenches is dominated by extensional forces in the overriding Anatolian Plate and compressive forces on the subducting Nubian-Hellenic Arc plate interface (Shaw et al., 2010).

A possible explanation for compressive forces acting on the Antalya slab is the absence of the roll back along Antalya Slab, while western Anatolia is being pulled towards the SW by the roll back of the Hellenic slab (Figure 5.5-c) As a result, with the contribution of the slow rates of convergence along the easternmost part of the plate boundary, the Antalya slab is being compressed between Nubia and Anatolia as a passive block. The slip vectors of the earthquakes on the Antalya slab and the updated GPS

velocity field from Ergintav et al., (2019) are in the same direction indicating that the deformation of Antalya Slab is taken up in a direction parallel to the motion of Anatolia (Figure 5.5-c). Moreover, the P axis plunge angles of earthquakes are parallel to the apparent slope of the seismicity (Figure 5.7) and perpendicular to the Cyprus trench unlike the Hellenic arc, where `the P axes are parallel to the trench direction (Shaw et al., 2010). Several earthquakes with strike-slip mechanisms, at varying locations and orientations in the same region, might be related to complexities associated with fragmentation of the Antalya Slab.

The high velocity body of teleseismic tomographic image at 50 km, provide constraints on the extension of the Antalya Slab (Figure 5.5-a). On the west, the slab is delimited by the tear almost aligned with the western coast of the Antalya Bay. The trace of this high velocity body has a subparallel orientation to the coastline of the Antalya Bay and extends to the center of Cyprus Island while losing its continuity in the east. Although the slab is not attached to the surface in the east of Cyprus it can still be observed in the transition zone.

The trace of the Cyprus trench from the bathymetry and gravity anomaly is not obvious as they are dominated by pronounced geological domains (Anaximander Mountains and the Florence Rise) and thick sediments. Nonetheless, the slab anomalies in Bouguer gravity anomaly and the tomography images indicate either a concave or a flat geometry between the west of Antalya Basin and the west of Cyprus where the Paphos Fault seems to be an interplate boundary separating Nubian block from Sinai block (Figure 5.10).

The consistency of different data sets implies two critical details of the geometry and related kinematics of the Antalya Slab:

1) The segmentation of the Cyprus Slab gave rise to the Antalya Slab.

2) Antalya Slab is compressed between Nubia and Anatolia as a passive piece of slab as a result of its being separated from the Nubian slab beneath the Aegean. As Anatolia is pulled toward the Hellenic trench, it generates the NE-SW compressive

motion along the Antalya slab leading to SE-NW striking topographic features (Figure S4-Area 1).

3) The Antalya Slab appears to have affected lithospheric deformation along the southern boundary of the Anatolian Plate.

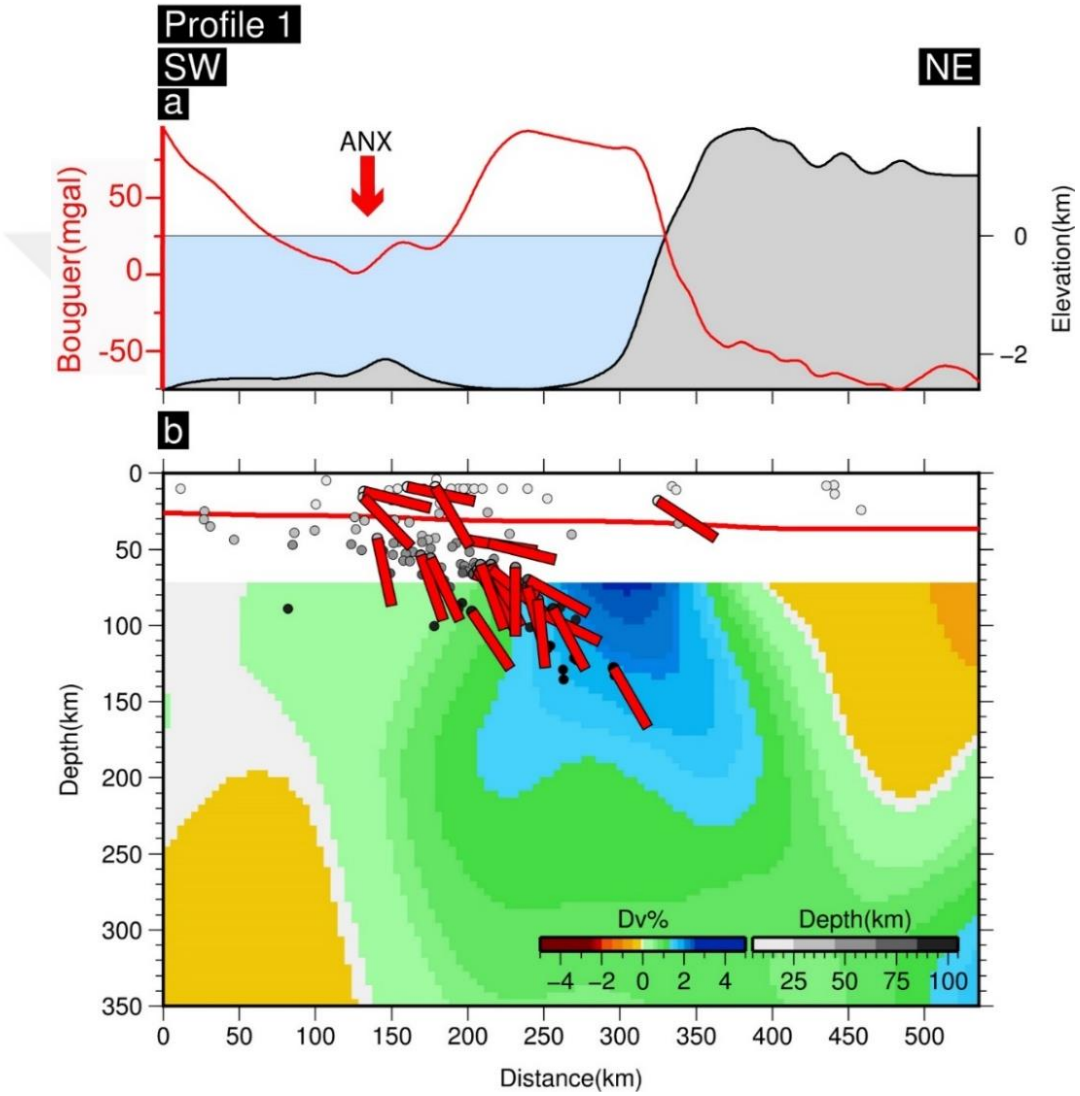


Figure 5.6. Topography, gravity anomaly and earthquake dip angles along Profile 1 in Figure 2 a. Gray and blue areas represent land and sea, respectively. Red solid line shows the Bouguer Gravity anomaly. b) The circles represent the seismicity with M > 3.5 and scaled by color with depth. Red bars indicate dip angles of computed mechanisms in Table 1. Positive and negative seismic P wave velocity perturbations of the tomography model are represented by hot colors and cold colors, respectively

(Karabulut et al., 2019). Red solid line refers to the crustal thickness (Karabulut et al., 2019). Red arrow marks the location of Anaximander Mountains in Figure 5.5-a.

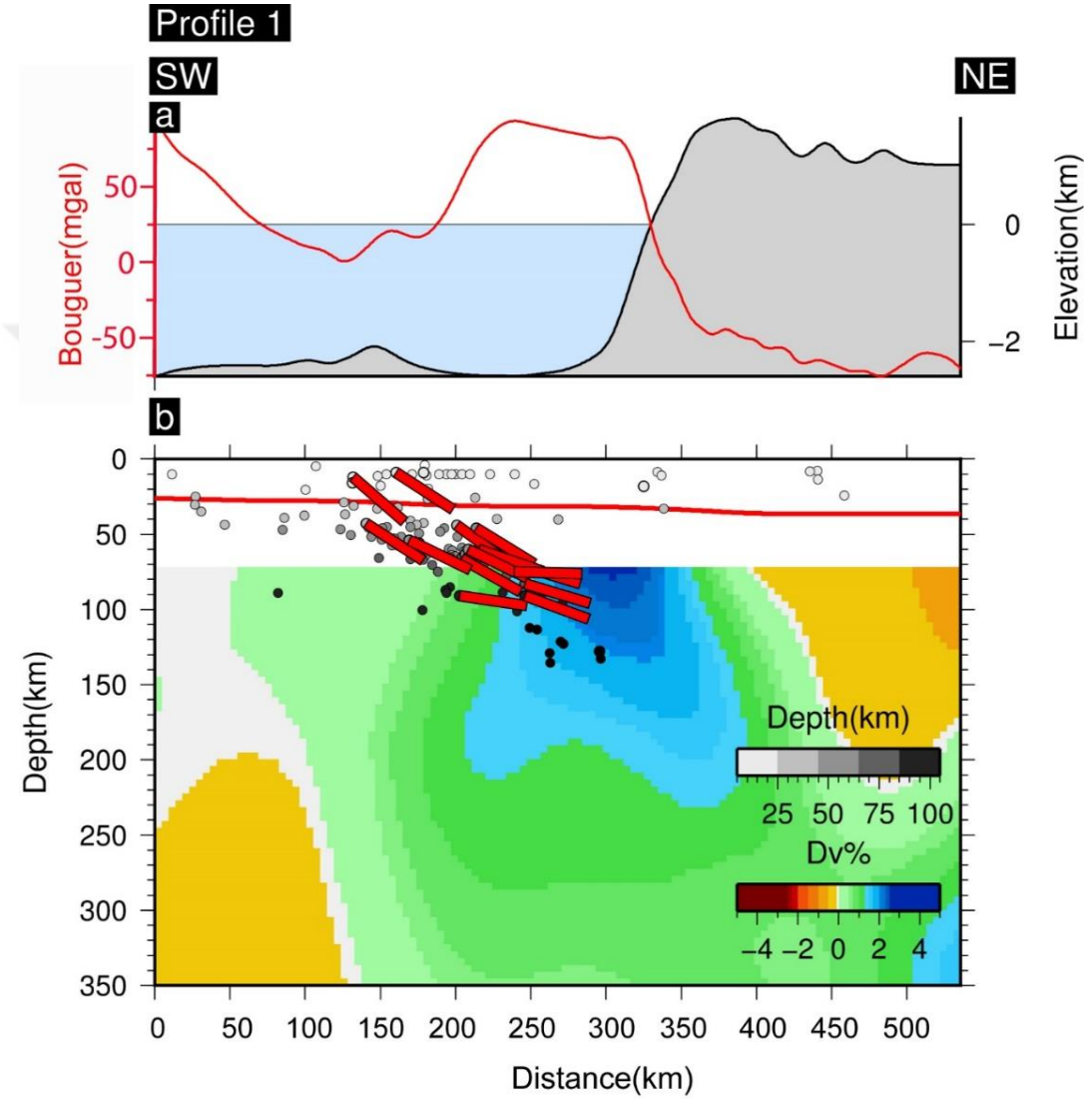


Figure 5.7. a) Gray area represents the topography and bathymetry while the red solid line shows the Gravity anomaly. b) The circles represent the seismicity with M>3.5 and scaled by color with depth. White arrows indicate P axes plunge angles. Positive and negative seismic P wave velocity perturbation is represented by hot colors and cold colors respectively (Karabulut et al., 2019). Red solid line refers to the crustal thickness (Karabulut et al., 2019).

5.4.2. A Localized Extensional Deformation Zone at the Isparta Angle

To the west of Antalya Bay, a localized low velocity anomaly, down to ~150 km is observed in the tomographic images indicating a slab break-off associated with the slab tear of Pliny-Strabo Trenches (Figure 5.8). Considering the correlation (location and wavelengths) between topography and Bouguer gravity anomaly, we relate this low velocity anomaly to the ascending asthenospheric mantle through the slab window and propose that the slab break-off may have eventually created this dome shaped topographic high with extensional deformation radially in all directions (Figure 5.9, Box 3).

The earthquakes with normal mechanisms surrounding this topographic high do not show coherent orientations with the regional trend of NS extension. The strike directions of these earthquakes are significantly different from the ones in the Gökova Bay. The sudden change on the orientation of these earthquakes located on the continuation of the Gökova Bay indicate that the slab tear and the related slab break-off marks the diminishing effect of slab roll back to the east of Pliny-Strabo tear zone, as evidenced by the lack of extension in the crust.

The observations from focal mechanisms, topographic highs and Bouguer gravity lows, strain-rate calculations, and the tomographic images in this relatively small region, provide direct evidence for interactions between slab segmentation in the upper mantle and deformation of the crust. In fact, the seismic images of the upper mantle and crustal observations such as topography, crustal thickness and Bouguer gravity anomaly are coherent at large wavelengths (Figure 5.9, Box 1-2-3). This indicates that the lithospheric structure of the eastern Mediterranean region is evolving with the segmentation of the Cyprus slab.

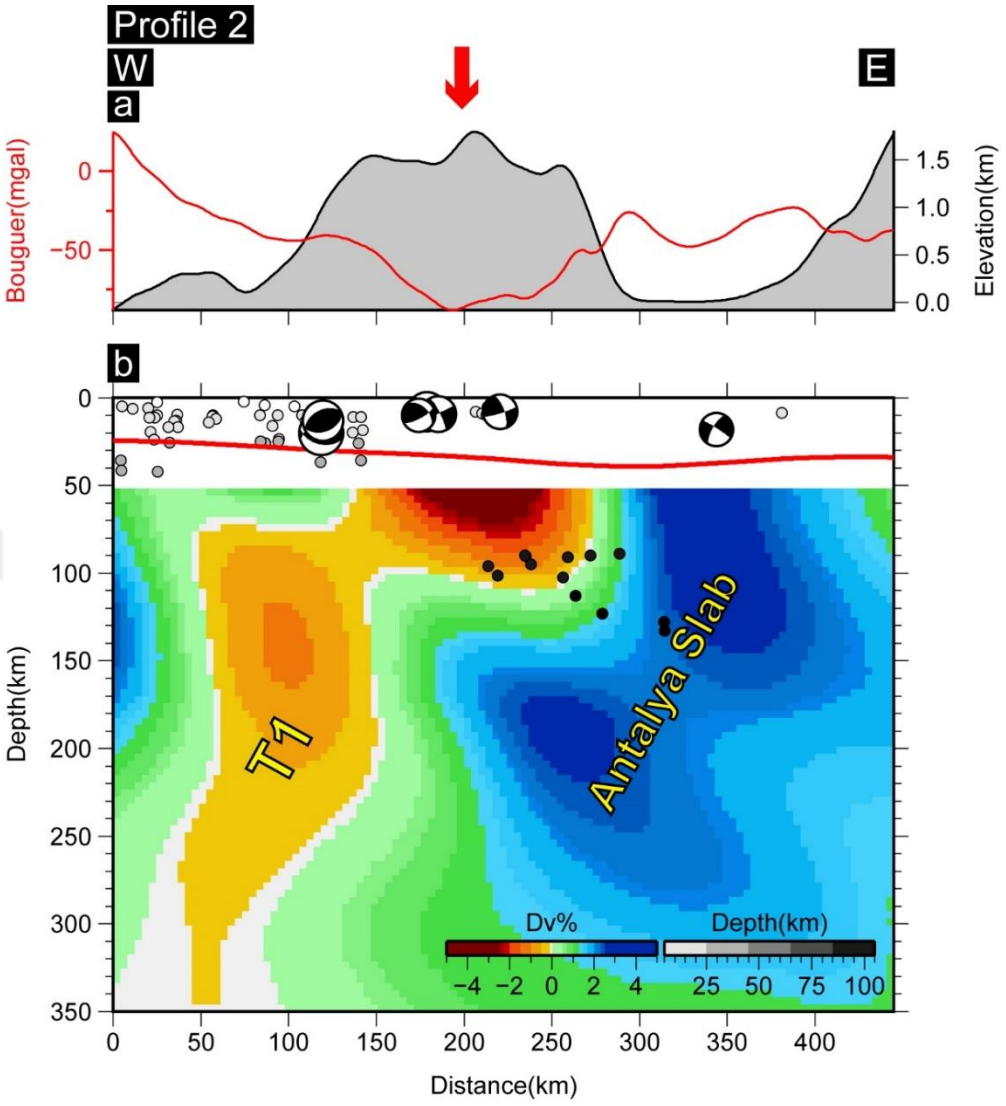


Figure 5.8. a) Topography, gravity anomaly and earthquake dip angles along Profile 2 in Figure 5.5. a) Gray and blue areas represent land and sea, respectively. Red solid line shows the Bouguer Gravity anomaly. Red arrow marks the location of the low velocity zone in Figure 5.5. b) The circles represent the seismicity with M > 3.5 and scaled by color with depth. Positive and negative seismic P wave velocity perturbations of the tomography model are represented by hot colors and cold colors, respectively (Karabulut et al., 2019). Red solid line refers to the crustal thickness (Karabulut et al., 2019). Beachballs repesent the normal mechanisms in Figure 5.5.

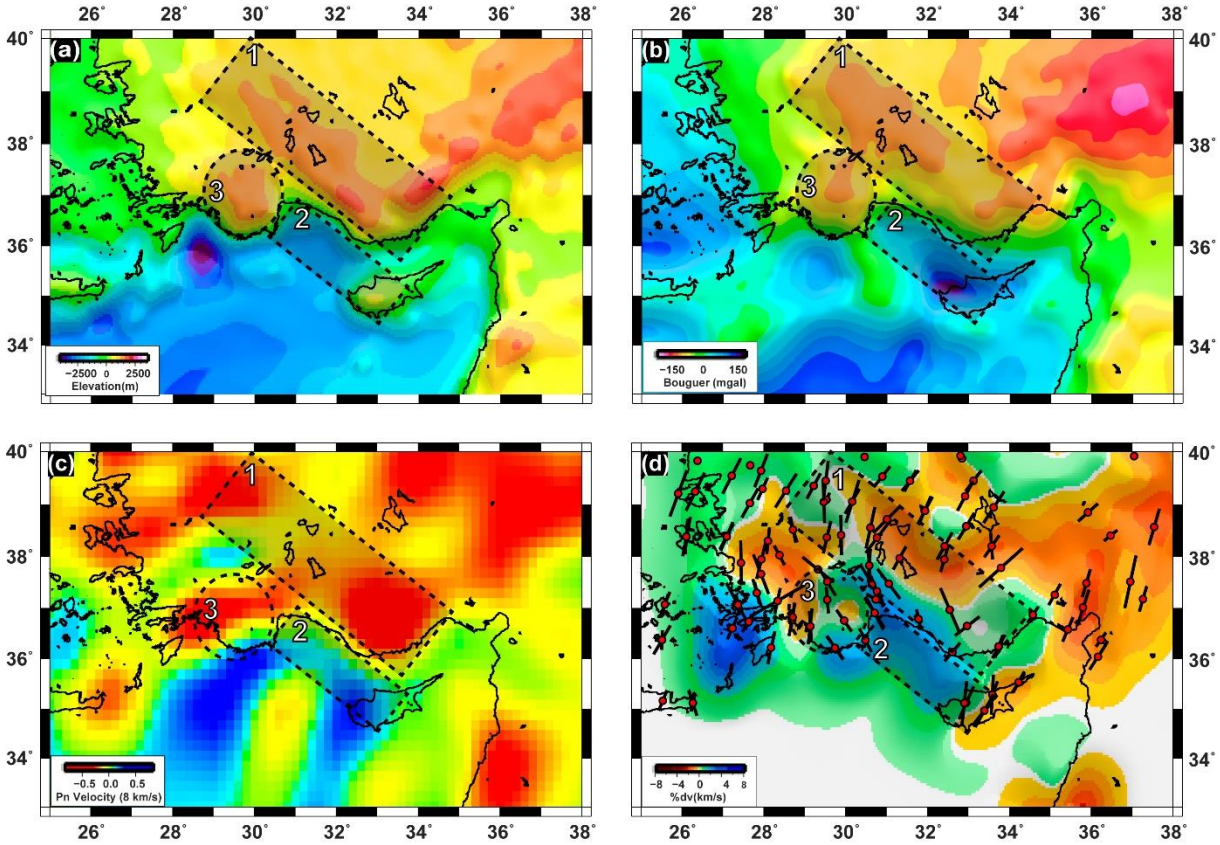


Figure 5.9. Topography, Bouguer gravity anomaly of the region 100 km filtered in a b and c respectively. d) Pn tomography from Mutlu & Karabulut (2011). e) Teleseismic tomography image at 100 km. All maps are shaded with a view angle of N45W. Main features are indicated by areas 1, 2 and 3.

The segmentation of the slab and the roll back are not only changing the lithosphere through the surrounding forces but also changing the rheology of the crust due to heat flow. Therefore, it is not surprising to observe very low shear wave velocities in the whole crust above the slab break off (See the group and phase velocity maps (less than 20 sec periods) of Cambaz and Karabulut, 2011; Delph et al., 2015).

The SKS anisotropy pattern in the whole Aegean-Anatolian domain shows significant deviations beneath Isparta Angle from its regional trend of NE-SW orientation (Paul et al., 2014) (Figure 5.9-d). The change in the anisotropy pattern may be related to the deviations of the mantle flow around the slab tears. Existence if the locally induced flow may also be forcing the overlying lithosphere upwards in addition to negative buoyancy of low density mantle.

The block models from GPS observations (Reilinger at al., 2006 Ergintav et al., 2019) explains well the internal deformation of the Anatolia region that in large part is accommodated by mapped, seismically active fault systems, indicating elastic behavior of the seismogenic upper crust (above ~20 km). Model fault slip rates are comparable to geologic rates, suggesting that major faults have controlled the recent geologic evolution of the region. On the other hand, the GPS residuals are relatively large in the region of Isparta Angle and along the Pliny-Strabo trenches suggesting the need for more detailed models in this complexly deforming area.

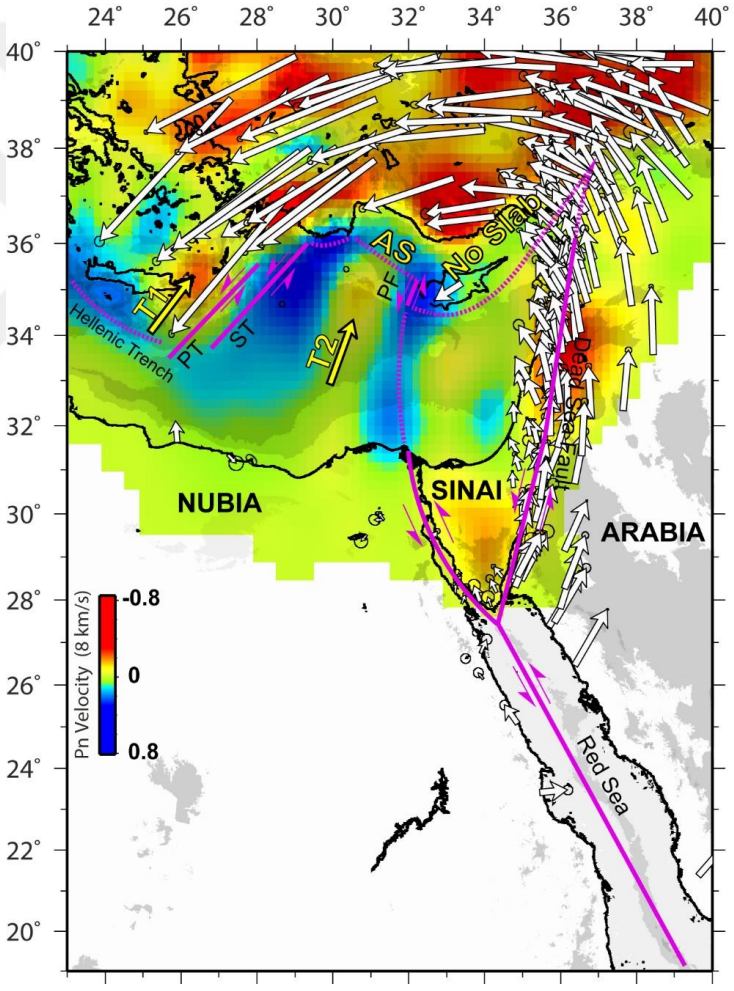


Figure 5.10. The plate boundary between Nubia-Anatolia-Sinai-Arabia. White arrows indicate the GPS velocity vectors with respect to Reilinger et al., (2006). Yellow arrows show the slip vectors of thrust mechanisms. AS: Antalya slab. T1: Tear 1. T2: Tear 2. Hot and cold colors refers to the Pn velocity change with respect to 8 km/s (Mutlu and Karabulut, 2011; Karabulut and Özdeğer, 2018).

6. SLIP DISTRIBUTION OF THE 2017 M_W 6.6 BODRUM-KOS EARTHQUAKE: RESOLVING THE AMBIGUITY OF FAULT GEOMETRY

6.1. Introduction

On July 20th, 2017, an M_w 6.6 earthquake occurred at the SW tip of Turkey, in Bodrum, causing two people's death, injuries of hundreds and resulted in intense damage around Bodrum Peninsula and Kos Island. Following the earthquake the region was hit by a local tsunami, reaching 1.4 m wave height (Heidarzadeh et al., 2017; Yalçıner et al., 2017).

The source mechanisms of the mainshock was reported as an EW striking normal fault in Gökova Bay which is consistent with the ongoing N-S extension in western Anatolia due to roll back of Hellenic subduction (Figure 6.1, see also McClusky et al., 2000 Figure 7). However, whether the earthquake occurred on the south dipping plane or on the north dipping plane was ambiguous due to different suggestions from different studies.

The first finite fault model after the mainshock used a south dipping fault plane derived from the coseismic GPS data (Saltogianni et al., 2017; Tiryakioğlu et al., 2017). They also observed that there is an uplift along the Bodrum coast. On the other hand, by the joint data from GPS and InSAR demonstrated considerable amont of negative displacement in the line of sight (LOS) direction from InSAR data on a small island called Karaada south of the Bodrum coastline which could only be explained by a north dipping fault (Ganas et al., 2017). Other studies such as Karasözen et al. (2018) also proposed that the earthquake ruptured a north dipping fault by evaluating horizontal GPS, InSAR and aftershock activity.

Kurt et al., (1999), defined the eastern Gulf of Gökova with multiple horst and graben structures by the reflection profiles from multichannel seismic data. To the west

of the gulf, surface expression of multiple south dipping faults are observed along with a north dipping fault, named Datça Fault. Ocakoğlu et al. (2018) argued that the surface expressions on the north of the Gulf belong to south dipping faults, while the ones on the southern margin of the gulf belongs to oblique left-lateral faults. The authors, depending on their findings, suggest that the 2017, Bodrum-Kos earthquake occurred on a south dipping fault.

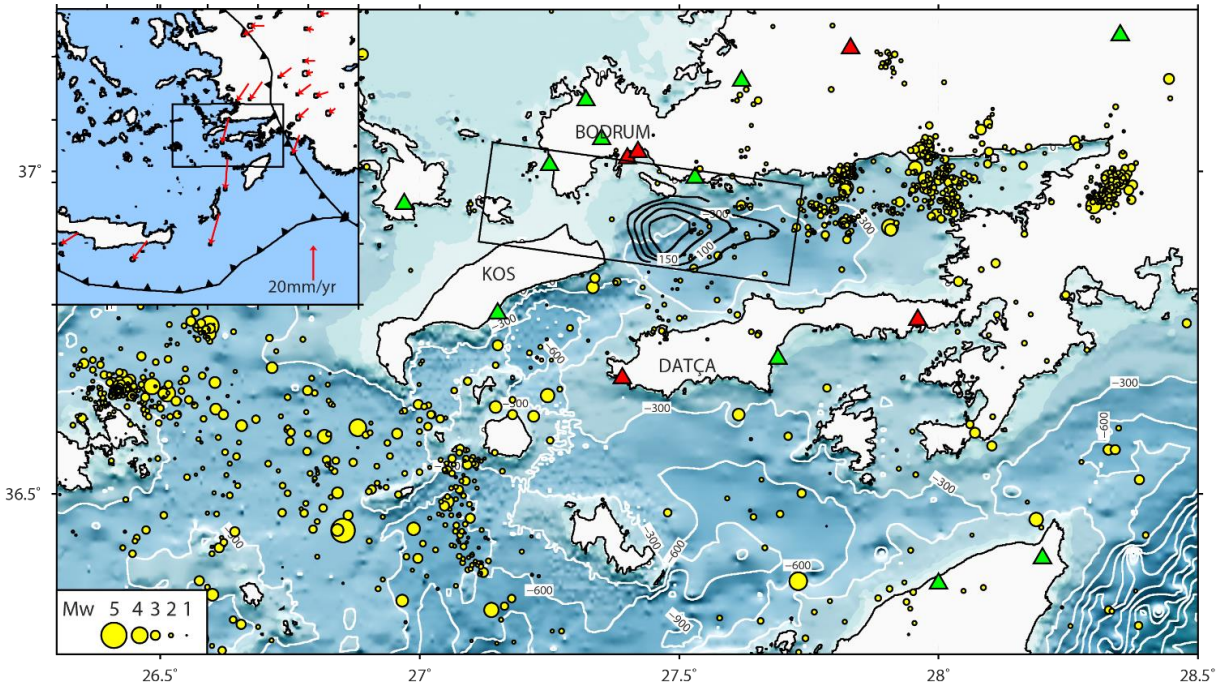


Figure 6.1. (Inset) Broader study area including the Hellenic Arc and the Aegean Sea region. The red vectors show selected annual GPS velocities with respect to Anatolia (Vernant et al., 2014). The black box shows the area of the main figure. (Main Figure) The study region of the 2017 Bodrum-Kos earthquake. The black circles filled with yellow show the seismicity between 2002 and 2008 (Bohnhoff et al., 2004; Brüstle, 2012) with magnitude scale on the bottom-left. The GPS stations used in this study are shown by green and red triangles for continuous and campaign sites, respectively. The black box represents the boundary of the best-fitting fault plane used for finite-fault modeling and the black enclosed curves show 50 cm slip contours for the best-fitting north-dipping slip mode

The 2017 event can potentially provide important information about identifying the faults that are currently active which accommodates the opening of Gulf of

Gökova.However, identifying whether the 2017 Bodrum-Kos earthquake ruptured a south-dipping or a north-dipping fault is challenging. First reason is related to the symmetrical horizontal and vertical displacements rising from a normal fault. This effect increases as the rupture does not arrive the surface or dip angle gets close to 45°. Second reason for the uncertainty is due to the fact that it is not possible to determine the dip direction from the aftershock distribution. Even the very early aftershocks of the 2017 earthquake are distributed over a large area rather than a single fault plane, making it impossible to identify the dip direction of the co-seismic fault.

The objective of this chapter is to identify the fault plane of July, 2017, M_w 6.6, Bodrum-Kos earthquake by making a precise relocation of the seismic activity during the first 20 days following the mainshock, solving focal mechanisms of large aftershocks and calculating the Coulomb stress transfer for both north and south dipping slip models from Konca et al., (2019). While the surface deformation from north and south dipping slip models both explain the surface displacements measured from InSAR and GPS data, their stress perturbation at depth can be quite different. Results show that the coseismic fault dips towards north.

6.2. Data

6.2.1. Aftershock Relocation

The seismicity of the first 20 days is relocated by joining catalogs of the General Directorate of Disaster Affairs of Turkey (AFAD), and Boğaziçi University Kandilli Observatory (KOERI) Regional Earthquake-Tsunami Monitoring Center (BDTIM) (Figure 6.2). While the phase readings of the same events from two catalogs were merged, the ones that exist in only one catalog are included too. Aftershocks occurred in the first 10 days are picked manually from the continuous waveforms (~1500 events). For the rest of the catalog, only catalogs from AFAD and KOERI are used. The joint catalog includes 2900 events from July 20 to August 7, 2017 (Figure 6.3). For the relocation process, the HYP code is used.

Once the locations are reliably obtained, a 1D minimum velocity models is derived from the latest catalog by minimizing the travel time errors using VELEST code (Kissling et al., 1994). Resulting 1-D crustal model is comparable with the velocity model from by Akyol et al. (2006). Variations from the 1D velocity model are implemented to the station corrections. Lateral and vertical uncertainties are in Figure 6.4.

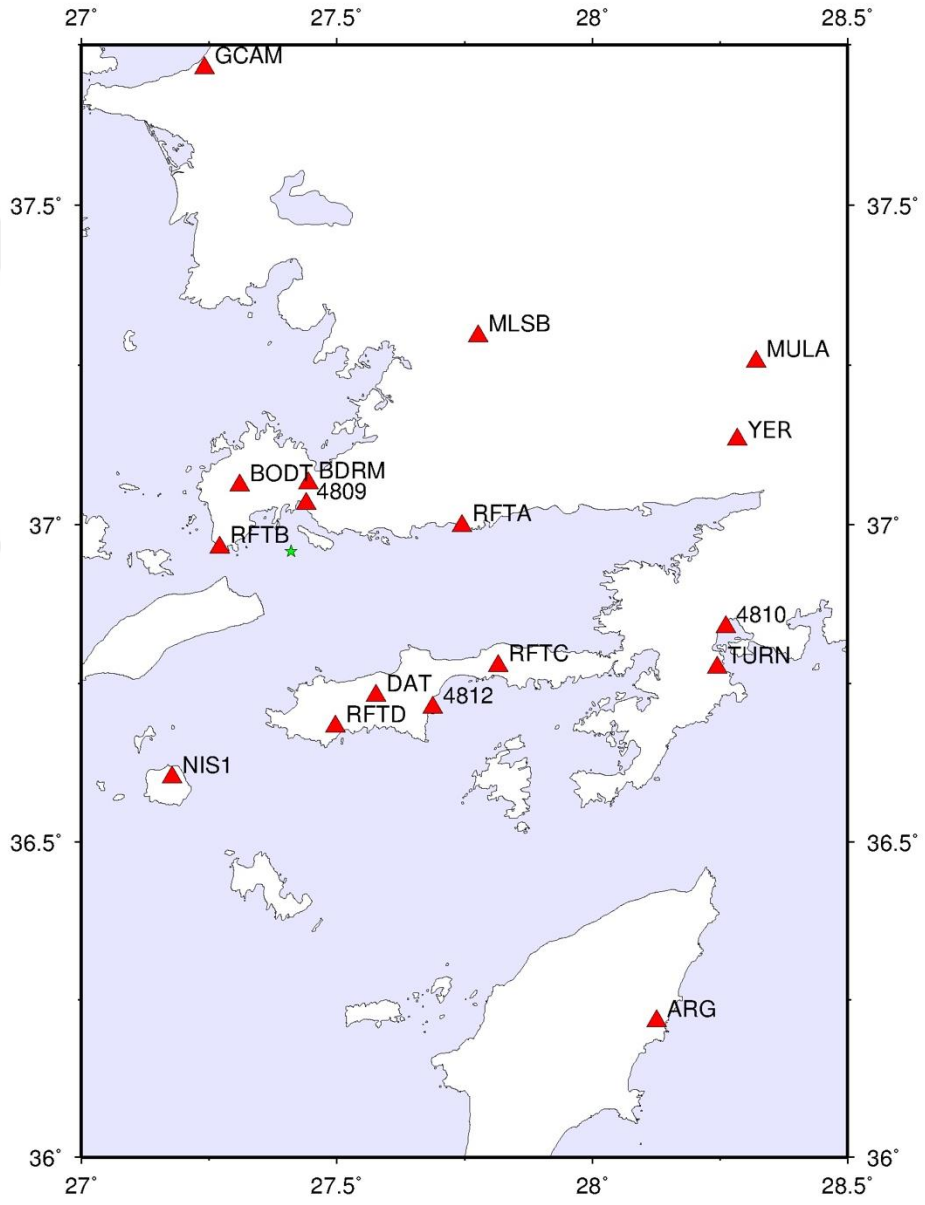


Figure 6.2. The distribution of the seismic stations used to locate the mainshock and aftershocks during the first month following the mainshock which are part of Kandilli Observatory and Research Institute (KOERI), General Directorate of Disaster Affairs of Turkey (AFAD), German Research Center (GFZ), Italian Seismic Network (INGV),

Seismological Network of Crete and Hellenic Unified Seismic Network (HUSN). (red triangles) . Green star shows the epicenter location.

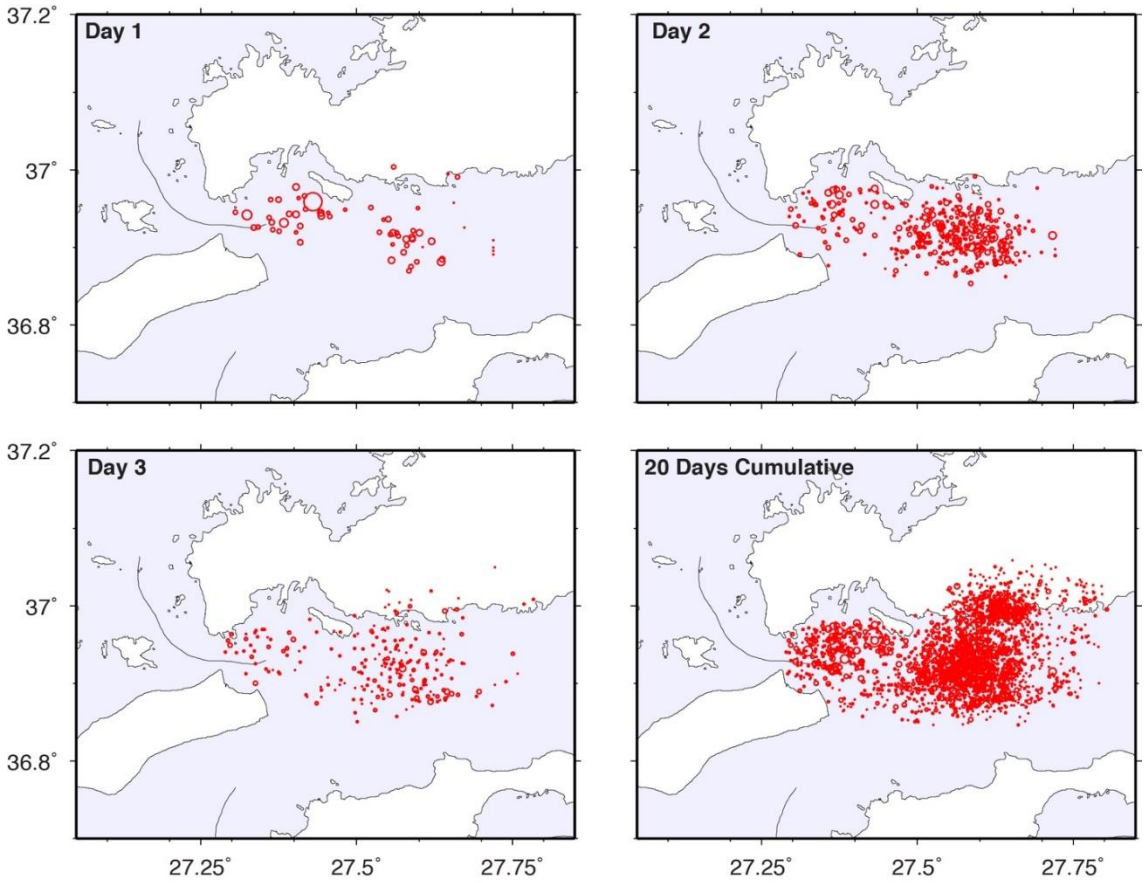


Figure 0.3. The evolution of the relocated seismicity following the mainshock during first 3 days and cumulative seismicity during the first 20 days.

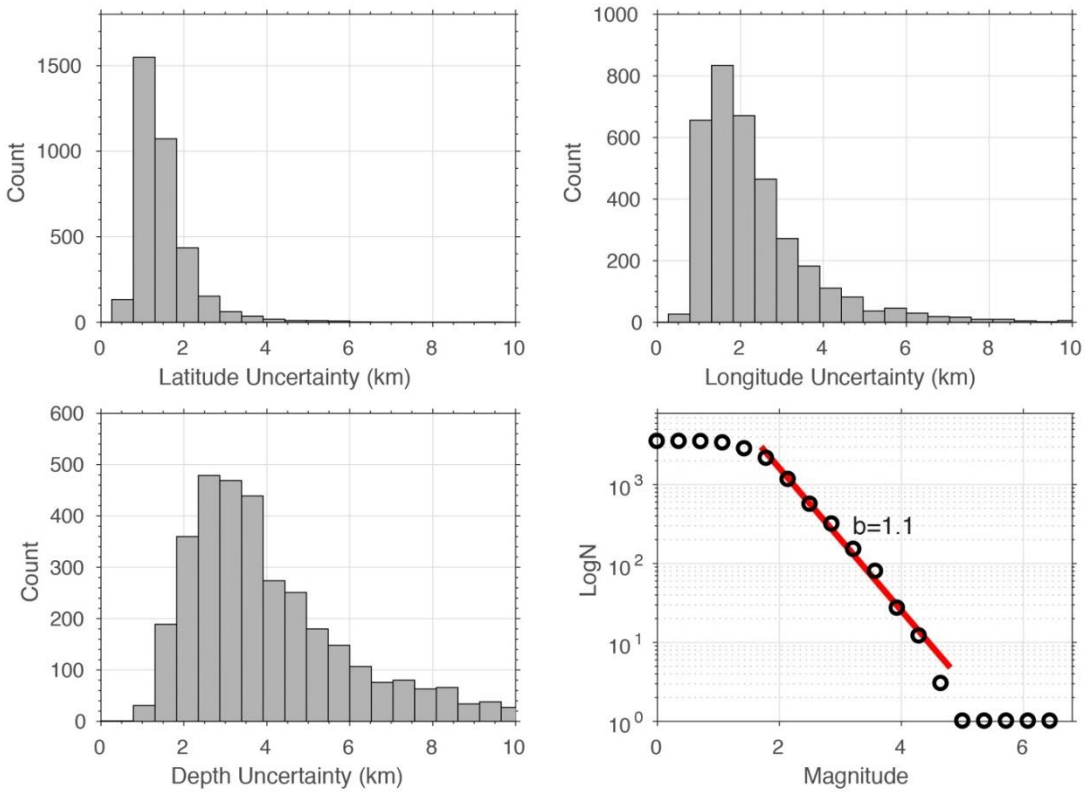


Figure 6.4. Statistics of the relocated aftershocks during the first 20 days following the July 20, 2017 Bodrum-Kos earthquake; (a) latitude; (b) longitude; (c) depth uncertainties. (d) Frequency-magnitude distribution and the best fitting b-value.

6.2.2. Aftershock Mechanisms

For the moment tensor inversion, gCAP algorithm of Zhu and Helmberger (1996), Zhu and Ben-Zion (2013) was employed using 83 broad-band stations at regional distances. For each event the number of station which are used varies depending on the magnitude and location of the earthquakes. The stations are from different networks as listed: Kandilli Observatory and Research Institute (KOERI), General Directorate of Disaster Affairs of Turkey (AFAD), German Research Center (GFZ), Italian Seismic Network (INGV), Seismological Network of Crete and Hellenic Unified Seismic Network (HUSN). Green's function library is created using the output velocity model from VELEST.

Except for some events with complex waveforms most of which occurred in a short time period after the mainshock, focal mechanism of 29 aftershocks with $6.6 > M_w > 4$

are calculated (Table C.3). An example of waveform fits is given in Figure 6.5. For the epicentral locations, joint catalog is used. Moreover, depths are redetermined from seismic waveforms by a choosing the best fitting focal mechanism solution of each aftershock after performing a grid search at 1 km intervals. The hypocentral depths deviate from the joint catalog in a narrow range of ±1km.

In order to check the stability of the moment tensor inversions, bootstrap analysis is applied to 3 aftershocks which has a variance reduction around 50%. 1000 inversions by selecting stations randomly are applied to selected earthquakes. Strike, dip and rake angle uncertainties lie within a range of 10° which proves the reliability of the solutions (Figure 6.6).

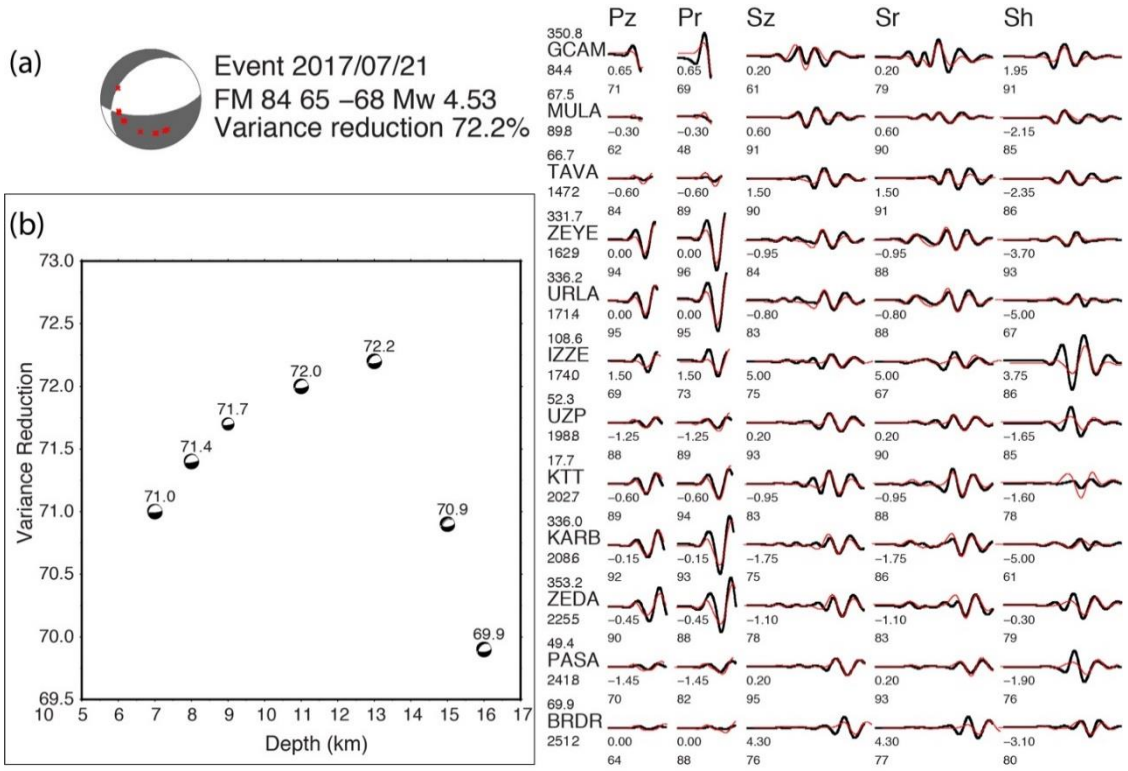


Figure 6.5. Result of an inversion of an M_w 4.5 aftershock that occurred a day after the mainshock. (a) (left) the best-fitting mechanism information and lower hemispheric projection of station locations. (right) Velocity waveform data (black) and model fits (red) for the P waves and S and surface wave windows. Station name, distance (km) and azimuth (°) are shown on the left of the traces. A band-pass filter between 0.02 Hz and 0.1 Hz for the 35 s Pnl window and 0.02–0.08 Hz for the 70 surface wave window was used. Grid search is performed to obtain the strike, dip and rake angles with 5° intervals and to the moment magnitude for a step size 0.1. Maximum time shifts were chosen as 2 s and 5 s for the P_{nl} and Surface wave components respectively. Station name, distance and azimuth of each station is shown on left of the waveforms. (b) Depth vs variance reduction and the best-fitting mechanism at each depth.

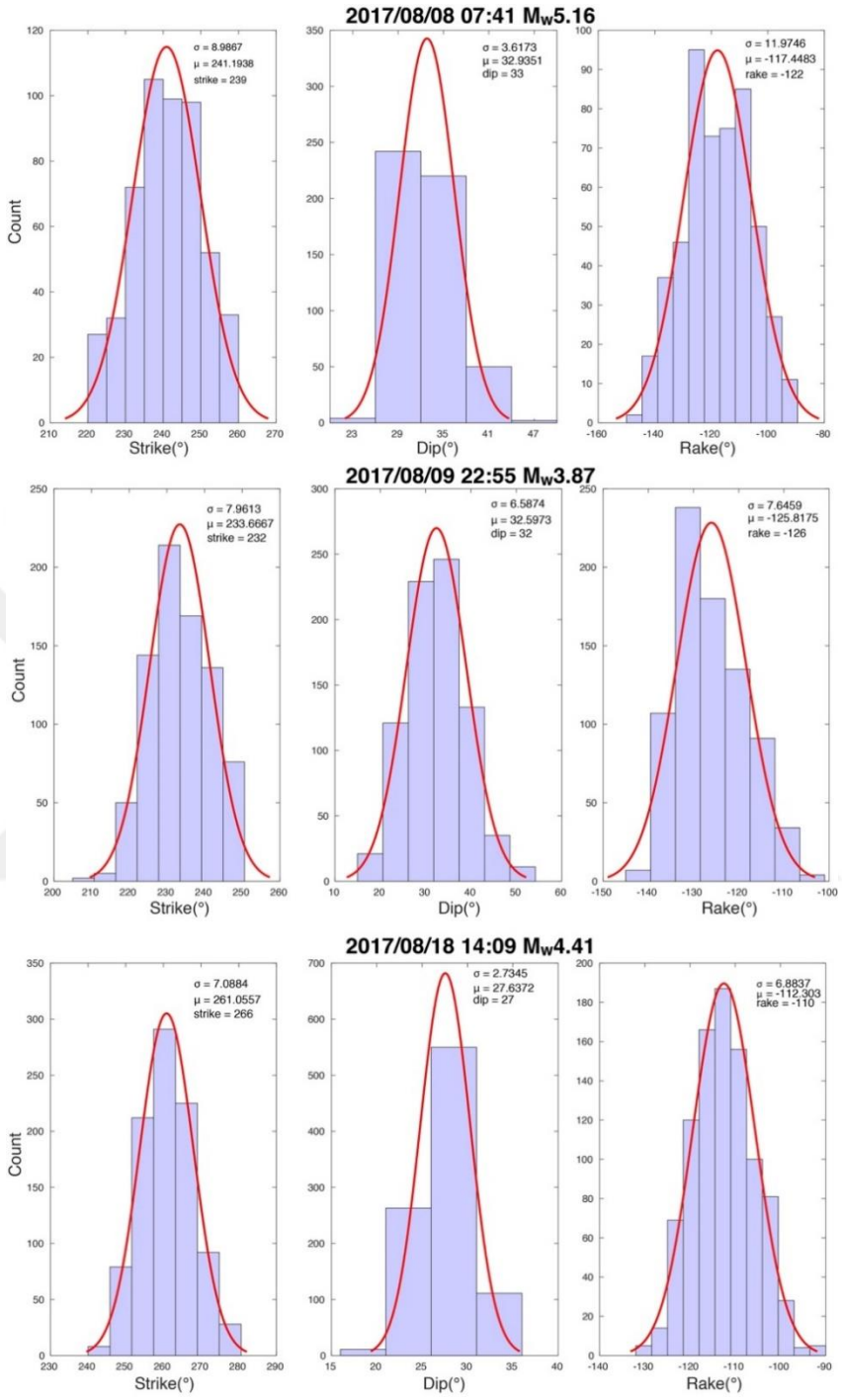


Figure 6.6. Bootstrap analysis of selected aftershocks with a variance reduction of ~50%. The date, time and magnitude of each earthquake is indicated at the top of the histograms for strike, dip and rake, respectively. By fitting a Gaussian curve, the average value (μ) and the standard deviation (σ) from the bootstrap analysis is calculated and displayed on top right of each plot. Strike, dip and rake values using all the data are also listed below the bootstrap results.

6.3. Results

6.3.1. Aftershock Locations and Mechanisms

Relocation of the seismic activity in the 20 days following the mainshock indicates that while the aftershocks that occurred in the first 3 days are located around the region with the highest slip, rest of the activity is located at the tips of the main rupture (Figure 6.7). Especially, in the first 24 hours following the mainshock, aftershocks tend to occur in the lateral termination of the highest slipping zone both towards east and west. The time evolution of relocated catalog demonstrates that the mainshock triggered neighboring faults with a time delay at distances as far as 40 km to north. The distribution of the aftershock mechanisms indicates that there are multiple E-W striking normal faults around the mainshock area, as suggested by previous studies (e.g. Karasözen et al., 2018). It is remarkable that several oblique mechanisms with strike slip component are observed to the NW of the main fault. The strike of these mechanisms are consistent with the faulting the region which is in a more NW-SE trend compared to its NE and N.

Figure 6.8 demonstrates geometric relationship between the crosssections and the two possible fault planes. The profiles to the west of the aftershock activity has a better correlation with the north-dipping fault plane compared to the south-dipping plane. Yet the depth distribution does not indicate a clear pattern, making it hard to put a constraint on the direction of the dip. The distributed seismic (~100 km) activity might be related to the activity which is triggered by the main shock. The hypocenter location is closer to the north-dipping fault (Figure 6.8-a) compared to the south-dipping fault (Figure 6.8-b), increasing the possibility of the north-dipping plane to be the ruptured one.

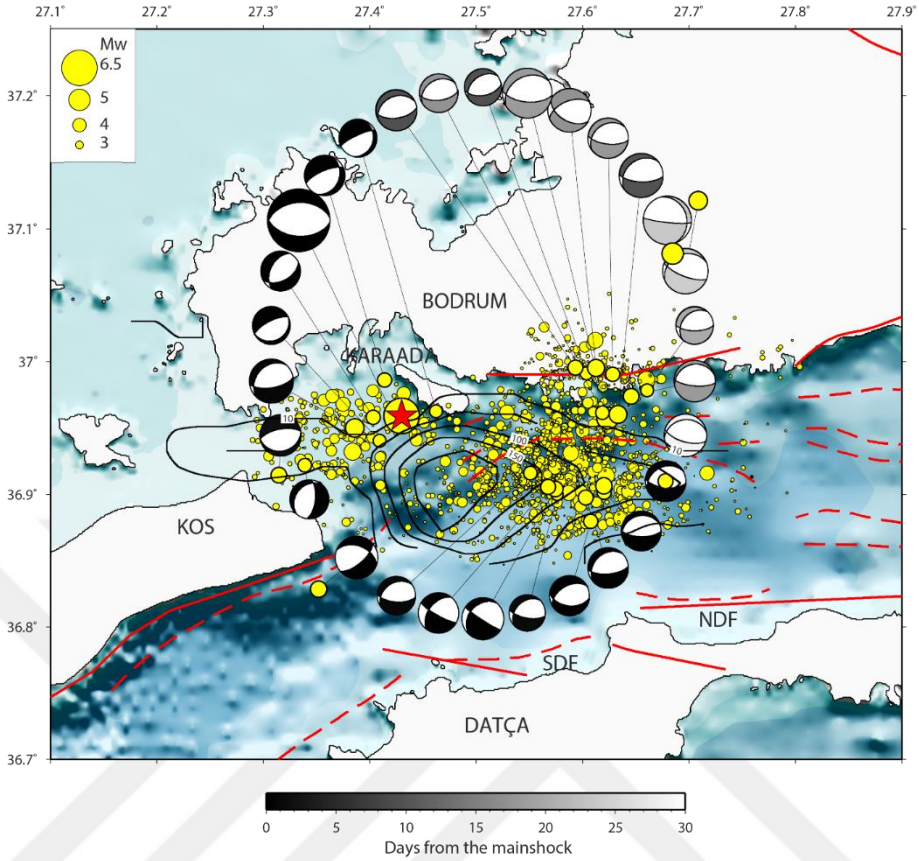


Figure 6.7. Map view of relocated mainshock, aftershock distribution and focal mechanisms. Focal mechanisms are colored in gray scale by their occurrence time and scaled in size by magnitude. Yellow circles show the epicenters of aftershock activity of the first 20 days in the vicinity of the main shock (M > 1). The outermost black contour outlines the fault area that slips more than 10 cm. The other black enclosed curves show slip contours at every 50 cm for the final north-dipping slip model. Solid red lines indicate active faults in the region from active fault map of General Directorate of Mineral Research and Exploration (Emre et al., 2013), while red dashed lines indicate faults from the study of Görür et al. (1995) and Kurt et al. (1999). Tick marks show the hanging wall of the identified normal faults from Kurt et al. (1999). SDF: South Datça Fault, NDF: North Datça Fault.

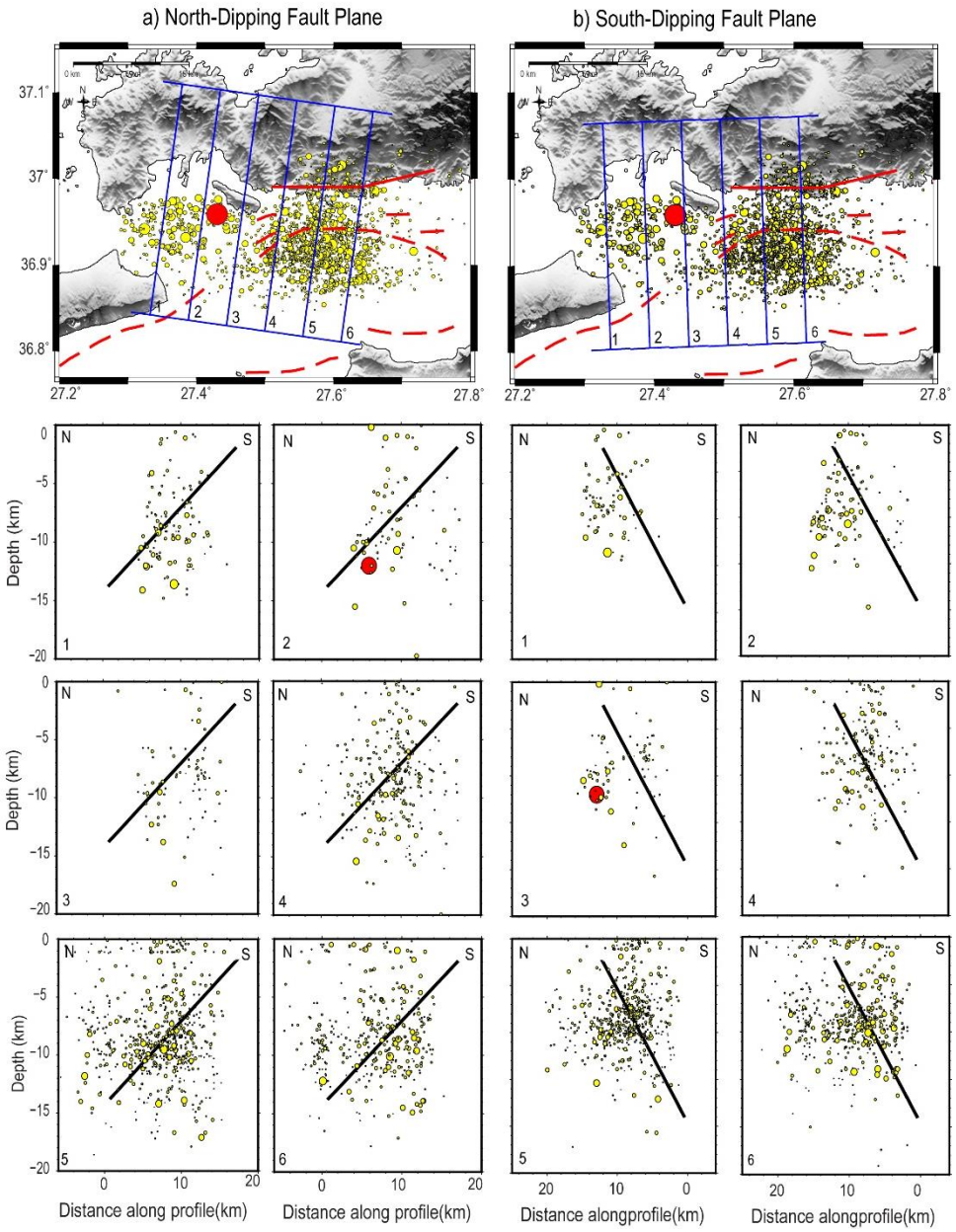


Figure 6.8. Seismicity distribution of the first 20 days with fault planes dipping to (a) north, and (b) south. Thick dashed lines show the fault plane. Red filled circle shows the location of the mainshock from this study. Each profile includes earthquakes within 2.5 km distance to the profile line in each direction. Red dashed lines show the fault lines from Emre et al. (2013) Görür et al. (1995) and Kurt et al. (1999).

6.3.2. Coulomb Stress Changes and Early Aftershock Distribution

Coulomb stress changes which are derived from different slip models, show variation with depth, providing a criterion for the choice of the fault plane. It is also critical to relate the seismic activity after the first several days and the coulomb stress changes to put constraints of the dip direction of the fault plane.

The south-dipping and north-dipping slip distributions both explain the geodetic data relatively well; however their stress perturbations close to the slip zone is quite different. In this study, we compare how the Coulomb stress changes of the two possible slip distributions fit the early aftershock locations.

Since the slip distribution of the mainshock is depth dependent, the Coulomb stress change is computed at varying depths (Figure 6.9). The stress changes obtained from the finite fault model of a north dipping fault is well-correlated with the distribution of the aftershocks in the first 5 days, verifying that the main rupture occurred on a north dipping fault. The difference between two models can clearly be observed especially at depth slices of 8 km and 10 km.

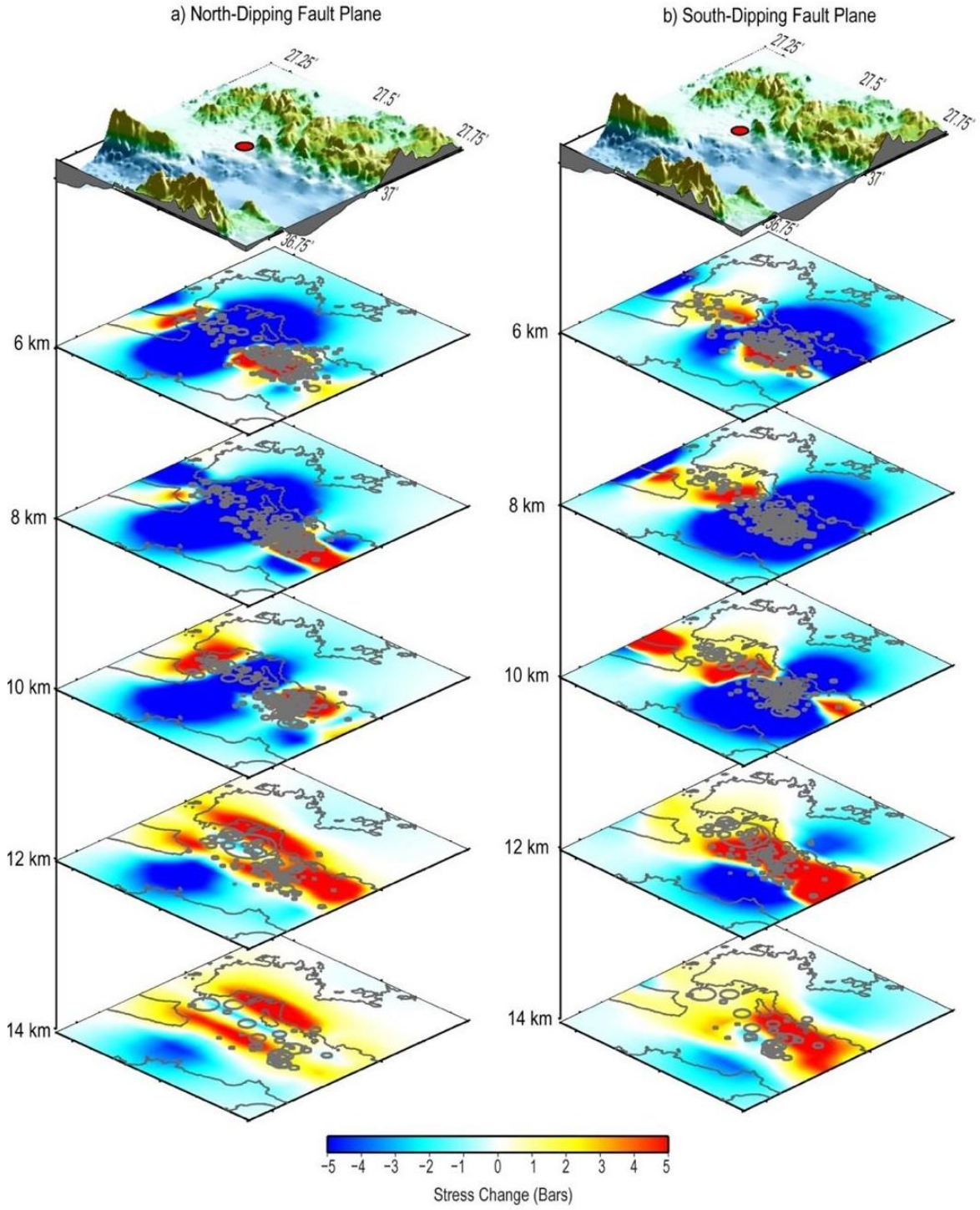


Figure 6.9. The Coulomb stress changes with the same mechanism as the mainshock for the (a) northdipping (left panel) and (b) south-dipping (right panel) faults at depths between 4-14 km. The gray circles show the aftershocks (M≥1) during the first 5 days following the mainshock (between 2017/07/20 and 2017/07/25). Coulomb stress changes are calculated on faults having the same mechanism as the mainshock.

6.3. Discussion

2017, Bodrum-Kos earthquake is one of the major events which is a consequence of the high rate of extension due to Hellenic roll-back (e.g., Royden and Faccenna, 2018). The change in the strikes of the earthquake mechanisms demonstrates the effect of the roll-back on the direction of crustal extension, which tends to rotate from a N-S motion to NW-SE motion from east to west. The aftershock distribution demonstrates that other faults in the region was triggered due to the stress release from the mainshock.

The distribution of the aftershocks is well-correlated with the north-dipping finite-fault model of Konca et al., 2019. Although the east of the Gulf of Gökova Bay is dominated by south-dipping faults, there is a north-dipping fault system which can be observed on the surface (Kurt et al., 1999). This fault lies along the southern margin of the Datça Peninsula where the thickness of the sediments reaches to ~3.5 The thickness increase toward the southern margin of the western Gökova Bay indicates that not only that the 2017 event ruptured a north dipping fault, but the north-dipping faults are the dominant that are actively extending the western section of the gulf.

An integrated analysis of the distribution of relocated aftershocks and new focal mechanisms along with the recent finite-fault solutions from Konca et al, 2019 shows that the a north-dipping plane better fits the data. Although the dip of the main fault is now determined, another point which remains to be answered is whether the ruptured occurred on the South Datça Fault or a result of the deformation in the Gökova Ridge and still needs to be further explored.

7. CONCLUSIONS

This study elucidates the fault interactions and lithospheric deformation in Anatolia-Aegean domain, especially in Eastern Mediterranean and Eastern Anatolia through focal mechanism solutions and also supporting seismological data such as tomographic images, fault slip models and geodetic observations.

In Chapter 4, the study of 2011 Van earthquake shows that three groups of aftershocks with strike-slip mechanisms are activated due to mainshock. Coulomb stress transfer calculated from the mainshock co-seismic slip also supported the triggering process. The seismicity and earthquake mechanisms demonstrate that the main fault is truncated by a N-S striking left lateral strike slip fault at the east. At the west of the main fault, while the seismicity is distributed over a broader area compared to the eastern end, still most of the earthquake source mechanisms have a considerable amount of left lateral strike slip component in NW-SE direction. Considering the short delay time of reactivation, several hours after the mainn shock, we propose that the mainshock rupture is terminated by two left lateral strike slip faults which are also activated due to the stress release from the main shock. This integrated system of faults with different mechanisms and strikes fits the post-seismic GPS vectors on the hanging wall in which move in opposite directions. The model also provides useful constraints for the post-seismic slip studies. In a next step, the post-seismic deformation can be explored to clarify the mechanism of this interaction. Overall this pattern of an almost E-W striking oblique thrust left-lateral fault, connected to N-S striking left lateral faults at each end are consistent with the N-S shortening due to collision of Arabia toward Eastern Anatolia.

In chapter 5, by using regional waveforms, the focal mechanism catalog north of Cyprus arc is significantly improved. This study demonstrates two remarkable results:

1) The Cyprus Subduction Zone has been delimited between the west of Cyprus and across Pliny- Strabo Trenches. The remaining slab piece continues to subduct and deform under compressive forces. The segmentation process appears to have affected the

regional lithospheric deformation leading to NW-SW oriented features in the topography and gravity (Figure S4, Areas 1-2-3). Slip vectors of earthquakes in this zone are consistent with the broad scale motion of Anatolia toward the Hellenic trench revealing that the convergence beneath Antalya Bay is part of the motion of Anatolia toward the Hellenic Trench.

2) The tear (T1 in Figure S6) that separates the Cyprus Subduction Zone from the Hellenic Subduction Zone also involves a slab break-off. We interpret the topographic high and gravity low above the slab break-off to be the result of the upwelling of low density asthenospheric mantle.

The Nubia-Anatolia plate interface between the Hellenic and Cyprus arcs has evolved from a continuous subduction zone from Kefalonia to easternmost Anatolia, with significantly different lithospheric characteristics of both the subducting and over-riding lithosphere along strike. As a result of the long history of northward subduction, Anatolia is presently underlain by a thin mantle lithosphere and relatively weak lower crust hosting the brittle upper crust. The Cyprus Subduction Zone is in compression and as such is undergoing a similar type of deformation as that in eastern Anatolia. The subducting plate has been losing its momentum due to slab break-off, but still has the power of deforming the lithosphere during the last episode of the subduction process in the easternmost Mediterranean. Future work on this topic should continue to investigate the crustal and upper mantle structure in order to better understand the plate interactions, segmentation and corresponding effects on the overriding Anatolia-Aegean domain.

The sixth chapter provides a solution to the ambiguity of the fault plane of the 2017, Bodrum-Kos Earthquake which ruptured the western segment of the Gulf of Gökova. The inferences of this chapter mainly contains the consistency of the early aftershock distribution with the Coulomb stress change due to the coseismic slip distribution from Konca et. al., (2019). Results indicate that the 2017, Mw 6.6, Bodrum-Kos Earthquake ruptured a north-dipping fault with ~40° which is 20-25 km long, E-W striking normal fault. Considering the sediment thicknesses (Kurt et al, 1999) we suggest that the 2017 earthquake might be a reflection of long term deformation for the western segment of the gulf.

The three studies of this thesis cover three different effects of the boundary on Anatolia microplate due to the forces related to the Nubia's and Arabia's convergence toward Anatolia. In the eastern Anatolia, 2011 Mw 7.1 Van earthquake reveals a mechanism of fault interaction which accommodates N-S shortening due to convergence of Arabia with Anatolia. In the southwest Anatolia, 2017 Bodrum-Kos earthquake shows an example of how N-S extension due to roll back of Hellenic subduction is accommodated beneath Gulf of Gökova. Finally the main study of this thesis, covers the earthquake mechanisms east of the Hellenic arc. The earthquake mechanisms in this region show the transition from N-S extension to compression and how they relate to the slab segmentation.

REFERENCES

Aksarı, D., H. Karabulut and S. Özalaybey, “Stress interactions of three moderate size earthquakes in Afyon, southwestern Turkey”, *Tectonophysics*, 485, 141–153, 2010.

Aksu, A. E., J. Hall and C. Yaltırak, "Miocene-Recent evolution of Anaximander Mountains and Finike Basin at the junction of Hellenic and Cyprus Arcs, eastern Mediterranean", *Marine Geology*, 258, pp. 24-47, 2009.

Aksu, A. E., J. Hall and C. Yaltırak, "Dramatic Pliocene–Quaternary subsidence of the southern Rhodes Basin and concomitant north-tilting and uplift of the Anaximander Mountains, the junction of Hellenic and Cyprus arcs, eastern Mediterranean Sea", *Tectonophysics*, 762, pp. 121–143, 2019.

Aktar, M., H. Karabulut, S. Özalaybey and D. Childs, "A conjugate strike-slip fault system within the extensional tectonics of Western Turkey", *Geophysical Journal International*, 171, pp. 1363-1375, 2007.

Aktuğ, B., J.-M. Nocquet, A. Cingöz, B. Parsons, Y. Erkan, P. England, O. Lenk, M. A. Gurdal, A. Kilicoglu, H. Akdeniz, and A. Tekgul, "Deformation of western Turkey from a combination of permanent and campaign GPS data: Limits to block-like behavior", *Journal of Geophys. Res.*, 114, B10404, 2009.

Arpat, E., F. Saroğlu and H. B. Iz, "The 1976 Caldıran earthquake", *Yeryuvarı ve İnsan,* 2, pp. 29-41, 1977.

Barka, A.A. and K. Kadinsky-Cade, "Strike-slip fault geometry in Turkey and its influence on earthquake activity", *Tectonics,* 7, pp. 663–684, 1988.

Bijwaard, H., and W. Spakman, "Non-linear global P-wave tomography by iterated linearized inversion", *Geophysical Journal International*, 141(1), pp. 71–82, 2000.

Biryol B, C., S. L. Beck, G. Zandt and A. A. Özacar, "Segmented African lithosphere beneath the Anatolian region inferred from teleseismic P-wave tomography", *Geophysical Journal International,* 184, 3, pp. 1037-1057, 2011.

Bohnhoff, M., M. Rische, T. Meier, B. Endrun, D. Becker, H. P. Harjes, and G. Stavrakakis, "CYC-NET: a temporary seismic network on the Cyclades (Aegean Sea, Greece)", *Seim.Res.Lett.,* 75(3), pp. 352-359, 2004.

Brüstle, A., "Seismicity of the eastern Hellenic Subduction Zone", Ruhr-University, Bochum, 2012.

Cambaz, M. D. and H. Karabulut, "Love-wave group velocity maps of Turkey and surrounding regions", *Geophysical Journal International,* 181(1), pp. 502–520, 2010.

Delph, J. R., C. B. Biryol, S. L. Beck, G. Zandt and K. M. Ward, "Shear wave velocity structure of the Anatolian Plate: Anomalously slow crust in southwestern Turkey", *Geophysical Journal International,* 202(1), pp. 261–276, 2015.

Dercourt, J., M. Gaetani and B. Vrielynck, "Atlas Peri-Tethys Palaeogeographical Maps", *CCGM,* 2000, https://ccgm.org/en/atlases/189-atlas-of-peri-tethys-palaeogeographical-maps-.html

Dewey, J. F., and A. M. C. Şengör, "Aegean and surrounding regions: complex multiplate and continuum tectonics in a convergent zone", *Geological Society of America Bulletin,* 90(1), pp. 84–92, 1979.

Doğan, B. and A. Karakas, "Geometry of co-seismic surface ruptures and tectonic meaning of the 23 October 2011 M_w 7.1 Van earthquake (East Anatolian Region, Turkey)", *J. Struct. Geol.,* 46, pp. 99–114, 2013.

Doğan, U., O.D. Demir, Z. Çakır, S. Ergintav, H. Özener, M. A. Akoğlu, S. S. Nalbant and R. Reilinger, "Postseismic deformation follwoing the October 2011 Van

earthquake (Turkey): Evidence for for aseismic fault reactivation", *Geophys. Res. Lett.,* 41, pp. 2334–2341, 2013.

Dreger, D. S. and D. V. Helmberger, "Determination of source parameters at regional distances with three-component sparse network data", *Journal of Geophysical Research: Solid Earth,* 98(B5), pp. 8107–8125, 1993.

Durand, V., M. Bouchon, H. Karabulut, D. Marsan, J. Schmittbuhl, M. P. Bouin, M. Aktar and G. Daniel, "Seismic interaction and delayed triggering along the North Anatolian Fault", *Geophys. Res. Lett.,* 37(18), L18310, 2010.

Dziewonski, A. M., T. A. Chou and J. H. Woodhouse, "Determination of earthquake source parameters from waveform data for studies of global and regional seismicity", *Journal of Geophysical Research: Solid Earth,* 86(B4), pp. 2825–2852, 1981.

Efron, B., "Computers and the theory of statistics: thinking the unthinkable", *SIAM Review,* 21(4), pp. 460–480, 1979.

Ekström, G., M., Nettles and A. M. Dziewoński, "The global CMT project 2004-2010: Centroid-moment tensors for 13,017 earthquakes", Physics of the Earth and Planetary Interiors, 200-201, pp. 1-9 2012.

Elliott, J.R., A. C. Copley, R. Holley, K. Scharer and B. Parsons, "The 2011 M_w 7.1 Van (Eastern Turkey) earthquake", *J. Geophys. Res. Ocean,* 118, pp. 1619–1637, 2013.

Emre, O., T. Y. Duman, S. Özalp, H. Elmacı and F. Saroğlu, "Active fault map of Turkey with and explanatory text", *General Directorate of Mineral Research and Exploration. Special Publication Series,* 30, Ankara-Turkey, 2013.

Ergintav, S., M. Floyd, D. Paradissis, H. Karabulut, P. Vernant, F. Masson, I. Georgiev, A. Ö. Konca, U. Doğan, R. King and R. Reilienger, "Anatolia-Aegean at the

junction of ocean subduction and continental collision: Geodetic implications for the dynamics of E Mediterranean tectonics", *Tectonics*, 2019.

Feng, W., Z. Li, T. Hoey, Y. Zhang, R. Wang, S. Samsonov, Y. Li and Z. Xu, "Patterns and mechanisms of coseismic and postseismic slips of the 2011 M_w 7.1 Van (Turkey) earthquake revealed by multi-platform synthetic aperture radar interferometry", *Tectonophysics*, 632, pp. 188–198, 2014.

Fielding, E.J., P.R. Lundgren, T. Taymaz, S. Yolsal-Cevikbilen, and S. E. Owen, "Fault-Slip Source Models for the 2011 M 7.1 Van Earthquake in Turkey from SAR Interferometry, Pixel Offset Tracking, GPS, and Seismic Waveform Analysis", *Seismol. Res. Lett.*, 84, pp. 579–593, 2013.

Floyd, M. A., H. Billiris, D. Paradissis, G. Veis, A. Avallone, P. Briole, S. Mcclusky, J.-M. Nocquet, K. Palamartchouk, B. Parsons and P. C. England, "A new velocity field for Greece: Implications for the kinematics and dynamics of the Aegean", *J of Geophys. Res.*, 115, B110, 2010.

Ganas, A., P. Elias, V. S, P. Briole, V. Kapetanidis, I. Kassara, A. Barberopoulou, P. Argyrakis, Chouliaras, G and A. Moshou, "Co-seismic deformation and preliminary fault model of the July 20, 2017 M6.6 Kos earthquake", *Aegean Sea, Rep*, 2017.

Glover, C. and A. Robertson, "Neotectonic intersection of the Aegean and Cyprus tectonic arcs: Extensional and strike-slip faulting in the Isparta Angle, SW Turkey", *Tectonophysics*, 298, pp. 103-132, 1998

Govers, R., and M. J. R. Wortel, "Lithosphere tearing at STEP faults: Response to edges of subduction zones", *Earth and Planetary Science Letters*, 236, pp. 505-523, 2005.

Govers, R. and A. Fichtner, "Signature of slab fragmentation beneath Anatolia from full-waveform tomography", *Earth and Planetary Science Letters*, 450, pp. 10-19, 2016.

Görür, N., A. M. C. Şengör, M. Sakınç, O. Tüysüz, R. Akkök., E. Yiğitbaş, F. Oktay., A. Barka, N. Sarıca, B. Ecevitoğlu, E. Demirbağ, Ş. Ersoy, O. Algan, C. Güneysu and A. Aykol, "Rift formation in the Gökova Region, Southwest Anatolia: Implication for the Opening of the Aegeran Sea", *Geol. Mag.*, 132, pp. 637-650, 1995.

Güneş, P., A. E. Aksu and J. Hall, "Structural framework and deformation history of the western Cyprus Arc", *Tectonophysics*, 744, pp. 438-457, 2018.

Hackl, M., R. Malservisi and S. Wdowinski,"Strain rate patterns from dense GPS networks", *Natural Hazards and Earth System Sciences*, 9(4), pp. 1177–1187, 2009.

Heidarzadeh, M., Ö. Necmioğlu, T. Ishibe and A. C. Yalçıner, "2017 Bodrum–Kos (Turkey–Greece) M_w 6.6 earthquake and tsunami of 20 July 2017: a test for the Mediterranean tsunami warning system", *Geoscience Letters*, 4, pp. 31, 2017.

Hill, D.P. and S. G. Prejean, "Dynamic Triggering", *Treatise on Geophysics*, pp. 257–291, 2007.

Howell, A., J. Jackson, A. Copley, D. McKenzie and E. Nissen, "Subduction and vertical coastal motions in the eastern Mediterranean", *Geophysical Journal International*, 211, pp. 593–620, 2017.

Işık, S. E., A. O. Konca and H. Karabulut, "The seismic interactions and spatiotemporal evolution of seismicity following the October 23, 2011 Mw 7.1 Van, Eastern Anatolia, earthquake", *Tectonophysics*, 702, pp. 8-18, 2017.

Jackson, J. and D. McKenzie, "The geometrical evolution of normal fault systems", *Journal of Structural Geology*, 5(5), pp. 471–482, 1983.

Jolivet, L. and C. Faccenna, "Mediterranean extension and the Africa-Eurasia collision", *Tectonics*, 19(6), pp. 1095–1106, 2000.

Jolivet, L., C. Faccenna, B. Huet, L. Labrousse, L. Le Pourhiet and O. Lacombe, "Aegean tectonics: Strain localisation, slab tearing and trench retreat", *Tectonophysics*, 597, pp. 1–33, 2013.

Jost, M. L. and R. B. Hermann, "A student guide to and review of moment tensors", *Seism. Res. Lett.*, 60, 1989.

Kalafat, D., K. Kekovali, F. Akkoyunlu and Z. Öğütçü, "Source mechanism and stress analysis of 23 October 2011 Van Earthquake (M_w = 7.1) and aftershocks", *J. Seismol.*, 18, pp. 371–384, 2014.

Karabulut, H. and A. Değer Özbakır, "Pn tomography of the Eastern Mediterranean Region", *EGU General Assembly Conference Abstracts*, 20, pp. 8663, 2018.

Karabulut, H., D. Aksarı D., A. D. Özbakır and A. Paul, "A new P-wave tomographic model of the Aegean-Anatolia Domain and its implications for small scale dynamics", EGU General Assembly Conference Abstracts, 21, pp. 10365, 2019a.

Karabulut, H., A. Paul, A. D. Özbakır, T. Ergün and S. Şentürk, "A new crustal model of the Anatolia-Aegean domain: Evidence for the dominant role of isostasy in the support of the Anatolian plateau", *Geophysical Journal International*, 218, pp. 57-73, 2019b.

Karasözen, E., E. Nissen, P. Büyükakpınar, M. D. Cambaz, M. Kahraman, E. Kalkan Ertan, B. Abgarmi, E. Bergman, A. Ghods and A. A. Özacar, "The 2017 July 20 M_w 6.6 Bodrum–Kos earthquake illuminates active faulting in the Gulf of Gökova, SW Turkey", *Geophy. Jour. Int.*, 214(1), pp. 185–199, 2018.

King, G., S. Stein and J. Lin, "Static stress changes and the triggering of earthquakes", *International Journal of Rock Mechanics and Mining Sciences & Geomechanics Abstracts*, 32(2), pp. 50-51, 1995.

Kissling, E., W. L. Ellsworth, D. Eberhart-Phillips and U. Kradolfer, "Initial reference models in local earthquake tomography", *Journal of Geophysical Research,* 991, pp. 19635-196461, 994.

Koçyiğit, A., "New field and seismic data about the intraplate strike-slip deformation in Van region, East Anatolian plateau, E. Turkey", *J. Asian Earth Sci.*, 62, pp. 586–605, 2013.

Konca, A. O., "Rupture process of 2011 M_w 7.1 Van, Eastern Turkey earthquake from joint inversion of strong-motion, high-rate GPS, teleseismic, and GPS data", *J. Seismol.*, 19, pp. 969-988, 2015.

Konca, A. O., S. E. Güvercin, S. Özarpacı, A. Özdemir, G. J. Funning, U. Doğan, S. Ergintav, M. Floyd, H. Karabulut and R. Reilinger, "Slip distribution of the 2017 M w6.6 Bodrum–Kos earthquake: resolving the ambiguity of fault geometry", *Geophysical Journal International*, 219, pp. 911-923, 2019.

Kurt, H., E. Demirbağ and I. Kuscu, "Investigation of the submarine active tectonism in the Gulf of Gökova, southwest Anatolia–southeast Aegean Sea, by multi-channel seismic reflection data", *Tectonophys*, 305, pp. 477-496, 1999.

Liu, C., Y. Zheng, X. Xiong and R. Wang, "Rupture Process of the 23 October 2011 M_w 7.1 Van Earthquake in Eastern Turkey by Joint Inversion of Teleseismic, GPS and Strong-Motion Data", *Pure Appl. Geophys.*, 172, pp. 1383–1396, 2015.

McClusky, S., S. Balassanian, A. Barka, C. Demir, S. Ergintav, I. Georgiev, O. Gurkan, M. Hamburger, K. Hurst, H. Kahle, K. Kastens, G. Kekelidze, R. King, V. Kotzev, O. Lenk, S. Mahmoud, A. Mishin, M. Nadariya, A. Ouzounis, D. Paradissis, Y. Peter, M. Prilepin, R. Reilinger, I. Sanli, H. Seeger, A. Tealeb, M. Toksoz and G. Veis, "Global Positioning System constraints on plate kinematics and dynamics in the eastern Mediterranean and Caucasus", *J. Geophys. Res.*, 105(B3), pp. 5695-5720, 2000.

McKenzie, D., "Active tectonics of the Mediterranean region", *Geophysical Journal International,* 30(2), pp. 109–185, 1972.

McQuarrie, N., J. M. Stock, C. Verdel and B. P. Wernicke, "Cenozoic evolution of Neotethys and implications for the causes of plate motions", *Geophysical Research Letters,* 30(20), 2003.

Mutlu, A. K. and H. Karabulut, "Anisotropic Pn tomography of Turkey and adjacent regions", *Geophysical Journal International,* 187, pp. 1743 - 1758, 2011.

Ocakoğlu, N., P. Nomikou, Y. İşçan, M. F. Loreto and D. Lampridou, "Evidence of extensional and strike-slip deformation in the offshore Gökova-Kos area affected by the July 2017 M_w 6.6 Bodrum-Kos earthquake, Eastern Aegean Sea", *Geo-Marine Letters,* 38211, pp. 225, 2018.

Özbakır, A. D., R. Govers and R. Wortel, "Active faults in the Anatolian-Aegean plate boundary region with Nubia", *Turkish Journal of Earth Sciences,* 26, pp. 30-56, 2017.

Paul, A., H. Karabulut, A. K. Mutlu and G. Salaün, "A comprehensive and densely sampled map of shear-wave azimuthal anisotropy in the Aegean-Anatolia region", *Earth and Planetary Science Letters,* 389, pp. 14–22, 2014.

Perk, S., "1-D local crustal structures from seismological data in the Cyprus Subduction zone and Antalya Bay", MSc These, Boğaziçi University, Dep. of Geopyhsics, 2013.

Pilidou, S., K. Priestley, J. Jackson and A. Maggi, "The 1996 Cyprus earthquake: a large, deep event in the Cyprean Arc", *Geophysical Journal International,* 158(1), pp. 85-97, 2004.

Portner, D. E., J. R. Delph, B. C. Biryol, S. Beck, G. Zandt and A. A. Özacar, "Subduction termination through progressive slab deformation across Eastern Mediterranean subduction zones from updated P-wave tomography beneath Anatolia", *Geosphere.,* 14 (3), pp. 907-925, 2004.

Reilinger, R., S. Mcclusky, P. Vernant, S. Lawrence, S. Ergintav, R. Cakmak, H. Ozener, F. Kadirov, I. Guliev, R. Stepanyan, M. Nadariya, G. Hahubia, S. Mahmoud, K. Sakr, A. Arrajehi, D. Paradissis, A. Al-Aydrus, M. Prilepin, T. Guseva, E. Evren, A. Dmitrotsa, S. V. Filikov, F. Gomez, R. Al-Ghazzi and G. Karam, "GPS constraints on continental deformation in the Africa-Arabia-Eurasia continental collision zone and implications for the dynamics of plate interactions", *J. of Geophys. Res.,* 111, B05411, 2006.

Reilinger, R. and S. McClusky, "Nubia--Arabia--Eurasia plate motions and the dynamics of Mediterranean and Middle East tectonics", Geophysical Journal International, 186(3), pp. 971-979, 2011.

Rosenbaum, G., G. S. Lister and C. Duboz, "Reconstruction of the tectonic evolution of the western Mediterranean since the Oligocene", *Journal of the Virtual Explorer,* 8, pp. 107-130, 2002.

Royden, L. and D. Papanikolaou, "Slab segmentation and late Cenozoic disruption of the Hellenic arc", *Geochem. Geophys. Geosys.,* 12(3), 2011.

Royden, L. and C. Faccenna, "Subduction Orogeny and the Late Cenozoic Evolution of the Mediterranean Arcs", *Annual Review of Earth and Planetary Sciences,* 46, pp. 261-289, 2018.

Salamon, A., A. Hofstetter, Z. Garfunkel and H. Ron, "Seismotectonics of the Sinai subplate--the eastern Mediterranean region", *Geophysical Journal International,* 155(1), pp. 149-173, 2003.

Saltogianni, V., T. Taymaz, S. Yolsal-Cevikbilen, T. Eken, M. Gianniou, T. Ocalan, S. Pytharouli and S. Stiros, "Fault-model of the 2017 Kos-Bodrum (east Aegean Sea) M_w 6.6 earthquake from inversion of seismological and GPS data", Preliminary ReportRep., Istanbul Technical University, 2017.

Saroğlu, F., "Doğu Anadolu'nun neotektonik dönemde jeolojik ve yapısal evrimi", PhD Theses, İstanbul Universitesi Fen Bilimleri Enstitusu, 1985.

Saroğlu, F. and Y. Güner, "Doğu Anadolu'nun jeomorfolojik gelişimine etki eden ögeler", *Turkiye Jeol. Kur. Bult.,* 24/2, pp. 39-50, 1981.

Şengör, A. M. C., "Turkiye'nin neotektoniğinin esasları", *Türkiye Jeoloji Kurumu Yayını,* 1980.

Sezgin, N. and A. Pınar, "Present day active tectonics of Eastern Turkey", The Tectonics of Eastern Turkey and the Northern Arabian Plate, 38, pp. 19, 2002.

Shao, G. and C. Ji, "Preliminary Result of the Oct 23, 2011 M_w 7.13 Turkey Earthquake", 2011.

Shaw, B. and J. Jackson, "Earthquake mechanisms and active tectonics of the Hellenic subduction zone", Geophysical Journal International, 181(2), pp. 966-984, 2010.

Şengör, A. M. C., C. Grall, C. İmren, X. Le Pichon, N. Görür and P. Henry, "The geometry of the North Anatolian transform fault in the Sea of Marmara and its temporal evolution: implications for the development of intracontinental transform faults", *Canadian Journal of Earth Sciences,* 51(3), pp. 222-242, 2014.

Taymaz, T., J. Jackson and R. Westaway, "Earthquake mechanisms in the Hellenic Trench near Crete", *Geophysical Journal International,* 102(3), pp. 695-731, 1990.

ten Veen, J. H., J. M. Woodside, T. A. Zitter, J. F. Dumont, J. Mascle and A. Volkonskaia, "Neotectonic evolution of the Anaximander Mountains at the junction of the Hellenic and Cyprus arcs", *Tectonophysics*, 391, pp. 35-65, 2004.

Tiryakioğlu, I., B. Aktuğ, C. Ö. Yiğit, H. H. Yavasoglu, H. Sözbilir, Ç. Özkaymak, F. Poyraz, E. Taneli, F. Bulut, A. Doğru and H. Özener, "Slip distribution and source parameters of the 20 July 2017 Bodrum-Kos earthquake (M_w 6.6) from GPS observations", *Geodin. Acta.*, 30(1), pp. 1-14, 2017.

Utkucu, M., "23 October 2011 Van, Eastern Anatolia, earthquake (M_w 7.1) and seismotectonics of Lake Van area", *J. Seismol.*, 17, pp. 783-805, 2013.

Vernant, P., R. Reilinger and S. McClusky, "Geodetic evidence for low coupling on the Hellenic subduction plate interface", *Earth and Planetary Science Letters*, 385, pp. 122-129, 2014.

Waldhauser, F., "hypoDD—A Program to Compute Double-Difference Hypocenter Locations", *U.S. Geological Survey Open-File Report*, 01-113, pp. 25, 2001, https://pubs.usgs.gov/of/2001/0113/

Waldhauser, F. and W. L. Ellsworth, "A Double-difference Earthquake location algorithm: Method and application to the Northern Hayward Fault. California", *Bulletin of the Seismological Society of America*, 90(6), pp. 1353-1368, 2000.

Wang, C., X. Ding, Q. Li, X. Shan, W. Zhu, B. Guo and P. Liu, "Coseismic and postseismic slip models of the 2011 Van earthquake, Turkey, from InSAR, offset-tracking, MAI, and GPS observations", *J. Geodyn.*, 91, pp. 39-50, 2015.

Wdowinski, S., Z. Ben-Avraham, R. Arvidsson and G. Ekström, "Seismotectonics of the Cyprian Arc", *Geophysical Journal International*, 164, pp. 176-181, 2006.

Wei, S., Z. Zhan, Y. Tan, S. Ni and D. Helmberger, "Locating earthquakes with surface waves and centroid moment tensor estimation", *J. Geophys. Res.* Solid Earth, 117, pp. 1-18, 2012.

Woodside, J. M., J. Mascle, A. A. C. Zitter, A. F. Limonov, M. Ergün and A. Volkonskaia, "The Florence Rise, the western bend of the Cyprus Arc", *Marine Geology,* 183(3-4), pp. 177-194, 2002.

Wortel, M. J. R., and W. Spakman, "Subduction and slab detachment in the Mediterranean-Carpathian region", *Science,* 290(5498), pp. 1910-1917, 2000.

Wortel, R., R. Govers and W. Spakman, "Continental collision and the STEP-wise evolution of convergent plate boundaries: From structure to dynamics", Subduction Zone *Geodynamics,* pp. 47-59, 2009.

Zhao, L. S. and D. V. Helmberger, "Source estimation from broadband regional seismograms", *Bulletin of the Seismological Society of America,* 84(1), pp. 91-104, 1994.

Zhu, L. and Y. Ben-Zion, "Parametrization of General Seismic Potency and Moment Tensors for Source Inversion of Seismic Waveform Data", *Geophy. Jour. Int.,* 194(2), pp. 839-843, 2013.

Zhu, L., and D. V. Helmberger, "Advancement in source estimation techniques using broadband regional seismograms", *Bull. Seismol. Soc. Am.,* 86, pp. 1634-1641, 1996.

Zhu, L. and X. Zhou, "Seismic moment tensor inversion using 3D velocity model and its application to the 2013 Lushan earthquake sequence", *Phys. Chem. Earth,* A/B/C, pp. 1-9, 2016.

Zor, E., "The crustal structure of the East Anatolian plateau (Turkey) from receiver functions", *Geophys. Res. Lett.,* 30, pp. 2-5, 2003.

APPENDIX A

Table A.1. Source parameters (strike, dip and rake angles and moment magnitude) obtained in Chapter 4. (**r**. Relocated events; *. Centroid depth)

Date	Time	Lat^{o}	Lon^{o}	Depth(km)	Strike^{o}	Dip^{o}	Rake^{o}	M_w
23.10.2011	11:27	38,840	43,310	5,70	266	44	-75	4,91
23.10.2011	12:13	38,790	43,160	6,70	167	53	84	4,38
23.10.2011	12:17	38,770	43,600	14,70	334	51	72	4,54
23.10.2011	12:20	38,730	43,540	20,40	224	34	10	4,64
23.10.2011	12:26	38,300	43,710	5,70	239	45	90	4,29
23.10.2011	12:30	38,730	43,230	7,10	35	72	42	4,35
23.10.2011	12:42	38,680	43,150	19,40	217	65	25	4,47
23.10.2011	14:02	38,760	43,710	11,40	169	39	80	4,02
23.10.2011	15:14	38,650	43,060	9,00	259	51	64	3,73
r*23.10.2011	15:24	38,610	43,180	13,00	231	39	40	4,49
23.10.2011	15:51	38,770	43,170	28,80	350	81	43	3,68
r23.10.2011	15:57	38,710	43,300	12,60	214	46	78	4,22
23.10.2011	17:08	39,070	42,240	10,20	234	38	75	3,69
23.10.2011	17:16	38,660	43,150	10,00	285	37	66	3,31
r23.10.2011	18:10	38,670	43,150	10,00	97	51	90	5,20
r23.10.2011	19:06	38,730	43,360	24,40	339	8	-14	4,71
23.10.2011	19:25	38,660	43,180	15,70	64	51	39	4,11
23.10.2011	19:48	38,680	43,000	10,00	26	36	35	4,23
23.10.2011	20:45	38,640	43,120	28,00	102	56	78	5,65
23.10.2011	21:20	38,900	43,540	10,00	190	74	29	4,16
23.10.2011	21:47	38,600	42,990	13,10	199	60	51	3,79
23.10.2011	22:21	38,620	43,070	17,50	240	69	28	4,56
*23.10.2011	23:34	38,590	43,520	15,10	61	29	75	4,07
23.10.2011	23:37	38,740	43,210	12,70	72	71	77	3,64
24.10.2011	00:50	38,730	43,310	5,70	196	28	14	4,03
24.10.2011	01:39	38,750	43,340	16,00	261	42	-15	4,05
r24.10.2011	08:28	38,570	43,460	22,00	251	54	84	4,63
24.10.2011	08:49	38,710	43,580	20,00	208	57	85	4,87
24.10.2011	11:14	38,750	43,400	13,50	149	60	78	4,01
24.10.2011	15:28	38,690	43,150	16,00	72	59	76	4,85
24.10.2011	18:52	38,700	43,220	15,30	273	41	76	4,00
*24.10.2011	23:15	38,670	43,540	14,00	22	36	49	3,72
r24.10.2011	23:55	38,790	43,530	15,40	0	67	-57	4,42

25.10.2011	00:08	38,630	43,260	23,60	140	57	30	3,82
25.10.2011	02:33	38,750	43,170	18,30	249	52	68	4,04
Date	Time	Lat^{o}	Lon^{o}	Depth(km)	Strike^{o}	Dip^{o}	Rake^{o}	M_w
25.10.2011	02:49	38,670	43,220	7,20	240	60	47	3,79
25.10.2011	03:59	38,720	43,230	15,90	82	49	-36	3,84
25.10.2011	14:55	38,860	43,610	15,00	262	71	62	5,51
25.10.2011	15:16	38,920	43,790	22,80	211	79	10	4,12
25.10.2011	15:19	38,820	43,410	5,90	213	46	81	4,01
25.10.2011	16:50	38,820	43,640	14,80	28	69	1	4,17
*25.10.2011	16:56	38,680	43,440	10,00	195	54	67	4,29
*25.10.2011	18:14	38,840	43,400	15,30	24	62	0	3,87
*25.10.2011	19:43	38,780	43,380	13,90	41	31	70	4,15
*25.10.2011	23:25	38,710	43,320	13,80	281	26	65	3,85
*26.10.2011	02:59	38,740	43,610	11,50	225	58	26	4,16
*26.10.2011	12:05	38,740	43,490	13,50	257	29	69	4,16
28.10.2011	00:25	38,560	43,170	25,40	35	55	26	4,15
28.10.2011	07:00	38,590	43,210	13,40	94	60	27	3,45
*28.10.2011	09:47	38,730	43,590	13,20	205	65	31	4,28
29.10.2011	03:52	38,590	43,210	11,00	49	64	21	4,42
29.10.2011	12:18	38,750	43,260	13,50	111	62	75	3,71
r29.10.2011	18:45	38,650	43,180	10,10	87	64	78	4,21
*30.10.2011	04:29	38,750	43,300	15,80	234	38	70	3,74
31.10.2011	16:57	38,730	43,430	10,90	276	69	66	3,66
05.11.2011	03:23	38,710	43,240	13,70	254	76	-61	4,12
06.11.2011	02:43	38,940	43,560	10,00	182	71	-21	4,48
07.11.2011	06:45	38,670	43,130	9,00	74	81	-13	3,60
08.11.2011	19:34	38,800	43,470	17,40	281	86	45	4,33
*2011.11.08	22:05	38,770	43,660	16,10	261	41	66	5,13
09.11.2011	02:20	38,600	43,200	11,30	40	60	20	3,66
*2011.11.09	19:23	38,440	43,280	13,40	176	72	-27	5,59
09.11.2011	20:45	38,480	43,270	10,00	220	70	18	4,38
10.11.2011	05:43	38,480	43,280	8,10	17	82	30	3,86
11.11.2011	13:11	38,500	43,330	7,70	46	79	17	3,56
12.11.2011	14:49	38,510	43,300	5,80	20	77	7	3,69
r12.11.2011	18:20	38,660	43,190	19,00	56	79	42	4,47
12.11.2011	19:53	38,470	43,300	7,00	215	83	-15	3,94
13.11.2011	03:44	38,420	43,000	7,30	212	55	34	3,81
r2011.11.14	16:47	38,650	43,060	13,70	70	68	43	4,41
*21.11.2011	20:55	38,680	43,260	14,20	265	46	86	4,18
*r21.11.2011	21:00	38,700	43,220	15,10	96	57	90	4,32

r22.11.2011	03:30	38,630	43,230	19,70	79	50	50	4,46
22.11.2011	09:18	38,490	43,260	15,00	183	75	29	3,73

Table A.2. GCMT solutions of selected earthquakes

Date	Time	Lat	Lon	Depth(km)	Strike^o	Dip^o	Rake^o	M_w
23.10.2011	18:10	38.668	43.153	20,9	100	45	93	5,10
23.10.2011	20:45	38.640	43.120	12,0	111	50	96	6,00
24.10.2011	08:28	38.570	43.460	22,0	265	45	86	4,80
24.10.2011	08:49	38.712	43.585	20,2	268	41	94	4,80
24.10.2011	15:28	38.693	43.148	18,5	93	46	93	5,00
25.10.2011	14:55	38.861	43.606	14,4	264	43	94	5,60
06.11.2011	02:43	38.938	43.564	15,8	186	87	-26	4,70
08.11.2011	22:05	38.770	43.660	21,2	280	37	87	5,30

APPENDIX B

Table B.1. Calculated mechanisms in this study. Lines with asterisks show the mechanisms that are compared to other studies and GCMT solutions. Highlighted lines are not presented in the main text since they are out of the area of this study, still are resolved to provide a better understanding of uncertainty of our solutions. Bold and italic rows indicate the earthquake focal mechanism solutions to which we applied bootstrap analysis.

Date	Hour	Lat°	Lon°	Depth(km)	Strike°	Dip°	Rake°	M_w
03.05.2003*	11:22	36,88	31,53	128	132	60	50	5,4
09.05.2003	14:56	36,73	30,91	91	138	26	70	5,0
16.10.2004	15:28	34,28	33,09	43	123	48	57	4,7
29.10.2007*	09:23	36,92	29,33	20	111	45	-85	5,3
16.11.2007*	09:08	36,83	29,34	13	115	50	-59	4,8
18.06.2009*	04:26	35,10	28,61	28	246	34	-58	5,0
19.06.2009*	14:04	35,34	28,48	36	65	50	-74	5,8
23.06.2009	04:48	35,97	30,05	12	206	14	10	3,9
07.11.2009	03:12	36,06	31,83	83	287	84	31	4,2
24.11.2009	01:59	35,98	28,48	16	225	46	30	3,9
22.12.2009*	06:06	35,73	31,53	44	313	9	90	5,0
26.05.2010	14:21	36,67	29,95	10	57	61	-76	4,0
14.10.2010	09:07	36,07	29,53	22	166	53	75	4,5
16.03.2011	11:17	37,30	30,48	8	201	18	-90	4,1
04.09.2011	17:40	35,74	31,15	9	0	60	-6	3,7
12.01.2012	00:25	36,08	31,10	66	119	19	50	4,5
13.03.2012	10:43	35,33	31,41	9	123	12	90	4,3
11.05.2012	18:48	34,22	34,17	25	216	74	49	5,3
23.06.2012	18:46	35,80	31,02	56	330	65	66	4,5
25.06.2012	13:05	36,42	28,95	25	49	70	-21	4,9
09.07.2012*	13:55	35,36	28,96	71	313	84	177	5,7
28.07.2012	23:29	34,82	34,27	47	250	76	35	4,3
08.12.2013	17:30	36,61	31,24	89	141	62	45	4,5
25.12.2013	18:10	36,94	31,06	90	293	37	82	4,4
28.12.2013*	15:20	36,05	31,31	46	304	14	71	5,5
06.03.2014	15:14	35,99	31,27	63	331	58	50	4,3
05.05.2014	05:04	36,09	31,07	91	95	56	67	3,9
19.06.2014	20:29	35,81	32,06	70	320	29	76	4,1
10.02.2015*	08:55	37,13	30,08	9	10	64	-82	4,3

16.02.2015	11:52	37,06	30,01	12	15	53	-62	4,6
Date	Hour	Lat°	Lon°	Depth(km)	Strike°	Dip°	Rake°	M_w
30.07.2015	15:03	34,32	33,66	36	116	62	50	4,3
18.08.2015	21:19	35,29	31,14	43	136	78	90	4,7
06.10.2015	21:27	35,98	29,66	37	11	54	25	5,2
22.03.2016	13:24	35,76	31,73	63	80	39	45	4,5
19.10.2016	12:17	36,09	30,51	54	124	71	86	4,3
13.01.2017	21:42	35,55	32,40	75	103	74	14	3,8
05.02.2017	10:33	36,20	31,13	60	314	64	86	4,4
29.09.2017	16:07	36,97	30,64	90	90	26	64	4,5
13.04.2018*	17:54	37,00	31,86	18	9	33	-61	4,0
10.09.2018*	23:01	37,20	30,62	100	216	35	84	4,8
12.09.2018*	06:20	36,05	31,21	60	205	70	-17	5,2

Table B.2. Other studies. Bold line shows the earthquake source mechanism from *Jackson & McKenzie* (1977) others are from *Howell et al.* (2017).

Date	Hour	Lat°	Lon°	Depth(km)	Strike°	Dip°	Rake°	M_w
03.05.2003	11:22	36,88	31,53	128	119	69	60	5,4
29.10.2007	09:23	36,92	29,33	20	116	54	-78	5,3
16.11.2007	09:08	36,83	29,34	13	263	38	-108	5,1
18.06.2009	04:26	35,10	28,61	28	246	34	-58	5,0
22.12.2009	06:06	35,50	31,30	58	133	63	90	5,3
09.07.2012	13:55	35,36	28,96	71	318	87	170	5,7

Table B.3. GCMT solutions

Date	Hour	Lat°	Lon°	Depth(km)	Strike°	Dip°	Rake°	M_w
03.05.2003	11:22	36,88	31,53	128	119	69	60	5,4
29.10.2007	09:23	36,92	29,33	20	116	54	-78	5,3
16.11.2007	09:08	36,83	29,34	13	263	38	-108	5,1
18.06.2009	04:26	35,10	28,61	28	246	34	-58	5,0
22.12.2009	06:06	35,50	31,30	58	133	63	90	5,3
09.07.2012	13:55	35,36	28,96	71	318	87	170	5,7
28.12.2013	17:30	36,05	31,32	54	137	61	87	5,9
10.02.2015	08:55	37,13	30,08	9	32	44	-56	4,7
13.04.2018	23:01	37,00	31,86	24	7	36	-91	4,9
10.09.2018	14:02	37,20	30,62	100	212	40	86	4,9

APPENDIX C

Table C.1. Several point source mechanism solutions by global and local agencies.

	NP1 (stk°/dip°/rake°)	NP2(stk°/dip°/rake°)
Global CMT	278/36/-82	88/55/-96
AFAD	275/38/-80	82/53/-98
USGS	285/39/-73	84/53/-103
KOERI	286/53/-72	78/40/-112

Table C.2. The velocity model for the region obtained from earthquake relocations.

Depth (km)	Vp (km/s)	Vs (km/s)
0.0	3.15	1.73
2.0	4.84	2.77
4.0	5.40	3.09
6.0	5.71	3.28
8.0	5.85	3.36
10.0	6.02	3.46
12.0	6.13	3.51
16.0	6.20	3.56
20.0	6.50	3.75
30.0	7.38	4.25
37.0	7.85	4.33

Table C.3. Mechanisms of the mainshock and the aftershocks obtained in this study from regional seismic data.

Date	Hour	Lat°	Lon°	Depth(km)	Strike°	Dip°	Rake°	M_w
20.07.2017	22:31	36,96	27,43	12	94	48	-84	6,4
21.07.2017	00:15	36,96	27,4	10	64	49	-63	4
21.07.2017	00:52	36,94	27,4	10	66	20	-87	3,9
21.07.2017	00:56	36,88	27,6	8,6	96	48	-65	4,1
21.07.2017	01:24	36,92	27,46	10,5	245	77	-74	3,9
21.07.2017	01:34	36,9	27,56	14,2	119	79	-42	4,1
21.07.2017	01:37	36,9	27,57	9,5	123	84	-58	4,3
Date	Hour	Lat°	Lon°	Depth(km)	Strike°	Dip°	Rake°	M_w

21.07.2017	01:49	36,98	27,41	14,1	247	70	-70	4,1
21.07.2017	02:11	36,82	27,35	0,5	291	44	-37	4,4
21.07.2017	03:58	36,89	27,6	13,9	85	66	-72	4,2
21.07.2017	05:12	36,9	27,62	1	91	67	-84	4,1
21.07.2017	05:51	36,92	27,33	10,3	220	30	-60	4
21.07.2017	09:54	36,91	27,67	14,7	96	64	-74	4,2
21.07.2017	17:08	36,95	27,38	12,9	81	65	-71	4,5
22.07.2017	00:33	36,91	27,55	10,2	94	63	-70	3,9
22.07.2017	04:52	36,9	27,57	15,1	100	67	-62	3,7
22.07.2017	17:08	36,91	27,31	7,85	79	25	-90	4,2
30.07.2017	07:01	36,99	27,59	10,37	82	59	-81	4,2
30.07.2017	10:55	36,99	27,6	10,25	80	54	-73	3,8
30.07.2017	17:05	36,96	27,63	12,2	92	66	-71	4,5
07.08.2017	05:17	36,99	27,61	10,4	120	49	-50	4,5
07.08.2017	05:43	36,96	27,61	11,87	84	60	-77	4,01
07.08.2017	18:24	36,99	27,62	9,14	96	66	-71	4,1
08.08.2017	01:45	36,97	27,64	6,86	95	71	-83	4,3
08.08.2017	07:41	36,95	27,62	11,03	95	61	-72	5,1
09.08.2017	22:55	36,97	27,66	13,74	90	67	-66	3,8
13.08.2017	11:15	37,08	27,68	28	346	20	-21	5
14.08.2017	02:42	37,12	27,7	7	111	71	-72	4,6
18.08.2017	14:09	36,9	27,62	16,79	106	65	-79	4,4